

Haemodynamic Simulation and Optimisation for the Flow-Diversion Treatment of Intracranial Aneurysms

Mingzi Zhang

A thesis submitted to Macquarie University
for the degree of Doctor of Philosophy

8 September 2018



MACQUARIE
University
SYDNEY • AUSTRALIA

Haemodynamic Simulation and Optimisation for the Flow-Diversion Treatment of Intracranial Aneurysms

Mingzi Zhang

Department of Biomedical Sciences
Faculty of Medicine and Health Sciences

Supervisor:

Itsu Sen (Yi Qian), PhD

Co-supervisors:

Makoto Ohta, PhD

David Ignatius Verrelli, PhD

M. Zhang

Sydney, Australia

STATEMENT OF ORIGINALITY

This work has not previously been submitted for a degree or diploma in any university, except for Tohoku University per the thesis submission agreement signed by both Macquarie University and Tohoku University before commencement of this joint-supervision Cotutelle program. To the best of my knowledge and belief, the thesis contains no material previously published or written by another person except where due reference is made in the thesis itself.

Mingzi Zhang

September 8, 2018

Table of Content

Table of Content.....	i
Acknowledgement	v
Summary	vii
List of Publications and Awards	ix
List of Figures	xi
List of Table	xvi
List of Abbreviations	xvii
Chapter 1 Introduction	1
1.1 Intracranial Aneurysms	2
1.2 Flow-Diversion Treatment	3
1.3 Fluid Flow Simulation	6
1.4 Literature Review	7
1.4.1 Haemodynamic simulation of flow in the Circle of Willis	7
1.4.2 CFD simulation of aneurysmal haemodynamics	7
1.4.3 Haemodynamic parameters proposed for examining the IA flow	8
1.4.4 Modelling of endovascular treatment for IAs	8
1.4.5 Optimisation studies in relation to FD treatment	9
1.5 Research Objectives	10
1.5.1 Existing problems	10
1.5.2 Objectives	11
1.6 Thesis Contents	12
Chapter 2 Materials and Methods	15
2.1 Aneurysm Model Geometries	16
2.1.1 Idealised aneurysm geometries	16
2.1.2 From medical images to the 3D aneurysm models	16
2.1.3 Realistic aneurysm geometries	17
2.2 Flow-diverting Stents	19
2.2.1 Pipeline Embolization Device	19
2.2.2 Silk stent	20
2.2.3 Flow-Redirection Endoluminal Device	21
2.2.4 Other endovascular devices	22

2.3 Virtual Stent Deployment.....	22
2.3.1 Spring–mass analogue.....	22
2.3.2 Modelling the restoring forces acting inside a FD stent	22
2.3.3 Simulation of virtual stent deployment	23
2.4 Haemodynamic Simulation	24
2.4.1 Computational grid generation	24
2.4.2 Computational fluid dynamics methods	25
Chapter 3 Structural Optimisation of Flow-Diverting Stent.....	27
3.1 Objective	28
3.2 Methods	28
3.2.1 Aneurysm geometries	29
3.2.2 FD stent model	30
3.2.3 Random modification of FD stent structure.....	31
3.2.4 Simulated annealing.....	31
3.2.5 Haemodynamic simulation.....	33
3.2.6 Longitudinal displacement test	34
3.2.7 Optimisation with different objective functions	34
3.3 Results	35
3.3.1 Optimisation with the AAV objective function.....	35
3.3.2 Optimisation with the AMV objective function	39
3.4 Discussion	43
3.4.1 Modification parameter used in optimisation	43
3.4.2 Objective function and SA procedure	44
3.4.4 Haemodynamic compatibility between FD structure and vascular geometry.....	45
3.4.5 Reliability of the optimised FD structure	46
3.4.6 Disruption of BOIs determines flow-diversion efficacy.....	46
3.5 Limitation and Future Work	47
3.6 Conclusion	47
Chapter 4 Haemodynamic Simulation of Flow-Diversion Treatments with Stent Compaction Applied	49
4.1 Objective	50
4.2 Methods	51
4.2.1 Aneurysm and FD stent model.....	51
4.2.2 FD stent modelling and deployment	51
4.2.3 Stent compaction ratio.....	51
4.2.4 Haemodynamic simulation.....	53

4.3 Results	54
4.3.1 FD wire structures and MCR after compaction.....	54
4.3.2 Observation of aneurysm flow patterns	62
4.3.3 Reduction of AAV, MF, and EL.....	63
4.4 Discussion.....	63
4.4.1 Morphological distinctions between the successful and the unsuccessful case	64
4.4.2 Haemodynamic effects of stent compaction	66
4.4.3 Haemodynamic effects of device diameter	67
4.4.4 Validation of the FD wire structures post-treatment	68
4.5 Limitation and Future Work.....	70
4.6 Conclusion	70
Chapter 5 Haemodynamic Simulation of Flow-Diversion Treatment with Multiple Flow-Diverting Stents.....	73
5.1 Objective	74
5.2 Methods	75
5.2.1 Aneurysm and FD models	75
5.2.2 Multiple FD Implantation	75
5.2.3 Haemodynamic Simulation	77
5.3 Results	78
5.3.1 Stent wire configurations, porosity, and pore-density	83
5.3.2 Aneurysmal flow patterns.....	86
5.3.3 Aneurysmal haemodynamics	87
5.4 Discussion.....	87
5.4.1 Mesh density and flow diversion enhanced by the second device	87
5.4.2 Effects of different stent diameters in dual-FD treatment	88
5.4.3 Different haemodynamic outcomes in two patient aneurysms	90
5.5 Limitation and Future Work.....	91
5.6 Conclusion	92
Chapter 6 Investigation of Incomplete Stent Expansion Effects on Aneurysmal Haemodynamics	95
6.1 Objective	96
6.2 Materials and Methods.....	97
6.2.1 Patient Aneurysms	97
6.2.2 Classification of IncSE.....	97
6.2.3 Virtual Stent Deployment	99
6.2.4 Aneurysmal Haemodynamics.....	100

6.3 Results	101
6.3.1 <i>In Vivo</i> and Virtually Deployed FD Stent Configurations.....	101
6.3.2 Aneurysmal Haemodynamics.....	102
6.3.3 Pressure Drop and Flow Patterns inside the Parent Artery	102
6.4 Discussion.....	106
6.4.1 IncSE and Its Association with the Parent Artery's Morphology.....	106
6.4.2 Counter-Intuitive Aneurysmal Flow Reduction Associated with the Proximal IncSE	107
6.4.3 IncSE-Induced Elevated Pressure Drop Increases the Aneurysmal Inflow	108
6.5 Limitations	109
6.6 Conclusion	109
Chapter 7 Applying Computational Simulation to the Design of Flow-Diversion Treatment: A Showcase.....	111
7.1 Objective	112
7.2 Materials and Methods	112
7.2.1 Treatment scenarios selected for comparison.....	112
7.2.2 Haemodynamic simulation.....	113
7.3 Results	113
7.3.1 Differences in flow-diversion efficacy	113
7.3.2 Observation of intra-aneurysmal haemodynamics	114
7.4 Discussion.....	116
7.4.1 Comparison of haemodynamics in different treatment scenarios	116
7.4.2 Effects of stent diameter vary with respect to the treatment strategy	116
7.4.3 Clinical relevance of designing a favourable treatment plan.....	117
7.5 Limitations.....	118
7.6 Conclusion	118
Chapter 8 Conclusion and Outlook	119
8.1 Conclusion	120
8.2 Outlook.....	122
Bibliography.....	125

Acknowledgement

This work was carried out under the supervision of Prof. Itsu Sen (Yi Qian), who has been continuously supporting me throughout my Cotutelle Ph.D. candidature. I would like to express my sincere gratitude to him for accepting me as his student and providing me with excellent supervision and guidance. I enjoy the fruitful and productive discussions with him, and this work would not have been possible without his valuable scientific inputs. Meanwhile, I would like to thank Mrs. Yuka Sen, the wife of Prof. Sen, for inviting and treating us many times in their home. The delicious food always reminded me the taste of home.

This work would not have been possible without the supervision of Prof. Makoto Ohta as my Cotutelle supervisor at Tohoku University, Japan. Prof. Ohta has been continuously supporting me in every aspect, since I first enrolled as an exchange student at his laboratory in 2011. I am especially grateful for his encouragement on my attending scientific conferences and participating in academic internship. Those activities helped me tremendously in enriching my academic experience and broadening my research horizon.

I am truly grateful to my co-supervisor Dr. David I. Verrelli, who has backed me up all the time in the way of research data analysis and journal article preparation. I always appreciate his suggestions and can never identify a comment from him that is unprofessional. Constructive discussions with him contributed enormously to a rigorous presentation of my research. His guidance and advice have educated me intensively, especially in the aspects of scientific data processing and academic English writing.

Besides my supervisors, I would also like to thank the members in my thesis's examination committee at Tohoku University, Prof. Toshiyuki Hayase and Prof. Yoichi Haga, for their time and constructive advice, which have tremendously improved the quality of the present dissertation. I am also thankful to Prof. Bastien Chopard at the

University of Geneva, for sharing fruitful research proposals with me and hosting me as an internship student in 2014.

I would like to acknowledge the fellowship of the other members of the Sen and the Ohta Laboratories, past and present. While it is impossible to list them all here individually, special thanks go to Mrs Yasuno Emori, who helped me a lot in dealing with administrative affairs. I extend my thanks to Doctors Toshio Nakayama, Hitomi Anzai, Yasutomo Shimizu, Simon Tupin, Kaihong Yu, and Xiaobo Han, for their kind assistance and support to my research; Narendra Putra, Tomohito Watanabe, Kazuhiro Watanabe, Taihei Onishi, and Ren Takahashi, for being my nice colleagues; Doctors Fengping Zhu, Liuen Olivia Liang, Xi Zhao, and, Yuanyuan Daisy Dai, for the good time we had in Sydney. And I would not forget the fun I had in Sendai, together with my friends: Yuuki Yoshida, Wataru Sakuma, Daichi Suzuki, Yuta Muramoto, Makoto Ito, and a lot of other friends in the IMR basketball club. All you people have made my Ph.D. journey a beautiful memory in my life.

Research does not always run smoothly, and I want to make special acknowledgement of Yujie Li for her companionship during our journey. Her patience, understanding, support, and the cuisines of home always brightened me up when I was in bad mood.

Finally, I must express my deepest gratitude to my mum and dad, who instilled in me an appreciation for knowledge and learning. It is their endless love, unconditional support, and firm belief in my capabilities that have made me strong and confident, enabling me to overcome the hurdles that I encountered in the way of striving for the best. My every little success would never have been possible without their support and encouragement. The family we formed is always my anchor, and I cherish the beautiful times we had together. I pray for us health, happiness, and the best of luck.

Mingzi

September 8, 2018

Summary

Despite various complications reported, flow-diverting (FD) stent implantation has become a major mode of treatment for intracranial aneurysms. Review of literature suggests that the treatment outcomes are closely associated with the aneurysmal haemodynamics changed by the implanted stent. In this thesis, I sought to examine the haemodynamic changes following different strategies of FD treatment and provide practical solutions to improve the stent's flow-diversion efficacy.

As the first accomplishment, I developed in Chapter 3 an automated optimisation method to be used to accommodate stent configuration to a specific aneurysm geometry. Adopting this method, wire structure of a stent can be modified to alter the local haemodynamics towards maximal reduction of the aneurysmal inflow. Furthermore, employing a virtual stent deployment technique and computational fluid dynamics analysis, I systematically investigated in Chapter 4 and 5 the aneurysmal haemodynamics following the flow-diversion treatment with a stent compaction technique applied or with dual-FD stents deployed — two of the most commonly adopted treatment strategies in the current interventional practice. These studies provided quantitative results illustrating stent wire characteristics and the subsequent aneurysmal haemodynamic changes in various flow-diversion scenarios. Finally, I examined in Chapter 6 the aneurysmal haemodynamics affected by incomplete stent expansion (IncSE) — a condition suspected to cause delayed aneurysm occlusion, for which various severities of IncSE occurring at different segments of the parent artery were modelled and examined. Results suggest that the effects of IncSE vary greatly with respect to the location where it occurs.

Based upon this series of studies, a workflow was put forward to individualise the treatment plan corresponding to the haemodynamic characteristics of a specific patient, from the patient aneurysm model reconstruction, to computer-aided stent deployment rehearsal, and then to the haemodynamic outcome analysis to determine the most effective treatment plan prior to the real treatment. An example of implementing this

workflow to predict the post-treatment haemodynamics thereby determining the most favourable treatment strategy was illustrated in detail in Chapter 7.

Apart from this useful application, methodologies developed in the thesis, including the FD stent modelling technique, the stent structural optimisation method, the classification of stent compaction, and the in-house software for stent deployment simulation, would certainly contribute to future research and development of FD stents and interventional planning.

List of Publications and Awards

Publications in Peer-Reviewed Academic Journals:

1. **Zhang M.**, Anzai H., Chopard B., Ohta M., **2016**. Towards the patient-specific design of flow diverters made from helix-like wires: an optimization study. *BioMedical Engineering Online*. 15, 371-382.
2. **Zhang M.**, Li Y., Zhao X., Verrelli D. I., Chong W., Ohta M., Qian Y., **2017**. Haemodynamic effects of stent diameter and compaction ratio on flow-diversion treatment of intracranial aneurysms: A numerical study of a successful and an unsuccessful case. *Journal of Biomechanics*. 58(2017), 179-186.
3. **Zhang M.**, Li Y., Verrelli D. I., Chong W., Ohta M., Qian Y., **2018**. Haemodynamic outcomes of intracranial aneurysm treatments with dual flow-diverting stents of different sizes. *Journal of Biomechanics*. (Under Review)
4. **Zhang M.**, Li Y., Sugiyama S., Verrelli D. I., Matsumoto Y., Tominaga T., Qian Y., Ohta M., **2018**. Incomplete stent expansion (IncSE) in flow-diversion treatment affects aneurysmal haemodynamics: A quantitative comparison of treatments affected by different severities of malapposition occurring in different segments of the parent artery. *Journal of Biomechanics*. (Under Review)
5. Li Y., **Zhang M.**, Verrelli D.I, Chong W., Ohta M., Qian Y., **2018**. Numerical simulation of aneurysmal haemodynamics with calibrated porous-medium models of flow-diverting stents. *Journal of Biomechanics*. (Accepted)
(<https://doi.org/10.1016/j.jbiomech.2018.08.026>)
6. Dai Y., Qian Y., **Zhang M.**, Li Y., Lv P., Tang X., Javadzadegan A., Lin J., **2018**. Associations between local haemodynamics and carotid intraplaque haemorrhage with different stenosis severities: a preliminary study based on MRI and CFD. *Journal of Clinical Neuroscience*. (Under Review)

Publications in Peer-Reviewed Conference Proceedings:

1. **Zhang M.**, Anzai H., Chopard B., Ohta M., **2015**. Manufacture-oriented design optimisation of a flow diverter stent using lattice Boltzmann method and simulated annealing, in: *Advances in Structural and Multidisciplinary Optimization. Proceedings of the 11th World Congress of Structural and Multidisciplinary Optimization (WCSMO-11)*. ISBN 13: 978-0-646-94394-7.
2. **Zhang M.**, Li Y., Verrelli D. I., Chong W., Ohta M., Qian Y., **2017**. Applying computer simulation to the design of flow-diversion treatment for intracranial aneurysms, in: *Engineering in Medicine and Biology Society (EMBC)*, pp. 3385-3388,

2017 *IEEE the 39th Annual International Conference of the IEEE*.
doi:10.1109/EMBC.2017.8037582

3. **Zhang M.**, Li Y., Verrelli D. I., Chong W., Ohta M., Qian Y., **2017**. Applying virtual stent deployment to study flow-diversion treatment for intracranial aneurysm: the effect of stent compaction on post-treatment wire configuration, in: *Proceedings of the 8th International Conference on Computational Methods (ICCM2017)*
4. Li Y., **Zhang M.**, Verrelli D. I., Yang W., Chong W., Ohta M., Qian Y., **2017**. A sensitivity study on modelling a flow-diverting stent as a porous medium using computational fluid dynamics, in: *Engineering in Medicine and Biology Society (EMBC)*, pp. 3389-3392, 2017 *IEEE the 39th Annual International Conference of the IEEE*. doi:10.1109/EMBC.2017.8037583
5. Li Y., **Zhang M.**, Verrelli D. I., Yang W., Chong W., Ohta M., Qian Y., **2017**. Modelling flow-diverting stent as porous medium with different permeabilities in the treatment of intracranial aneurysms: a comparison of a successfully treated case and an unsuccessful one, in *Proceedings of the 8th International Conference on Computational Methods (ICCM2017)*

Publications in Non-Peer-Reviewed Academic Journals:

1. 太田信, 安西眸, 吉田裕貴, **Zhang Mingzi**, Li Yujie, 中山敏男. ステンツの最適デザインを考へる. 脳神経外科速報, 2014, vol. 24(5), pp. 532-537.
2. 安西眸, 渡邊和浩, 張明子, Narendra Kurnia PUTRA, 竹島由里子, 太田信. 医工学分野における CAVE 活用. 可視化情報, 2016, vol. 36(143), pp. 20-24.

Co-authored Book Chapters:

1. 太田信, 安西眸, 吉田裕貴, **Zhang Mingzi**, Li Yujie, 中山敏男. 基礎からよくわかる, 実践的 CFD (数値流体力学) 入門, 脳血管編, **2017**. Chapter 4(2), pp. 165-171.

Award Received when Attending Academic Conferences:

The *Best Student Presentation Award*, in the Interdisciplinary Cerebrovascular Symposium (Intracranial Stent Meeting 2015), 13-14th November 2015, Gold Coast, Australia.

List of Figures

FIGURE 1-1 INTRACRANIAL ANEURYSMS OBSERVED IN ROTATIONAL ANGIOGRAPHY (LEFT) AND <i>IN VIVO</i> (RIGHT). AN1 TO AN4 IN THE INTRAOPERATIVE PHOTOGRAPHS RESPECTIVELY CORRESPOND TO FOUR ANEURYSMS IDENTIFIED IN THE ROTATIONAL ANGIOGRAPHICAL IMAGES[9].	2
FIGURE 1-2: ENDOVASCULAR TREATMENT OF IAS WITH AN FD STENT: THE DEPLOYMENT PROCEDURE FOR A PED FD STENT. [25]	4
FIGURE 1-3: THE HEALING PROCEDURE FOR IA TREATMENTS WITH A FD STENT. A: THE NO-STENT CONDITION, B: IMMEDIATELY AFTER FD STENT DEPLOYMENT, C: PARTIAL OCCLUSION OF THE ANEURYSM, AND D: COMPLETE OCCLUSION OF THE ANEURYSM. [26]	4
FIGURE 1-4: THREE REPRESENTATIVE BRANDS OF FD STENT: THE <i>PED</i> (TOP) [25], THE <i>Silk+</i> (MIDDLE) [27], AND THE <i>FRED</i> (BOTTOM) [28].	5
FIGURE 2-1: IDEALISED AND REALISTIC ANEURYSM MODELS USED IN CHAPTER 3. A: THE STRAIGHT IDEALISED MODEL (S MODEL), B: THE CURVED IDEALISED MODEL (C MODEL), AND C: THE REALISTIC MODEL (R MODEL).	16
FIGURE 2-2: THE GEOMETRY OF THE SUCCESSFULLY TREATED PATIENT ANEURYSM. (FIGURES ON THE LEFT AND ON THE RIGHT ARE THE MODEL VISUALISED FROM DIFFERENT CAMERA ANGLES.)	17
FIGURE 2-3: THE GEOMETRY OF THE UNSUCCESSFULLY TREATED PATIENT ANEURYSM. (FIGURES ON THE LEFT AND ON THE RIGHT ARE THE MODEL VISUALISED FROM DIFFERENT CAMERA ANGLES.)	18
FIGURE 2-4: THE MAXIMUM INSCRIBED SPHERE RADIUS WITH RESPECT TO THE POINTS ALONG THE CENTRELINES OF THE SUCCESSFUL CASE (LEFT) AND THE UNSUCCESSFUL CASE (RIGHT).	18
FIGURE 2-5: SCHEMATIC OF THE COMMERCIALLY AVAILABLE PACKAGING OF THE <i>PIPELINE</i> STENT. [25]	19
FIGURE 2-6: (TOP) THE COMMERCIALLY AVAILABLE <i>Silk+</i> STENT. (BOTTOM) SCHEMATIC OF THE TAPERED <i>Silk+</i> STENT WITH DIFFERENT DIAMETERS DESIGNED FOR THE DISTAL LANDING ZONE (LD) AND THE PROXIMAL LANDING ZONE (LP). [27]	20
FIGURE 2-7: (TOP) THE COMMERCIALLY AVAILABLE PACKAGING OF THE <i>FRED</i> SYSTEM. (BOTTOM) CONFIGURATION OF THE OUTER AND THE INNER STENT LAYERS. [28]	21
FIGURE 3-1: SCHEMATIC OF THE PROPOSED OPTIMISATION PROCEDURE	29
FIGURE 3-2: FROM CLOCKWISE AND ANTI-CLOCKWISE HELIX FILAMENTS TO AN FD STENT.	30
FIGURE 3-3: DEMONSTRATION OF STARTING PHASE CHANGES RESULTING IN LONGITUDINAL DISPLACEMENTS OF A HELIX. ...	32
FIGURE 3-4: THE SA PROCEDURES FOR THE S, C, AND R MODELS. (VERTICAL AXIS: R_f , HORIZONTAL AXIS: STEPS OF SA PROCEDURE.) OBJECTIVE FUNCTION: AAV.	35
FIGURE 3-5: VISUALISATION OF INTRA-ANEURYSMAL STREAMLINES, COLOUR-CODED BY VELOCITY MAGNITUDE, UNDER NO-STENT CONDITIONS, AND WITH STENT BEFORE AND AFTER OPTIMISATIONS, FOR RESPECTIVELY THE S, C, AND R ANEURYSM MODELS. (BLACK ARROWS: FLOW DIRECTION, RED ARROWS: BOI, BLUE ARROWS: BOO, AND YELLOW CIRCLES: INFLOW AREA.)	36
FIGURE 3-6: VISUALISATION OF INTRA-ANEURYSMAL ISO-VELOCITY SURFACES, CORRESPONDING TO 0.01, 0.015, AND 0.1 M/S, UNDER NO-STENT CONDITIONS, AND WITH STENT BEFORE AND AFTER OPTIMISATIONS, FOR RESPECTIVELY THE S, C, AND R MODELS. (BLACK ARROWS: FLOW DIRECTION; YELLOW CIRCLES: INFLOW AREA.)	36
FIGURE 3-7: VISUALISATION OF VELOCITY COMPONENTS PERPENDICULAR TO THE ANEURYSM NECK PLANE, UNDER NO-STENT CONDITIONS, AND WITH STENT BEFORE AND AFTER OPTIMISATIONS, FOR RESPECTIVELY THE S, C, AND R MODELS. (BLACK ARROWS: FLOW DIRECTION, RED CIRCLES: INFLOW AREA, AND BLUE CIRCLES: OUTFLOW AREA.)	38
FIGURE 3-8: VISUALISATION OF VELOCITY VECTORS GENERATED FROM THE ANEURYSM NECK PLANE, UNDER NO-STENT CONDITIONS, AND WITH STENT BEFORE AND AFTER OPTIMISATIONS, FOR RESPECTIVELY THE S, C, AND R MODELS. (BLACK ARROWS: FLOW DIRECTION; YELLOW CIRCLES: INFLOW AREA.)	38
FIGURE 3-9: LDTs OF THE OPTIMISED FD STENT STRUCTURES FOR RESPECTIVELY THE S, C, AND R MODELS (HORIZONTAL AXIS: THE LONGITUDINAL DISPLACEMENT OF THE RESPECTIVE FD STENT STRUCTURE).	40
FIGURE 3-10: THE SA DEVELOPMENTS FOR THE S AND C MODELS. (VERTICAL AXIS: R_f , HORIZONTAL AXIS: STEPS OF SA PROCEDURE.) OBJECTIVE FUNCTION: AMV.	41
FIGURE 3-11: VISUALISATION OF INTRA-ANEURYSMAL STREAMLINES, COLOUR-CODED BY VELOCITY MAGNITUDE, BEFORE AND AFTER OPTIMISATIONS, FOR RESPECTIVELY THE S AND C ANEURYSM MODELS. (RED ARROWS: BOI, RECTANGLE WITH	

RED DOTTED LINES: RESULTS OBTAINED FROM ADOPTING AAV AS OBJECTIVE FUNCTION, AND RECTANGLE WITH GREEN DOTTED LINES: RESULTS OBTAINED FROM ADOPTING AMV AS OBJECTIVE FUNCTION.).....	41
FIGURE 3-12: VISUALISATION OF VELOCITY COMPONENTS PERPENDICULAR TO THE ANEURYSM NECK PLANE BEFORE AND AFTER OPTIMISATIONS, FOR RESPECTIVELY THE S AND C ANEURYSM MODELS. (YELLOW CIRCLES: INFLOW AREA, RECTANGLE WITH RED DOTTED LINES: RESULTS OBTAINED FROM ADOPTING AAV AS OBJECTIVE FUNCTION, AND RECTANGLE WITH GREEN DOTTED LINES: RESULTS OBTAINED FROM ADOPTING AMV AS OBJECTIVE FUNCTION.)	42
FIGURE 3-13: VISUALISATION OF VELOCITY VECTORS GENERATED FROM THE ANEURYSM NECK PLANE BEFORE AND AFTER OPTIMISATIONS, FOR RESPECTIVELY THE S AND C ANEURYSM MODELS. (RED CIRCLES: INFLOW AREA, RECTANGLE WITH RED DOT LINES: RESULTS OBTAINED FROM ADOPTING AAV AS OBJECTIVE FUNCTION, AND RECTANGLE WITH GREEN DOTTED LINES: RESULTS OBTAINED FROM ADOPTING AMV AS OBJECTIVE FUNCTION.).....	42
FIGURE 3-14: VISUALISATION OF REDUCTION RATES OF AMV AND AAV OF THE S AND C MODELS. OBJECTIVE FUNCTION FOR OPTIMISATION: AMV.....	43
FIGURE 4-1: FD STENT DEPLOYMENT PROCESS OF THE SUCCESSFUL ANEURYSM CASE. (FROM TOP-LEFT TO BOTTOM-RIGHT: STENT VERTICES FULLY CRIMPED TO FULLY EXPANDED).....	54
FIGURE 4-2: FD STENT DEPLOYMENT PROCESS OF THE UNSUCCESSFUL ANEURYSM CASE. (FROM TOP-LEFT TO BOTTOM-RIGHT: STENT VERTICES FULLY CRIMPED TO FULLY EXPANDED).....	55
FIGURE 4-3: FD STENT CONFIGURATIONS OF TREATMENTS WITH FD STENTS OF THREE DIFFERENT DIAMETERS, D , AT FOUR COMPACTION LEVELS IN THE UNSUCCESSFUL CASE. THE UNTREATED CASE IS ALSO SHOWN FOR COMPARISON. (NT: UNTREATED CONDITION; CPT: COMPACTION LEVEL.).....	56
FIGURE 4-4: FD STENT CONFIGURATIONS OF TREATMENTS WITH FD STENTS OF THREE DIFFERENT DIAMETERS, D , AT FOUR COMPACTION LEVELS IN THE UNSUCCESSFUL CASE. THE UNTREATED CASE IS ALSO SHOWN FOR COMPARISON. (NT: UNTREATED CONDITION; CPT: COMPACTION LEVEL.).....	56
FIGURE 4-5: METAL COVERAGE RATES MEASURED ACROSS THE ANEURYSM OSTIUM FOR THE SUCCESSFUL (LEFT) AND THE UNSUCCESSFUL (RIGHT) CASES.....	57
FIGURE 4-6: ISO-VELOCITY VISUALISATION OF TREATMENTS WITH FD STENTS OF THREE DIFFERENT DIAMETERS, D , AT FOUR COMPACTION LEVELS IN THE SUCCESSFUL CASE. INFLOW BOUNDARY CONDITION = 130 mL/MIN. THE UNTREATED CASE IS ALSO SHOWN FOR COMPARISON. (NT: UNTREATED CONDITION; CPT: COMPACTION LEVEL.).....	57
FIGURE 4-7: ISO-VELOCITY VISUALISATION OF TREATMENTS WITH FD STENTS OF THREE DIFFERENT DIAMETERS, D , AT FOUR COMPACTION LEVELS IN THE UNSUCCESSFUL CASE. INFLOW BOUNDARY CONDITION = 130 mL/MIN. THE UNTREATED CASE IS ALSO SHOWN FOR COMPARISON. (NT: UNTREATED CONDITION; CPT: COMPACTION LEVEL.).....	58
FIGURE 4-8: STREAMLINE VISUALISATION FOR TREATMENTS WITH FD STENTS OF THREE DIFFERENT DIAMETERS, D , AT FOUR COMPACTION LEVELS IN THE SUCCESSFUL CASE. INFLOW BOUNDARY CONDITION = 130 mL/MIN. THE UNTREATED CASE IS ALSO SHOWN FOR COMPARISON. (NT: UNTREATED CONDITION; CPT: COMPACTION LEVEL.).....	58
FIGURE 4-9: STREAMLINE VISUALISATION FOR TREATMENTS WITH FD STENTS OF THREE DIFFERENT DIAMETERS, D , AT FOUR COMPACTION LEVELS IN THE UNSUCCESSFUL CASE. INFLOW BOUNDARY CONDITION = 130 mL/MIN. THE UNTREATED CASE IS ALSO SHOWN FOR COMPARISON. (NT: UNTREATED CONDITION; CPT: COMPACTION LEVEL.).....	59
FIGURE 4-10: WSS VISUALISATION OF TREATMENTS WITH FD STENTS OF THREE DIFFERENT DIAMETERS, D , AT FOUR COMPACTION LEVELS IN THE SUCCESSFUL CASE. INFLOW BOUNDARY CONDITION = 130 mL/MIN. THE UNTREATED CASE IS ALSO SHOWN FOR COMPARISON. (NT: UNTREATED CONDITION; CPT: COMPACTION LEVEL.).....	59
FIGURE 4-11: WSS VISUALISATION OF TREATMENTS WITH FD STENTS OF THREE DIFFERENT DIAMETERS, D , AT FOUR COMPACTION LEVELS IN THE UNSUCCESSFUL CASE. INFLOW BOUNDARY CONDITION = 130 mL/MIN. THE UNTREATED CASE IS ALSO SHOWN FOR COMPARISON. (NT: UNTREATED CONDITION; CPT: COMPACTION LEVEL.).....	60
FIGURE 4-12: RELATIVE VALUES OF AAV AFTER TREATMENTS WITH A FD STENT FOR THREE DIFFERENT DIAMETERS AND FOUR COMPACTION LEVELS. SYMBOLS ARE PLOTTED AT THE AVERAGE FOR THE FIVE INFLOW BOUNDARY CONDITIONS; VERTICAL ERROR BARS INDICATE THE STANDARD DEVIATION FOR EACH SUCH CONDITION. THE UNTREATED CONDITION (NT) REPRESENTS THE 100% LEVEL IN EACH GRAPH.	61
FIGURE 4-13: RELATIVE VALUES OF MF AFTER TREATMENTS WITH A FD STENT FOR THREE DIFFERENT DIAMETERS AND FOUR COMPACTION LEVELS. SYMBOLS ARE PLOTTED AT THE AVERAGE FOR THE FIVE INFLOW BOUNDARY CONDITIONS; VERTICAL ERROR BARS INDICATE THE STANDARD DEVIATION FOR EACH SUCH CONDITION. THE UNTREATED CONDITION (NT) REPRESENTS THE 100% LEVEL IN EACH GRAPH.	61
FIGURE 4-14: RELATIVE VALUES OF EL AFTER TREATMENTS WITH A FD STENT FOR THREE DIFFERENT DIAMETERS AND FOUR COMPACTION LEVELS. SYMBOLS ARE PLOTTED AT THE AVERAGE FOR THE FIVE INFLOW BOUNDARY CONDITIONS; VERTICAL	

ERROR BARS INDICATE THE STANDARD DEVIATION FOR EACH SUCH CONDITION. THE UNTREATED CONDITION (NT) REPRESENTS THE 100% LEVEL IN EACH GRAPH.	62
FIGURE 4-15: THE MAGNIFIED VIEW OF FD WIRE DILATION INTO THE ANEURYSM LUMEN. SUB-FIGURES (A) AND (B) SHOW THE FD WIRES AFTER DEPLOYMENT IN RESPECTIVELY THE SUCCESSFUL AND THE UNSUCCESSFUL CASE; SUB-FIGURES (C) AND (D) DEPICT THE CENTRELINES EXTRACTED FROM THE RESPECTIVE ANEURYSM GEOMETRY FOR COMPARISON.	65
FIGURE 4-16: COMPARISON OF CFD SIMULATIONS AND ANGIOGRAPHIC MEDICAL IMAGERY FOR THE UNSUCCESSFUL CASE. TOP: CFD RESULTS OF ISO-VELOCITY SURFACE (LEFT) AND STREAMLINES (RIGHT); BOTTOM: DSA IMAGES TAKEN UPON THE 6 TH MONTH'S FOLLOW-UP AFTER TREATMENT.	65
FIGURE 4-17: THE COMPARISON OF FD WIRE STRUCTURES BETWEEN <i>IN VITRO</i> AND VIRTUAL DEPLOYMENTS. (ROW I: RAW IMAGES, ROW II: SELECTING THE REGION OF INTEREST (ROI), AND ROW III: SUBDOMAINS POST IMAGE PROCESSING. LEFT AND RIGHT SERIES ARE FD WIRES OBSERVED FROM TWO CAMERA ANGLES)	68
FIGURE 4-18: COMPARISON OF FD WIRE CHARACTERISTICS BETWEEN <i>IN VITRO</i> AND VIRTUAL DEPLOYMENTS IN SCENES 1 AND 2. VERTICAL ERROR BARS INDICATE THE STANDARD DEVIATION (SD) OF THE DATA FOR EACH CONDITION.	70
FIGURE 5-1: SCHEMATIC OF VIRTUAL STENT DEPLOYMENT OF TWO FD DEVICES. (I_A: RECIPIENT ANEURYSM GEOMETRY, I_B: THE FIRST FD STENT TO BE DEPLOYED, II_A: DEPLOYMENT OF THE FIRST STENT, II_B: SURFACE FITTING OF THE FIRST DEPLOYED STENT, III_A: DEPLOYMENT OF THE SECOND STENT, III_B: THE SECOND FD STENT TO BE DEPLOYED, AND IV: ANEURYSM WITH TWO FD STENTS IMPLANTED.)	76
FIGURE 5-2: THE COMPUTATIONAL MESH OF THE ANEURYSM MODEL WITH TWO STENTS DEPLOYED IN THE PARENT ARTERY. (A) MODEL GEOMETRY; (B) MODEL SURFACE MESH; (C) VOLUME MESH IN THE CROSS SECTION DEPICTED IN 'A'; AND (D) MAGNIFIED VIEW OF THE STENT MESH DETAILS ENCLOSED IN A SQUARE IN 'C'.	78
FIGURE 5-3: FD STENT CONFIGURATIONS OF TREATMENTS WITH SINGLE OR DUAL FD STENTS FOR THE SUCCESSFUL CASE. THE UNTREATED CASE IS ALSO SHOWN FOR COMPARISON. (NT: THE UNTREATED CONDITION; SFD: SINGLE FD TREATMENT; AND DFD: DUAL FD STENT TREATMENT.)	79
FIGURE 5-4: FD STENT CONFIGURATIONS OF TREATMENTS WITH SINGLE OR DUAL FD STENTS FOR THE UNSUCCESSFUL CASE. THE UNTREATED CASE IS ALSO SHOWN FOR COMPARISON. (NT: THE UNTREATED CONDITION; SFD: SINGLE FD TREATMENT; AND DFD: DUAL FD STENT TREATMENT.)	80
FIGURE 5-5: ISO-VELOCITY SURFACES OF TREATMENTS WITH SINGLE OR DUAL FD STENTS FOR THE SUCCESSFUL CASE. THE UNTREATED CASE IS ALSO SHOWN FOR COMPARISON. (NT: THE UNTREATED CONDITION; SFD: SINGLE FD TREATMENT; AND DFD: DUAL FD STENT TREATMENT.)	80
FIGURE 5-6: ISO-VELOCITY SURFACES OF TREATMENTS WITH SINGLE OR DUAL FD STENTS FOR THE UNSUCCESSFUL CASE. THE UNTREATED CASE IS ALSO SHOWN FOR COMPARISON. (NT: THE UNTREATED CONDITION; SFD: SINGLE FD TREATMENT; AND DFD: DUAL FD STENT TREATMENT.)	81
FIGURE 5-7: STREAMLINES OF TREATMENTS WITH SINGLE OR DUAL FD STENTS FOR THE SUCCESSFUL CASE. THE UNTREATED CASE IS ALSO SHOWN FOR COMPARISON. (NT: THE UNTREATED CONDITION; SFD: SINGLE FD TREATMENT; AND DFD: DUAL FD STENT TREATMENT.)	81
FIGURE 5-8: STREAMLINES OF TREATMENTS WITH SINGLE OR DUAL FD STENTS FOR THE UNSUCCESSFUL CASE. THE UNTREATED CASE IS ALSO SHOWN FOR COMPARISON. (NT: THE UNTREATED CONDITION; SFD: SINGLE FD TREATMENT; AND DFD: DUAL FD STENT TREATMENT.)	82
FIGURE 5-9: WSS OF TREATMENTS WITH SINGLE OR DUAL FD STENTS FOR THE SUCCESSFUL CASE. THE UNTREATED CASE IS ALSO SHOWN FOR COMPARISON. (NT: THE UNTREATED CONDITION; SFD: SINGLE FD TREATMENT; AND DFD: DUAL FD STENT TREATMENT.)	82
FIGURE 5-10: WSS OF TREATMENTS WITH SINGLE OR DUAL FD STENTS FOR THE UNSUCCESSFUL CASE. THE UNTREATED CASE IS ALSO SHOWN FOR COMPARISON. (NT: THE UNTREATED CONDITION; SFD: SINGLE FD TREATMENT; AND DFD: DUAL FD STENT TREATMENT.)	83
FIGURE 5-11: POROSITIES WITHIN THE NECK PLANE AFTER TREATMENTS WITH SINGLE OR DUAL FD STENTS FOR RESPECTIVELY THE SUCCESSFUL AND THE UNSUCCESSFUL CASES. STENT SIZES ON THE HORIZONTAL AXIS INDICATE THE OUTER (EARLIER DEPLOYED) STENT DIAMETER; STENT SIZES REPRESENTED BY DIFFERENT COLOURS IN THE LEGEND INDICATE THE INNER (LATER DEPLOYED) STENT DIAMETER. (SFD: TREATMENTS WITH A SINGLE FD STENT AND DFD: TREATMENTS WITH TWO FD STENTS.)	84
FIGURE 5-12: NUMBER OF PORES WITHIN THE NECK PLANE AFTER TREATMENTS WITH SINGLE OR DUAL FD STENTS FOR RESPECTIVELY THE SUCCESSFUL AND THE UNSUCCESSFUL CASES. STENT SIZES ON THE HORIZONTAL AXIS INDICATE THE OUTER (EARLIER DEPLOYED) STENT DIAMETER; STENT SIZES REPRESENTED BY DIFFERENT COLOURS IN THE LEGEND	

INDICATE THE INNER (LATER DEPLOYED) STENT DIAMETER. (SFD: TREATMENTS WITH A SINGLE FD STENT AND DFD: TREATMENTS WITH TWO FD STENTS.).....	84
FIGURE 5-13: RELATIVE VALUES OF INTRA-ANEURYSMAL MF AFTER TREATMENTS WITH SINGLE OR DUAL FD STENTS FOR RESPECTIVELY THE SUCCESSFUL AND THE UNSUCCESSFUL CASES. STENT SIZES ON THE HORIZONTAL AXIS INDICATE THE OUTER (EARLIER DEPLOYED) STENT DIAMETER; STENT SIZES REPRESENTED BY DIFFERENT COLOURS IN THE LEGEND INDICATE THE INNER (LATER DEPLOYED) STENT DIAMETER. (SFD: TREATMENTS WITH A SINGLE FD STENT AND DFD: TREATMENTS WITH TWO FD STENTS.).....	84
FIGURE 5-14: RELATIVE VALUES OF INTRA-ANEURYSMAL EL AFTER TREATMENTS WITH SINGLE OR DUAL FD STENTS FOR RESPECTIVELY THE SUCCESSFUL AND THE UNSUCCESSFUL CASES. STENT SIZES ON THE HORIZONTAL AXIS INDICATE THE OUTER (EARLIER DEPLOYED) STENT DIAMETER; STENT SIZES REPRESENTED BY DIFFERENT COLOURS IN THE LEGEND INDICATE THE INNER (LATER DEPLOYED) STENT DIAMETER. (SFD: TREATMENTS WITH A SINGLE FD STENT AND DFD: TREATMENTS WITH TWO FD STENTS.).....	85
FIGURE 5-15: THE MEASUREMENT DOMAINS SELECTED FOR CALCULATING POROSITY AND NUMBER OF PORES IN BOTH ANEURYSM CASES. ARROWS INDICATE THE PERPENDICULAR DIRECTION TO THE NECK PLANES; RECTANGLES SHOW THE BOUNDARIES OF NECK MEASUREMENT PLANES; AND THE ORANGE AREAS INDICATE THE DOMAINS USED FOR CALCULATING THE POROSITY AND NUMBER OF PORES.....	86
FIGURE 5-16: THE STENT WIRE CONFIGURATIONS OBSERVED IN DUAL-FD STENT TREATMENTS WITH IDENTICAL-DIAMETER STENTS (INNER STENT 5 MM, OUTER STENT 5 MM) AND WITH DIFFERENT-DIAMETER STENTS (INNER STENT 5 MM, OUTER STENT 4.5 MM) FOR THE SUCCESSFUL CASE. TOP ROW: OVERVIEW OF THE TWO SCENARIOS. BOTTOM ROW: MAGNIFIED VIEW OF THE RECTANGULAR REGION (IDENTIFYING THE ANEURYSMAL INFLOW SEGMENT) OUTLINED IN RED IN THE OVERVIEW IMAGES.	89
FIGURE 5-17: COMPARISON OF CFD SIMULATIONS AND ANGIOGRAPHIC MEDICAL IMAGERY FOR THE UNSUCCESSFUL CASE. LEFT: CFD RESULTS OF ISO-VELOCITY SURFACES VISUALISED FROM TWO DIFFERENT ANGLES; RIGHT: THREE-DIMENSIONAL CTA (TOP) AND DSA IMAGE (BOTTOM) TAKEN AFTER THE SECOND FD STENT TREATMENT.	90
FIGURE 6-1: CENTRELINE TRAJECTORIES COLOUR-CODED BY CURVATURE (ROW 1) AND TORSION (ROW 2); SEGMENTS OF STENT WHERE INCSE MAY OCCUR (ROW 3); AND THE INCSE OBSERVED <i>IN VIVO</i> (ROW 4) FOR CASE 'A' AND 'B'. RED ARROWS INDICATE THE OBSERVED INCSE; BLACK ARROWS INDICATE REFERENCE LOCATION FOR QUANTIFYING DEGREE OF INCSE; AND YELLOW DASHED CIRCLES AND OVALS INDICATE THE LOCATION OF THE LABELLED REGIONS.	98
FIGURE 6-2: SCHEMATIC FOR THE DETERMINATION OF DIFFERENT LEVELS OF INCSE OCCURRING IN THE CENTRAL (TOP) AND THE DISTAL (BOTTOM) SEGMENT OF A FD STENT. A CENTRAL INCSE IS CLASSIFIED BY THE RADIUS MEASURED FROM THE STENT CROSS SECTION CORRESPONDING TO THE CENTRELINE POINT 'CM' — R_1 (50% OF R_3), R_2 (75% OF R_3), AND R_3 RESPECTIVELY INDICATE A STENT AT THE SEVERE LEVEL OF INCSE, AT THE INTERMEDIATE LEVEL, AND UNDER THE FULLY EXPANDED CONDITION. A DISTAL (OR A PROXIMAL) INCSE IS CLASSIFIED BY THE DIAMETER CORRESPONDING TO THE CENTRELINE POINT 'DM' (OR 'PM') — D_1 (50% OF D_3), D_2 (75% OF D_3), AND D_3 RESPECTIVELY INDICATE A STENT AT THE SEVERE LEVEL OF INCSE, AT THE INTERMEDIATE LEVEL, AND UNDER THE FULLY EXPANDED CONDITION.	99
FIGURE 6-3: FLOWRATES MEASURED BY pCMRI AT THE INLETS OF ICA FOR RESPECTIVELY CASE 'A' AND CASE 'B'.....	100
FIGURE 6-4: FD STENT CONFIGURATIONS AND HAEMODYNAMIC VISUALISATIONS OF TREATMENTS IN WHICH INCSE OCCURS AT DIFFERENT LEVELS OF SEVERITY: (A) FD STENT WIRE CONFIGURATIONS; (B) ISO-VELOCITY SURFACES; (C) STREAMLINES; AND (D) WALL SHEAR STRESS DISTRIBUTIONS. THE UNTREATED CONDITION AND THE TREATMENT WITH FD STENTS IDEALLY DEPLOYED ARE ALSO SHOWN FOR COMPARISON.	103
FIGURE 6-5: COMPARISON OF STENT WIRE CONFIGURATIONS BETWEEN VIRTUAL AND <i>IN VIVO</i> DEPLOYMENT (DSA IMAGERY) FROM TWO DIFFERENT CAMERA VIEWS FOR THE TWO CASES. INCSE SCENARIOS 'C-S' AND 'D-S' WERE RESPECTIVELY COMPARED TO <i>IN VIVO</i> DEPLOYMENTS FOR CASE 'A' AND 'B'. (RED ARROWS INDICATE THE SEGMENTS WHERE STENT WIRE MALAPPOSITION OCCUR.)	104
FIGURE 6-6: NORMALISED VALUES OF THE INTRA-ANEURYSMAL MASS FLOWRATE (MF), ENERGY LOSS (EL), AVERAGE VELOCITY (AV), AND AVERAGE VELOCITY CURL (VC) MEASURED FROM THE IDEAL DEPLOYMENT SCENARIOS (CONTROL GROUP, INDICATED WITH '*') AND INCSE SCENARIOS 'P-S', 'P-I', 'C-S', 'C-I', 'D-S', AND 'D-I' FOR BOTH ANEURYSMS. THE UNTREATED CONDITION (NT) REPRESENTS THE 100% LEVEL IN EACH BAR CHART.....	105
FIGURE 6-7: COMPARISONS OF THE PARENT-ARTERY FLOW PATTERN AND SHEAR STRESS DISTRIBUTION ON THE STENT SURFACE BETWEEN TREATMENTS IN WHICH INCSE OCCURS AT THREE DIFFERENT STENT SEGMENTS. (BLACK ARROWS INDICATE THE DIRECTION OF THE PARENT-ARTERY FLOW; DASHED BLACK CIRCLES INDICATE THE REGIONS WHERE COLLAPSED STENT WIRES PERSIST IN THE CENTRE OF THE PARENT ARTERY THAT DISRUPT THE PARENT-ARTERIAL FLOW.).....	107

FIGURE 7-1: FD STENT CONFIGURATIONS AND HAEMODYNAMIC VISUALISATION OF THE SIX TREATMENT SCENARIOS. THE UNTREATED CASE IS ALSO GIVEN FOR COMPARISON. (LEFT COLUMN: FD STENT CONFIGURATIONS; YELLOW IS 4 MM; BLUE IS 5 MM. MIDDLE COLUMN: FLOW STREAMLINES. RIGHT COLUMN: WSS DISTRIBUTION. ROWS 1 TO 7: TREATMENT SCENARIOS 'NT', 'D4NCPT', 'D5NCPT', 'D4CP80', 'D5CP80', 'D4INTO5', AND 'D5INTO4'.).....	115
FIGURE 7-3: RELATIVE MASS FLOW RATE AND ENERGY LOSS VALUES FOR THE SIX TREATMENT SCENARIOS. (THE UNTREATED CONDITION, NT, REPRESENTS THE 100% LEVEL.)	117

List of Table

TABLE 3-1: INITIAL TEMPERATURES AND LOWER TEMPERATURE LIMITS FOR RESPECTIVELY THE S, C, AND R MODELS.	32
TABLE 3-2: INTRA-ANEURYSMAL AVERAGE VELOCITIES AND R_f UNDER THE NO-STENT, INITIAL STENT, AND OPTIMAL STENT PLACEMENTS FOR RESPECTIVELY THE S, C, AND R MODELS (OBJECTIVE FUNCTION: AAV).	37
TABLE 3-3: INITIAL TEMPERATURES AND LOWER TEMPERATURE LIMITS OF SA PROCEDURES FOR THE S AND C MODELS.	39
TABLE 3-4: THE AMVS AND R_f UNDER THE NO-STENT, INITIAL STENT AND OPTIMISED FD CONDITIONS OF RESPECTIVELY THE S AND C MODELS. (OBJECTIVE FUNCTION: AMV).....	40
TABLE 4-1: THE AVERAGE IMPROVEMENTS OF FLOW REDUCTION WITH EACH LEVEL'S (25%) ADVANCEMENT OF COMPACTION RATIO, COMPARED TO THE NO-STENT CONDITIONS. VALUES ARE THE AVERAGE FOR THE FIVE INFLOW BOUNDARY CONDITIONS.	55
TABLE 4-2: THE DIFFERENCE BETWEEN THE MAXIMUM AND THE MINIMUM VALUE OF EACH HAEMODYNAMIC PARAMETER AT A GIVEN COMPACTION LEVEL, CONSIDERING FIVE INFLOW CONDITIONS AND THREE DIAMETERS. VALUES ARE THE PROPORTIONAL DIFFERENCES COMPARED TO THE NO-STENT CONDITIONS.....	60
TABLE 4-3: THE PORE-DENSITY, POROSITY, AND WIRE BRAIDING ANGLE MEASURED FROM THE FD STRUCTURES AFTER VIRTUAL AND <i>IN VITRO</i> DEPLOYMENTS.	69
TABLE 5-1: THE MF AND EL REDUCTION (COMPARED TO THE UNTREATED CONDITION) AFTER TREATMENTS WITH SINGLE OR DUAL FD STENTS. THE RESULTS FOR TWO FD STENTS ARE SUMMARISED WITH THE MEANS AND STANDARD DEVIATIONS (SD), IN WHICH THE EARLIER DEPLOYED STENT HAS THE SAME DIAMETER AS THE SINGLE STENT IN THE SAME ROW.	79
TABLE 6-1: PRESSURE DROP (PA) OF BLOOD FLOW FROM THE INLET TO THE OUTLET THROUGH THE PARENT ARTERY IN DIFFERENT INCSE SCENARIOS FOR THE TWO CASES.	104
TABLE 7-1: HAEMODYNAMIC PARAMETERS CALCULATED BEFORE AND AFTER THE SIX TREATMENT SCENARIOS.	114

List of Abbreviations

2D	Two-dimensional
3D	Three-dimensional
AAV	Intra-aneurysmal Average Velocity
ACA	Anterior Communicating Artery
AMV	Intra-aneurysmal Maximum Velocity
BOI	Bundle of Inflow
BOO	Bundle of Outflow
CFD	Computational Fluid Dynamics
CoW	Circle of Willis
CPT	Compaction Ratio
CTA	Computed Tomography Angiography
DFD	Dual Flow-Diverting Stent Treatment
DSA	Digital Subtraction Angiography
EL	Energy Loss
FD	Flow-diverting Stent
FDM	Finite Difference Method
FEM	Finite Element Method
FRED	Flow-Redirection Endoluminal Device
FSI	Fluid–Structure Interaction
FVM	Finite Volume Method
IA	Intracranial Aneurysm
ICA	Internal Carotid Artery
LBM	Lattice Boltzmann Method
LDT	Longitudinal Displacement Test
MCA	Middle Cerebral Artery
MCR	Metal Coverage Ratio
MF	Mass Flowrate
MISR	Maximum Inscribed Sphere Radius
MRI	Magnetic Resonance Imaging
NT	Not Treated
ODE	Ordinary Differential Equation
OSI	Oscillatory Shear Index

PCA	Posterior Communicating Artery
PDE	Partial Differential Equation
PED	Pipeline Embolization Device
PIV	Particle Image Velocimetry
ROI	Region of Interest
RT	Residence Time
SA	Simulated Annealing
SAH	Subarachnoid Haemorrhage
SD	Standard Deviation
SFD	Single Flow-diverting Stent Treatment
VMTK	Vascular Modelling Toolkit
VC	Velocity Curl
WSS	Wall Shear Stress

Chapter 1

Introduction

1.1 Intracranial Aneurysms

Intracranial aneurysms (IAs, see Figure 1-1, also known as brain or cerebral aneurysms, are common cerebrovascular disorders where a weakness in the wall of cerebral arteries dilates out and finally forms a bulging of the cerebral artery [1–3]. With a prevalence between 1 and 5% of the adult population [1,4,5], IAs can be asymptomatic, incidentally detected by computed tomography (CT) or magnetic resonance imaging (MRI) scans, or be found based on a collection of symptoms, such as severe headache, nausea, vomiting, vision impairment, *etc.* [4,6–8]

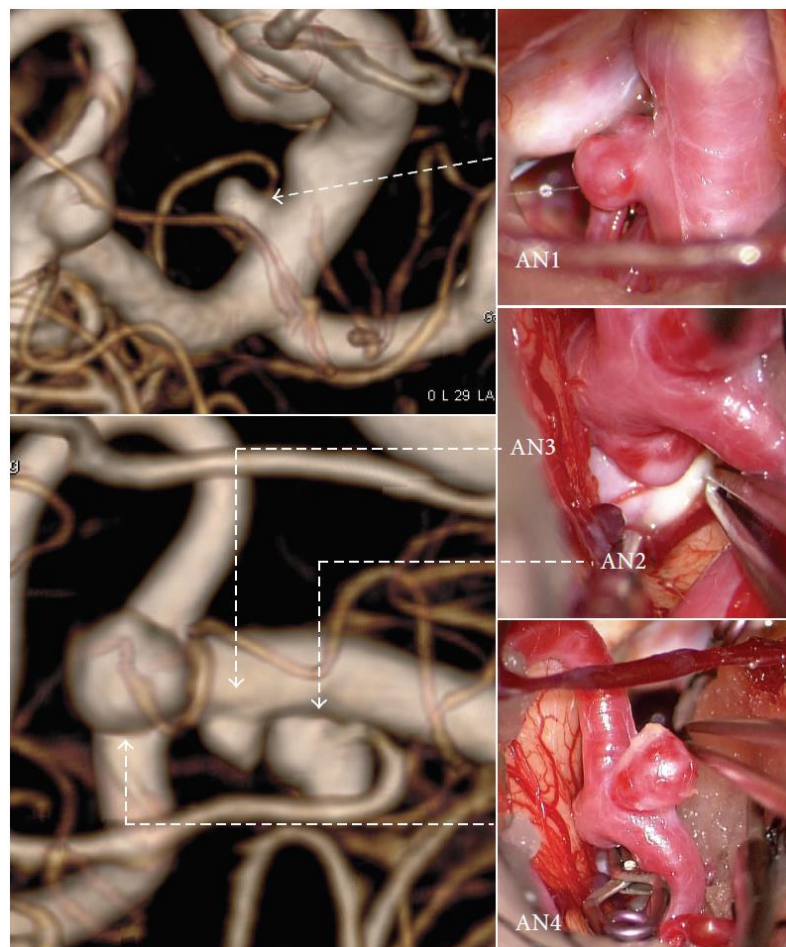


Figure 1-1 Intracranial aneurysms observed in rotational angiography (left) and *in vivo* (right). AN1 to AN4 in the intraoperative photographs respectively correspond to four aneurysms identified in the rotational angiographical images[9].

IAs are geometrically classified by size: small, large, and giant aneurysms respectively refer to those with diameters of less than 15, 15 to 25, and over 25 mm; and by shape — saccular, fusiform, and dissecting aneurysms [1]. IAs can occur in any segment of

the cerebral arteries, while the most frequent locations are reported to be the anterior communicating artery (30%), the posterior communicating artery (25%), and the middle cerebral artery (20%).

Untreated aneurysms may result in rupture, leading to subarachnoid haemorrhage (SAH) that severely threatens the patients' lives. As reported by published retrospective studies, IA-rupture-induced SAH accounts for approximately 5 to 15% of stroke, with a 30 days' mortality rate of 45% and a disability rate of 30% for the survivors [10,11]. Although the causes of IA initiation, progression, and rupture remain unclear, hypertension, vascular lesion induced by smoking, and adverse local haemodynamic changes are believed to be major factors [3].

1.2 Flow-Diversion Treatment

Some IAs can be treated with surgical clipping, in which neurosurgeons open the skull of a patient, *i.e.* a craniotomy, and isolate the aneurysm from the normal parent-artery circulation by placing a small clip across the aneurysm neck [7,8,12].

In the past decades, minimally invasive endovascular therapies, including stent-assisted coiling and flow-diverting (FD) stent implantation, have been proposed for the treatment of IAs. In the treatment with coils, neuroradiologists insert a flexible catheter (at the tip of which tiny coils are concealed) into the bloodstream through the femoral artery. When the catheter reaches the aneurysm segment of the parent artery, treating clinicians release those tiny coils into the aneurysm lumen to "fill up" the aneurysm. [13–17]

In contrast to treatments that physically clip the aneurysm or fill the aneurysm lumen with coils, flow-diversion treatments are intended to "divert", *i.e.* to re-direct much of the blood flow away, with an FD stent deployed across the aneurysm neck, such that most blood does not enter the aneurysm, thereby promoting blood clotting and thrombotic occlusion of the aneurysm (Figure 1-2). Prior to the invention and application of FD stents, many IAs went untreated, especially fusiform aneurysms, aneurysms with wide necks that cannot be coiled, or aneurysms that are hard to access

in a craniotomy [18–24]. Meanwhile, the FD stent serves as an alternative treatment for aneurysms that cannot be treated or failed to be treated by other approaches. Figure 1-3 demonstrates the healing process of IAs after treatment with a FD stent.

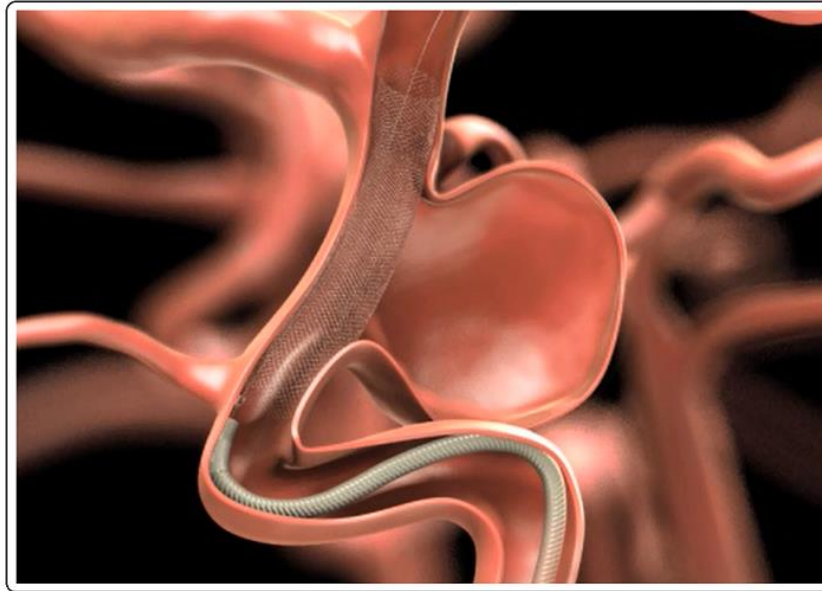


Figure 1-2: Endovascular treatment of IAs with an FD stent: the deployment procedure for a PED FD stent. [25]

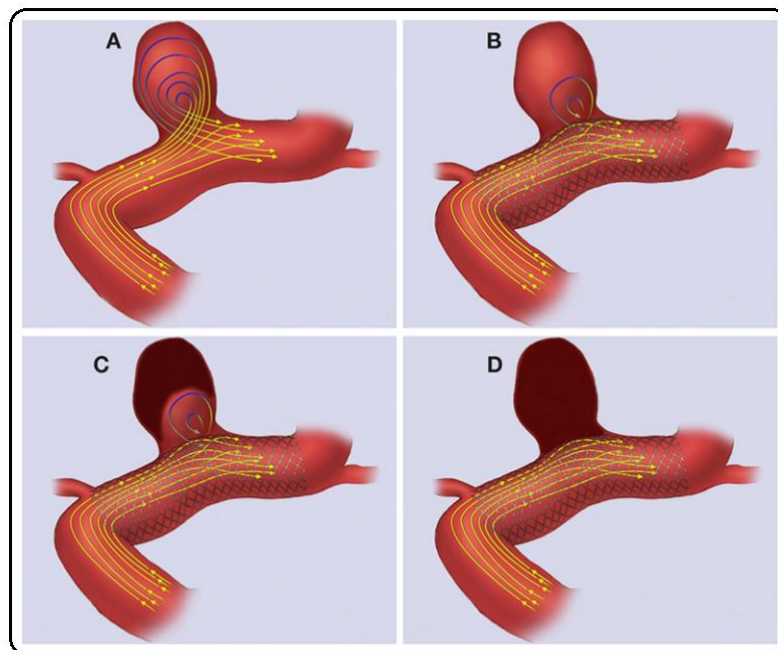


Figure 1-3: The healing procedure for IA treatments with a FD stent. A: the no-stent condition, B: immediately after FD stent deployment, C: partial occlusion of the aneurysm, and D: complete occlusion of the aneurysm. [26]

A number of manufacturers provide different brands of FD devices on the market — the pipeline embolization device (*PED*, Covidien, Irvine, USA), the *Silk/Silk+* FD device

(Balt International, Montmorency, France), the *Surpass* FD (Stryker Neurovascular, Fremont, USA), the flow-redirection endoluminal device (*FRED*, MicroVention, Tustin, USA), *etc.* Figure 1-4 shows the geometries of different brands of FD devices.

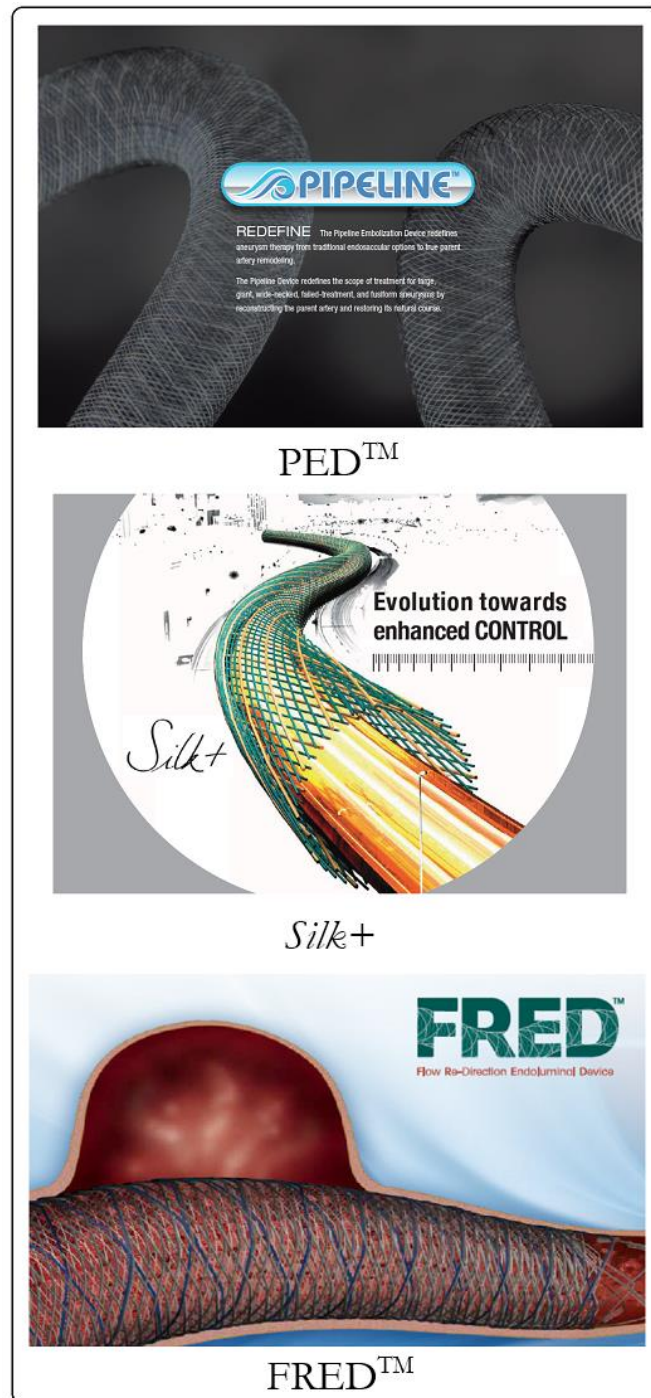


Figure 1-4: Three representative brands of FD stent: the *PED* (top) [25], the *Silk+* (middle) [27], and the *FRED* (bottom) [28].

1.3 Fluid Flow Simulation

It has been decades since computational fluid dynamics (CFD) simulation was first applied to the study of aneurysmal haemodynamics [29–41]. As a subfield of fluid mechanics based on numerical analysis and data structures, CFD can be used to resolve the intra-aneurysmal flow patterns qualitatively and quantitatively. The application of CFD seeks to help analyse the correlation between fluid mechanics and vascular wall biology, which is thought to be an important factor related to the central pathogenesis of aneurysm growth and rupture [37,42].

With the improvement of medical imaging accuracy, the geometries of the human vascular system, such as the shape of an IA with its parent artery, can be accurately reconstructed from anatomical images, which has promoted CFD simulations in the study of IAs.

For simulations of blood flow in large arteries, most CFD studies model the blood as an incompressible Newtonian fluid, in which the fluid is treated as continuous; thus, the three-dimensional Navier–Stokes equations can be discretised with a variety of methods, *e.g.* finite volume method (FVM), finite element method (FEM), finite difference method (FDM), *etc.* Recently, a mesoscopic method — the lattice Boltzmann method (LBM), which uses a discrete Boltzmann equation to solve the flow with collision models — has also been implemented [43].

Other sophisticated approaches have also been reported recently [44], which are believed to be able to more accurately approximate the blood flow: *e.g.* blood flow being simulated as a non-Newtonian fluid; CFD simulation being performed with a fluid–structure interaction (FSI) model, *etc.* Nevertheless, the imposition of high computational cost and the lack of knowledge about the vascular elasticity, thickness, *etc.* means that those approaches remain challenging.

1.4 Literature Review

With the aid of CFD simulations, various research has been presented in regard to the exploration of aneurysm initiation, progression, risk of rupture, and endovascular treatments.

1.4.1 Haemodynamic simulation of flow in the Circle of Willis

CFD simulations of blood flow in the Circle of Willis (CoW) were first performed to investigate the possible pathogeneses from the viewpoint of arterial haemodynamics. Alnaes *et al.* [44] reported that redistribution of wall pressure and wall shear stress (WSS) can be induced by anatomical deviations of brain arteries. To explore the correlation between the WSS changes and aneurysm initiation, Bammer *et al.* [45] and Wetzel *et al.* [46] found that arterial WSS distribution at the most common locations, especially the arterial bifurcations where IAs initiate and progress, have zones of either increased or decreased WSS. This phenomenon may be caused by flow swirling, also known as the “secondary flows”, induced by the curvature of cerebral arteries.

1.4.2 CFD simulation of aneurysmal haemodynamics

CFD studies of intra-aneurysmal circulation elucidate the flow patterns in which blood enters, circulates, and exits a variety of aneurysms of different morphologies [29,42,47–53]. The intra-aneurysmal flow circulations can be simple, with only a single recirculation zone or a single vortex structure existing within the aneurysm lumen; on the flip side, the circulations can also be complex, with recirculation regions that are unstable or become intermittent during a cardiac cycle [42,54,55]. Moreover, following from the structure of the aneurysm parent artery, strong aneurysm inflow jets can be induced. Studies confirmed that impingement of those inflow jets against the aneurysm wall can induce locally elevated pressure and WSS.

1.4.3 Haemodynamic parameters proposed for examining the IA flow

Numerous haemodynamic parameters have been calculated from CFD simulations to understand the mechanism of IA rupture and occlusion; they are WSS-related parameters (*e.g.* the maximum intra-aneurysmal WSS, low WSS area, WSS gradient), oscillatory shear index (OSI), residence time (RT), energy loss (EL), *etc.* [34,56–61]. For IA rupture, despite the fact that IA morphological parameters (*i.e.* notably the aspect ratio) are conventionally accepted as the primary indicator, WSS distribution, OSI, and number of vortexes were also reported to be associated with rupture [54,62–65]. Recently, a concept of EL, referring to the energy difference of the flowing fluid between entering and exiting an aneurysm, was put forward as a strong indicator of aneurysm rupture [31,36,66,67]. Furthermore, to predict a short-term aneurysm occlusion, many parameters were put forward, including the average or maximum intra-aneurysmal velocity (AAV/MAV), and intra-aneurysmal mass flowrate (MF) [56,68–73].

1.4.4 Modelling of endovascular treatment for IAs

Methodologies for modelling the process of FD treatment have also been studied in the past decade. There are two main elements of study: deployment, and flow diversion after deployment. Appanaboyina *et al.* [74] and Larrabide *et al.* [75] developed a virtual FD deployment technique using a deformable shape model, which realised the geometrical deployment of FD-like devices. Employing a finite-element method, Bernardini *et al.* [76] also realised the simulation of virtual FD deployment. Ma *et al.* [77–80] reported a virtual treatment technique, “HiFiVS”, to model the FD deployment procedure, and confirmed its good validity by comparing the wire structure to that deployed *in vitro*. To expedite the virtual deployment simulation, Janiga *et al.* [81] proposed a free-deformation method, and Peach *et al.* [82–84] introduced a spring–mass model to the virtual stenting simulation.

1.4.5 Optimisation studies in relation to FD treatment

On the basis of those computational techniques, applying CFD simulation to the optimisation of FD treatment has been pursued by many groups. The optimisation of FD treatment generally consists of two aspects — the optimal design of FD devices and the optimisation of treatment strategies.

Prior studies have attempted to investigate the effect of stent strut positions on flow-diversion efficacy [68,70,73,85]. Although some of those studies were performed based on a two-dimensional analysis, the concept of a bundle of inflow (BOI) has been established to correlate an efficient stent design with the AAV achieved post-treatment. Anzai *et al.* [70] suggests that the disruption of the BOI may markedly reduce the AAV according to an optimisation procedure performed on several idealised aneurysm geometries. Moreover, Lee *et al.* [85] confirmed the importance of device porosity and pore-density in reducing the aneurysmal inflow. In these studies, optimisation approaches, such as simulated annealing (SA) and the exploration of design space, started to show their benefits in a favourable stent structure design.

Besides optimisations applied to stent structure design, optimisation of treatment procedure was also proposed to assist neuroradiologists in treatments using the current commercially available stents. Janiga *et al.* [72] reported an automated CFD-based optimisation principle, aiming at finding a deployment scheme that could maximally block the aneurysmal inflow. Xiang *et al.* [80] compared the haemodynamic changes between treatments performed in a conventional way and with a dynamic ‘push-and-pull’ technique applied. These studies indicate the benefits of examining haemodynamic alterations prior to the real treatment in determining a favourable treatment plan.

1.5 Research Objectives

1.5.1 Existing problems

Review of a wider literature suggests that several problems exist in the design and deployment of FD stents. Those problems could plausibly be classified into the following four categories.

1.5.1.1 Complications related to inadequate flow diversion.

Inadequate flow diversion accounts for most treatment failures, including notably incomplete aneurysm occlusion and post-treatment aneurysm rupture [30]. A successful FD treatment depends heavily upon a sufficient ‘re-direction’ of aneurysmal inflow, such that blood clotting inside an aneurysm could be promoted.

In contrast to a favourable modification of aneurysm haemodynamics, FD stents could often produce adverse haemodynamic changes, such as a rather stronger aneurysmal inflow and an elevated pressure within the aneurysm sac, causing treatment failure [54].

1.5.1.2 Complications related to unsuitable device selection and deployment.

Size mismatch between the FD device and its recipient artery, together with the morphological alteration affected by deployment strategy (*e.g.* stent compaction, *etc.*), can result in tragedy [55,86,87]. For instance, deployment of an under-sized device may cause post-treatment stent migration; aggressively compacting an FD stent may push the stent wires into the aneurysm lumen, causing aneurysm rupture [88]. Furthermore, even if stents are ideally deployed, considerable flow-diversion difference exists between treatments using various stent diameters, which can affect the flow-diversion efficacy by up to 50 %, as reported by Mut *et al.* [87]

1.5.1.3 Complications related to bio-reactions against the implanted device.

The exposure of a FD stent’s metal surface can induce the proliferation of endothelial and smooth muscle cells on the stent surface, which may result in post-treatment in-stent stenosis [89–93]. The stent wire, regardless of its material, acts as a foreign body

that induces inflammatory reactions including platelet adhesion, activation, and aggregation [94–98]. Nevertheless, the flow-diversion efficacy of current FD stents relies heavily on a dense wire configuration. It is therefore a paradox for manufacturers to pursue high flow diversion whilst protecting against stenosis.

1.5.1.4 Other complications.

Other complications accompany FD stent implantation, including notably perforator artery occlusion, FD-implantation-induced vascular endothelial injury, *etc.*, due to the nature of this treatment mode [99–102].

1.5.2 Objectives

Those imperfections of flow-diversion treatment indicate the necessity of a comprehensive study of FD stent design and treatment planning. To meet this need, important contributions can plausibly be made in the following two aspects.

1.5.2.1 Design optimisation of FD stent structures

First, despite that manufacturers provide a range of FD stents with different combinations of diameter and length, those stents available on the market are still made of uniform wire configurations. As patients may react differently to the local haemodynamic changes caused by the implanted device, treatment outcomes may therefore vary from one to another. To resolve this issue, designing stent wire structures that are tailored to the stent recipient may lead to a better overall treatment outcome as flow-diversion efficacy of the specifically designed FD stent can be maximised.

1.5.2.2 Treatment rehearsal of all prospective treatment strategies

Furthermore, various strategies and manoeuvres (*e.g.* multi-FD stent implantation and stent deployment with compaction) have been practised in the delivery and deployment procedure of FD stents. Along with the factor of stent size, the impacts of those treatment strategies on aneurysmal haemodynamic outcomes remain unknown prior to a specific treatment. A treatment rehearsal that surveys the proposed

treatment strategy may aid in identifying the best solution, as well as in providing a better comparison of benefit of treatment *versus* no treatment.

In this thesis, applying numerical methods, I seek to improve the individualised FD stent design and deployment procedure that would contribute to a favourable treatment outcome. Specifically, four main topics were particularly focused on: 1) the development of a method for stent structural optimisation; 2) haemodynamic simulations of FD treatment with stent compaction technique applied; 3) haemodynamic simulations of FD treatment with dual-FD stents implanted; and 4) investigating the effects of incomplete FD stent expansion on aneurysmal haemodynamics.

1.6 Thesis Contents

The contents of this thesis are outlined as follows:

- Chapter 1: an introduction of this study's background, a wide literature review of relevant published studies, followed by the proposal of this thesis's research objectives;
- Chapter 2: introductions of the materials and general numerical methods to be implemented in the following Chapters;
- Chapter 3: a structural optimisation study of patient-specific stent design by lattice-Boltzmann simulation and simulated annealing procedure in idealised and realistic aneurysm models;
- Chapter 4: a haemodynamic study of flow-diversion treatment with compaction technique applied to FD stents of different diameters in successfully and unsuccessfully treated aneurysms;
- Chapter 5: a haemodynamic study of flow-diversion treatment with multiple FD stents of different diameters deployed in successfully and unsuccessfully treated aneurysms;

- Chapter 6: an investigation of aneurysmal haemodynamics affected by incomplete stent expansion of different levels of severities occurring at different segments of the parent artery;
- Chapter 7: a comparison between different treatment strategies and the discussion of a treatment individualisation attempt via reviewing a set of prospective treatment plans; and
- Chapter 8: a conclusion of this study and an outlook for future works beyond this thesis.

Chapter 2

Materials and Methods

2.1 Aneurysm Model Geometries

2.1.1 Idealised aneurysm geometries

Two idealised aneurysm geometries (Figure 2-1) were employed in Chapter 3: one is a ‘straight’ model (S model), in which a saccular aneurysm (represented by a sphere) was initiated from a straight vessel (represented by a straight tube); the other is a ‘curved’ model (C model), in which the same ‘sphere’ saccular aneurysm is connected to a curved vessel (represented by a curved tube). Both aneurysm geometries were adopted from earlier published papers [49,55] and were constructed using Pro/ENGINEER (Wildfire 5.0, PTC, USA).

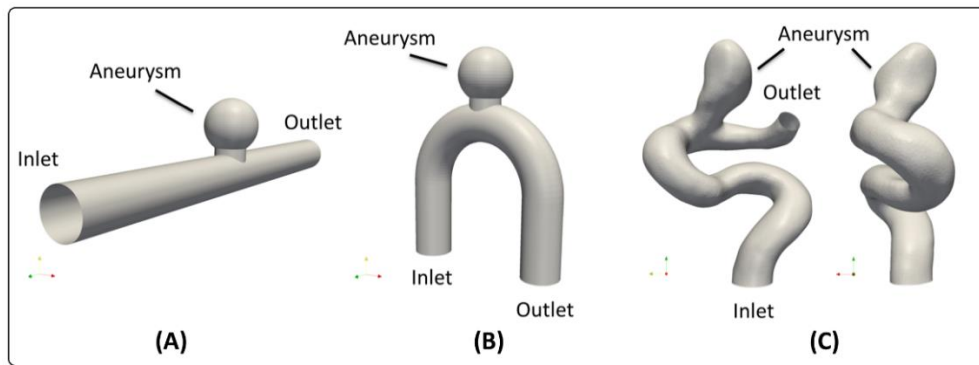


Figure 2-1: Idealised and realistic aneurysm models used in Chapter 3. A: the straight idealised model (S model), B: the curved idealised model (C model), and C: the realistic model (R model).

For both aneurysm models, the diameter of the aneurysm sac (D) is 4.8 mm, the diameter of the aneurysm neck (N) is 2.8 mm, and the arterial diameter (d_1) was 3.5 mm. The curvature radius (r) of the C model is 6.0 mm. These parameters were determined based upon the statistics reported in IA morphology studies [49].

2.1.2 From medical images to the 3D aneurysm models

Two-dimensional (2D) sliced medical images, *e.g.* DSA or CTA grey scale maps in DICOM format, *etc.* can be reconstructed into three-dimensional (3D) models using either commercial or open-source image processing packages, *e.g.* MIMICS (Materialise, Belgium) and VMTK [103]. This process is called 3D reconstruction, a

subject of computer vision and computer graphics, which captures the shape and appearance of a real object from its multiple 2D scans. The 3D IA models used in this thesis were reconstructed based upon a ‘contour interpolation’ strategy to generate 2D contours from greyscale values of pixels, with the 3D geometry segmented by interpolation of those 3D contours in the normal direction. This method is reported to be able to prevent the surface noise intrusion [104].

2.1.3 Realistic aneurysm geometries

Three realistic aneurysm models from patient medical scans were employed in this study. The first model is an ICA aneurysm that has been comprehensively studied in several published papers [38,59]. This aneurysm (referred to hereinafter as the ‘R model’) has an inlet diameter (d_2) of 3.8 mm, as shown in Figure 2-1.

The other two aneurysms were collected from the Neuroradiology Department at Monash Medical Centre (Melbourne, Australia), after proper institutional ethics approval was obtained. These two aneurysms were clinically observed and categorised respectively as a successfully treated case and an unsuccessfully treated one with the *Silk+* stents (Refer to Section 2.2.2 for detailed information). Complete aneurysm occlusion at the 6 months’ follow-up was set as the benchmark for a ‘successful’ treatment.

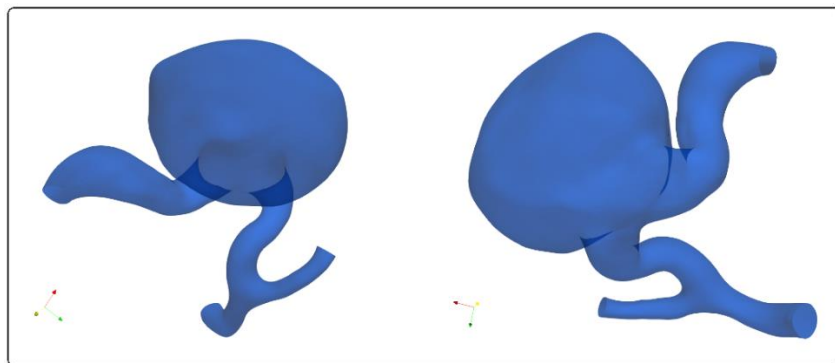


Figure 2-2: The geometry of the successfully treated patient aneurysm. (Figures on the left and on the right are the model visualised from different camera angles.)

For the successful case (Figure 2-2), CTA taken 6 months after treatment confirmed a complete occlusion of the aneurysm, whereas a large aneurysm lobule was found by CTA at the 6 months’ time point for the unsuccessful case (Figure 2-3). In a second

treatment, an additional *Silk+* stent was then deployed; however, CTA taken 6 months after the second treatment still revealed the continued existence of a residual aneurysm. The parent artery diameters ranged from 2.6 to 5.6 mm in the successful case, and from 2.2 to 6.2 mm in the unsuccessful case (Figure 2-4).

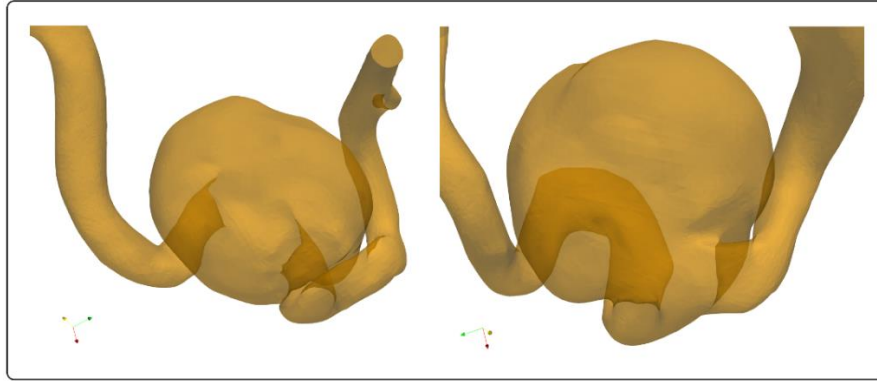


Figure 2-3: The geometry of the unsuccessfully treated patient aneurysm. (Figures on the left and on the right are the model visualised from different camera angles.)

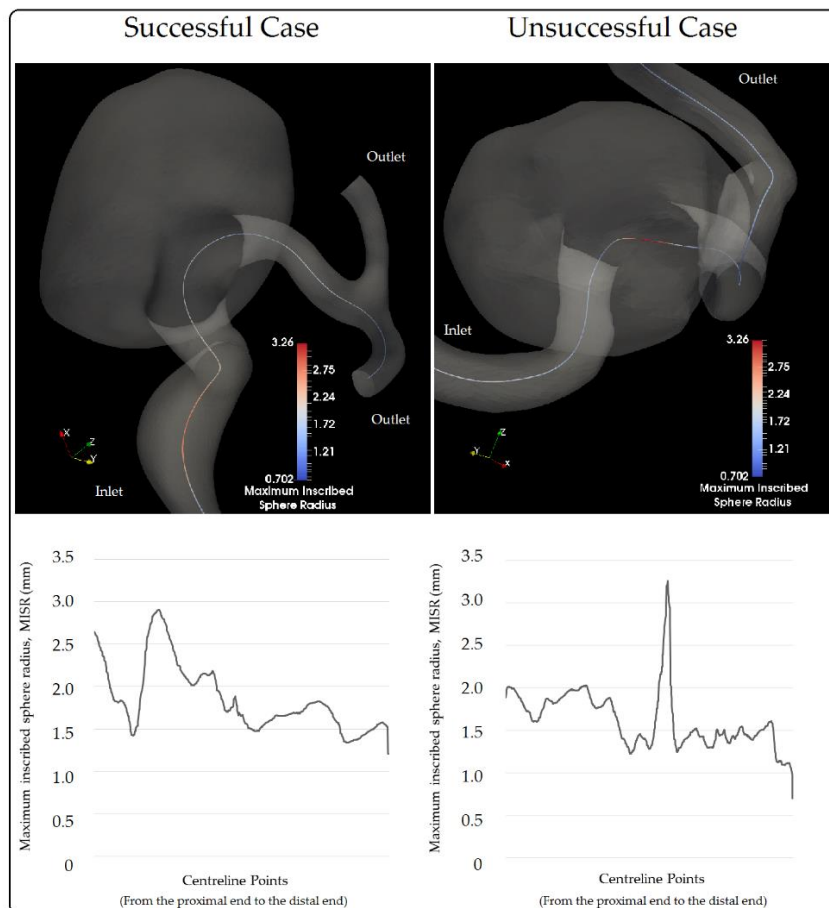


Figure 2-4: The maximum inscribed sphere radius with respect to the points along the centrelines of the successful case (left) and the unsuccessful case (right).

2.2 Flow-diverting Stents

Many brands of FD stent are available on the market, which mainly include the pipeline embolization device (*Pipeline*, Covidien, Irvine, USA), the *Silk+* FD device (Balt International, Montmorency, France), the *Surpass* FD (Stryker Neurovascular, Fremont, USA), and the flow-redirection endoluminal device (*FRED*, MicroVention, Tustin, USA)

2.2.1 Pipeline Embolization Device

A *Pipeline* stent (see Figure 2-5) intervention is indicated for the endovascular treatment of adults with large or giant wide-necked IAs in the ICA from the petrous to the superior hypophyseal segments. The device is composed of 48 braided strands, which are made from a combination of 75% cobalt chromium and 25% platinum tungsten, and a soft low-profile distal tip for flexible conformability. The manufacturer provides *Pipeline* stents with different stent diameters (ranging from 2.5 to 5.0 mm with an increment interval of 0.25 mm) and lengths (ranging from 10 to 35 mm). When the crimped device reaches its nominal diameter, the metal coverage ratio (MCR) should be a value between 30% and 35%. In addition, this device is fully re-sheathable and can be positioned and redeployed up to two times [105].

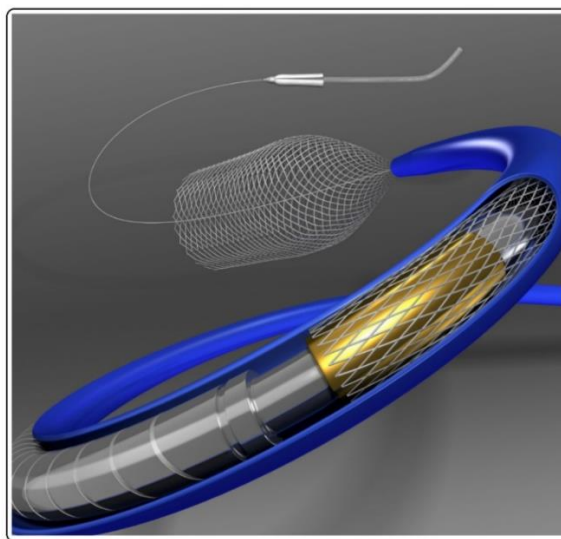


Figure 2-5: Schematic of the commercially available packaging of the *Pipeline* stent. [25]

2.2.2 Silk stent

The *Silk+* FD stents (see Figure 2-6) are also high-density braided stents for the treatment of IAs, which have an increased radial force of 15%, compared to the original *Silk* stents, for facilitating the deployment and vessel wall apposition in challenging anatomies. The *Silk+* was designed with higher radio-opacity for an increased visibility during and after deployment through 4 radio-opaque markers that run along the entire body of the stent, and 6 extra smaller platinum wires to enable the visualisation of the stent bodies. The manufacturer provides a set of stent sizes, with the stent diameter ranging from 2.0 to 5.5 mm, and the length from 15 to 40 mm. A unique feature of the *Silk+* stent is that ‘tapered’ stents are provided on the market for those aneurysms with a big size mismatch between the proximal and distal landing zones. The *Silk+* is re-sheathable and re-positionable before 90% of the crimped stent length has been deployed.

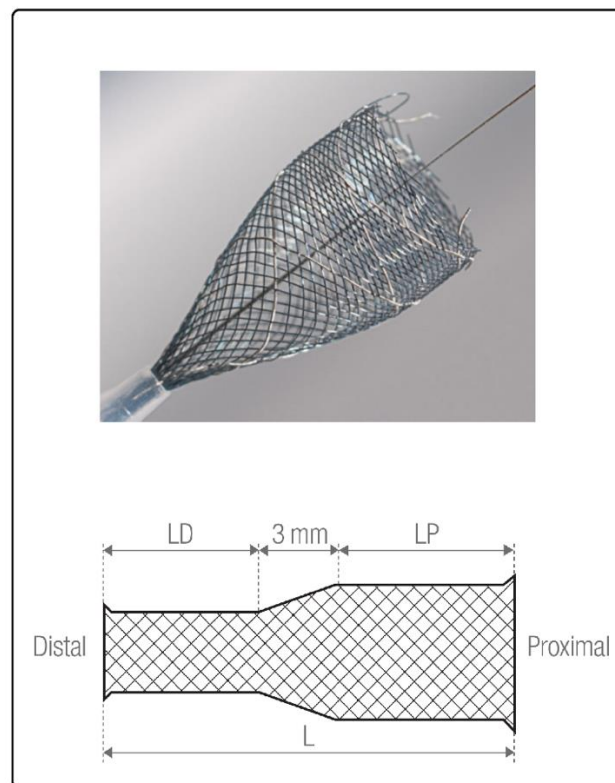


Figure 2-6: (Top) The commercially available *Silk+* stent. (Bottom) Schematic of the tapered *Silk+* stent with different diameters designed for the distal landing zone (LD) and the proximal landing zone (LP). [27]

2.2.3 Flow-Redirection Endoluminal Device

The *FRED* system (see Figure 2-7) is claimed to be next generation flow diversion device intended for the treatment of IAs. The *FRED* is a capaired, integrated dual-layer (stent-within-a-stent) self-expanding Nitinol braided design simultaneously deployed by a single-operator micro-catheter. The higher radial force outer stent (16 wires), and the low porosity, high metal surface area inner stent (48 wires with a MCR between 22% and 44%), unite to provide the ease of use, enhanced stent opening, improved vessel apposition and fluoroscopic visibility. The *FRED* system is reported to offer additional benefits over first generation flow diversion devices, by its ability to be partially deployed, retrieved and accurately repositioned or redeployed, without the need for a torque device. The manufacturer provides devices with fully opened diameters ranging from 2.5 mm to 5.5 mm, and total lengths between 7 and 38 mm.

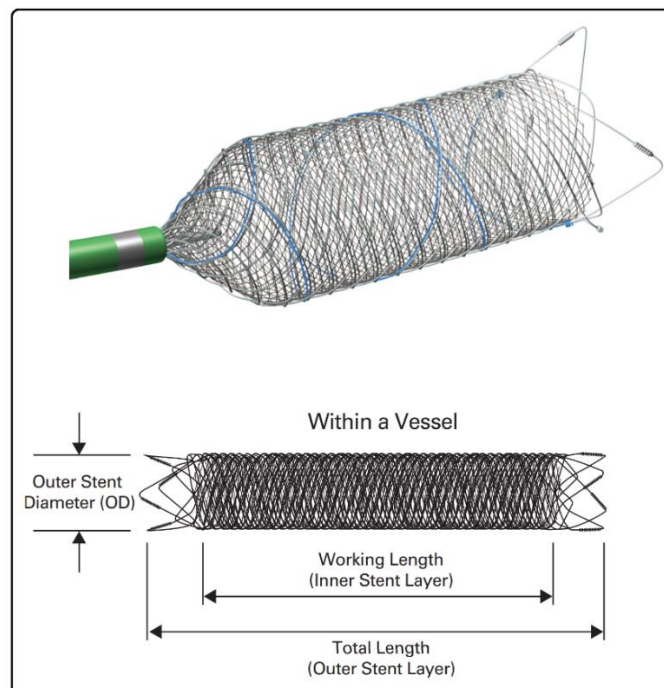


Figure 2-7: (Top) The commercially available packaging of the *FRED* system. (Bottom) Configuration of the outer and the inner stent layers. [28]

2.2.4 Other endovascular devices

Other FD stents, including notably the *Surpass* FD stent, have also been invented and introduced to the market. They are all made from braided metal wires, with different combinations of number of wires, thickness of wire, number of layers, *etc.*

2.3 Virtual Stent Deployment

To simulate the FD stent deployment procedure, a recently reported and validated algorithm, namely the spring–mass analogue, was adopted for its reasonable computational load and acceptable validity of simulation results [82–84,106–108].

2.3.1 Spring–mass analogue

The adopted spring–mass analogue was based on a set of simplifications:

- 1) FD strut wires were approximated by centrelines without an explicit thickness;
- 2) a FD wire intersection (node) was approximated by a mass point, which was fictitiously connected to its neighbours by springs;
- 3) the stiffness of each spring was associated with the length and thickness of the represented wire strut.

In this manner, a FD stent can be represented by a collection of springs and mass points; the structure of a FD stent and the internal forces acting inside the FD stent could therefore be mathematically represented and measured.

2.3.2 Modelling the restoring forces acting inside a FD stent

In the spring–mass system, interactions between mass points (nodes) can be calculated following Hooke’s law:

$$F_i = \sum_{j=1}^{n_i} k_{ij}(\delta_j - \delta_i), \quad (2 - 1)$$

in which F_i denotes the restoring force imposed on node i by its directly connected neighbour nodes; δ_i denotes the displacement of node i ; k_{ij} stands for the stiffness of the fictitious spring connecting node i and its neighbour j , which was determined as $2.09 \times 10^3 \text{ Nm}^{-1}$ [84] in the present study; and n_i is the number of nodes directly connected to node i .

2.3.3 Simulation of virtual stent deployment

I assumed that a FD stent was initially crimped in alignment with the centreline of the parent artery, and then expanded to its load-free status, driven by the restoring forces acting internally and controlled by a contact detection algorithm which keeps the nodal movements a chosen distance away from the arterial wall. I assumed that a fully expanded status was reached when there was almost no change in the FD nodal coordinates. Finally, a FD model was obtained from the nodal information by sweeping a circular cross-section through the centreline of each wire using Paraview [109].

The virtual stent deployment pseudocode [107] adopted in the thesis is as follows:

1. Initialisation of stent node displacement by subtracting the load-free coordinates of FD stent nodes from the current crimped coordinates. For a stent node $v_i = (x_i, y_i, z_i)'$, the initial crimping delta δ_i^{cr} is calculated by:

$$\delta_i^{\text{cr}} = \begin{pmatrix} \delta_{x_i}^{\text{cr}} \\ \delta_{y_i}^{\text{cr}} \\ \delta_{z_i}^{\text{cr}} \end{pmatrix} = \begin{pmatrix} x_i^{\text{cr}} \\ y_i^{\text{cr}} \\ z_i^{\text{cr}} \end{pmatrix} - \begin{pmatrix} x_i^{\text{lf}} \\ y_i^{\text{lf}} \\ z_i^{\text{lf}} \end{pmatrix} \quad (2-2)$$

2. Iteration until there is almost no change in expansion delta:

- a. Calculation of restoring force F_i for each node according to

$$F_i = \sum_{j=1}^{n_i} k_{ij} (\delta_j^{\text{cr}} - \delta_i^{\text{cr}}) \quad (2-3)$$

- b. Calculation of expansion delta δ_i^{exp} for each node i from force and nodal stiffness:

$$\delta_i^{\text{exp}} = -\frac{F_i}{\sum_{j=1}^{n_i} k_{ij}} \quad (2-4)$$

- c. Check the nodal coordinates after expansion δ_i^{exp} , to see if the node would still be within the vascular boundary (*i.e.* contact detection).
- d. Update the nodal coordinates for those that passed the contact detection:

$$\begin{pmatrix} x_i^{\text{cr}} \\ y_i^{\text{cr}} \\ z_i^{\text{cr}} \end{pmatrix} = \begin{pmatrix} x_i^{\text{cr}} \\ y_i^{\text{cr}} \\ z_i^{\text{cr}} \end{pmatrix} + \begin{pmatrix} \delta_{x_i}^{\text{exp}} \\ \delta_{y_i}^{\text{exp}} \\ \delta_{z_i}^{\text{exp}} \end{pmatrix} \quad (2-5)$$

- e. Update crimping delta values δ_i^{cr} by adding expansion displacement $\delta_{x_i}^{\text{exp}}$ to the previous δ_i^{cr} :

$$\delta_i^{\text{cr}} = \begin{pmatrix} \delta_{x_i}^{\text{cr}} \\ \delta_{y_i}^{\text{cr}} \\ \delta_{z_i}^{\text{cr}} \end{pmatrix} = \begin{pmatrix} \delta_{x_i}^{\text{cr}} \\ \delta_{y_i}^{\text{cr}} \\ \delta_{z_i}^{\text{cr}} \end{pmatrix} + \begin{pmatrix} \delta_{x_i}^{\text{exp}} \\ \delta_{y_i}^{\text{exp}} \\ \delta_{z_i}^{\text{exp}} \end{pmatrix} \quad (2-6)$$

3. Generation of FD stent structure using Paraview.

2.4 Haemodynamic Simulation

Haemodynamic simulations were performed for this thesis to resolve the aneurysmal blood flow behaviours using computational fluid dynamics (CFD) methods.

2.4.1 Computational grid generation

In CFD simulations, computational grid generation is always a troublesome procedure, because it drastically affects the validity of simulation results. Computation grid generation is the practice of generating a polygonal or polyhedral mesh that approximates a geometric domain. The term “mesh generation” is used interchangeably. The computational grids are mainly classified into three categories: 1) structured grids, which are identified by regular connectivity, *e.g.* Cartesian grids, rectilinear grids, *etc.*; 2) unstructured grids, which are identified by irregular connectivity, *e.g.* computational grids made of tetrahedra, pyramids, prisms,

hexahedra, *etc.*; and 3) hybrid grids, which contain a mixture of structured portions and unstructured portions.

The computational grids generated in Chapter 3 were Cartesian grids that could be coupled with the subsequent lattice Boltzmann simulation, due to the consideration of a huge computational load. The computational grids generated in Chapter 4, 5, and 6 were tetrahedral grids, to better describe the geometries of FD stents after deployment.

2.4.2 Computational fluid dynamics methods

2.4.2.1 Lattice-Boltzmann method

The lattice Boltzmann method (LBM) is a modern CFD approach which is often used to solve the incompressible, time-dependent Navier–Stokes equations. It is reported to be capable of easily representing complex physical phenomena, *e.g.* multiphase flows, and chemical interactions between the fluid and the surroundings [110–118].

LBM is a mesoscopic approach in which fluid is described in terms of the density distribution $f_i(r, t)$ of idealized fluid particles moving and colliding on a regular lattice. These collision–propagation dynamics can be written as

$$f_i(r + v_i \Delta t, t + \Delta t) = f_i(r, t) + \frac{1}{\tau} (f_i^{\text{eq}} - f_i), \quad (2 - 2)$$

where f^{eq} and τ are known as the local equilibrium distribution and relaxation time, respectively.

I adopted LBM as the CFD solver in Chapter 3, owing to the following advantages of LBM: primarily, the data pre-processing and computational grid generation can be automated in a time that accounts for a small fraction of the total simulation; secondly, the numerical simulation could be executed well in parallel, which enables the simulated annealing (SA) procedure (refer to Section 3.2.4) to process a thousand steps of CFD results.

2.4.2.2 Finite volume method

The finite volume method (FVM) is a method for the representation and evaluation of partial differential equations (PDE) in the form of algebraic equations [119,120]. Similar

to other discretisation methods, including notably the finite difference method (FDM) and the finite element method (FEM), numerical values are calculated for the elements on the discrete computational grids. In the FVM, volume integrals in a PDE that contain a divergence term are converted to surface integrals, using the divergence theorem. These terms are then evaluated as fluxes at the surfaces of each finite volume, which refers to the small volume surrounding each node on the computational grids. Because the flux entering a given volume is identical to that leaving the adjacent volume, these methods are conservative. FVM is also easily formulated to allow for unstructured meshes, which has been integrated into many CFD simulation packages, including notably the ANSYS package (Canonsburg, USA).

The application of the FVM is to solve the Navier–Stokes equations, which describes the motion of viscous fluid substances. The general form of the steady state Navier–Stokes equation is

$$\rho u_j \frac{\partial u_i}{\partial x_j} = -\frac{\partial P}{\partial x_i} + \frac{\partial}{\partial x_j} \left[\mu \left(\frac{\partial u_i}{\partial x_j} + \frac{\partial u_j}{\partial x_i} \right) \right], \quad (2-3)$$

where ρ represents the density, P is the static pressure, $u_{i,j}$ are velocity components and μ is the dynamic viscosity.

The CFD simulations in Chapters 4, 5, and 6 were performed using the CFX solver in the ANSYS packages.

Chapter 3

Structural Optimisation of Flow-Diverting Stent

3.1 Objective

In the FD treatment of IAs, high flow-diversion efficacy is desired to accelerate thrombotic occlusion of the aneurysm. However, a risk of post-stenting stenosis is posed when flow diversion is pursued through FD design by a simple decrease of device porosity. A possible way to improve flow diversion, whilst keeping the device porosity at a high level, may be an individually designed FD stent with its wire structure tailored to accommodate a patient aneurysm.

The conventional FD stents, such as the *PED* and the *Silk+*, are all constructed from homogeneous helical metal filaments. In spite of attempts being made to improve the flow-diversion efficacy by optimisation [70,73,85], a feasible approach that can be applied to the manufacturing procedure has not yet been reported for FD stents braided from helical filaments.

In this Chapter, I try to meet this need by demonstrating an automated optimisation procedure performed on the conventional helical FD stents. At first, the FD stent and patient aneurysm models were constructed; and then a random modification strategy was designed, and a CFD-simulation-based simulated annealing procedure was employed to control the random modification progressing towards an optimal solution. Finally, this optimisation approach was applied to three different aneurysms to investigate the stent structures and aneurysm haemodynamics before and after optimisation.

3.2 Methods

Figure 3-1 demonstrates the workflow of the proposed optimisation procedure, which mainly comprises the reconstruction of IA geometry, the modelling of FD stents, the strategy of random modification, the technique of CFD simulation, and the process of simulated annealing.

3.2.1 Aneurysm geometries

Aneurysmal local haemodynamics is sensitive to the morphology of the parent artery. To investigate the effectiveness of the proposed optimisation strategy under different haemodynamic conditions, I employed three aneurysm models — an idealised straight model (S), an idealised curved model (C), and a realistic aneurysm model (R) located at the internal carotid artery (ICA). The detailed descriptions and information about these three models can be found in Chapter 2.1.

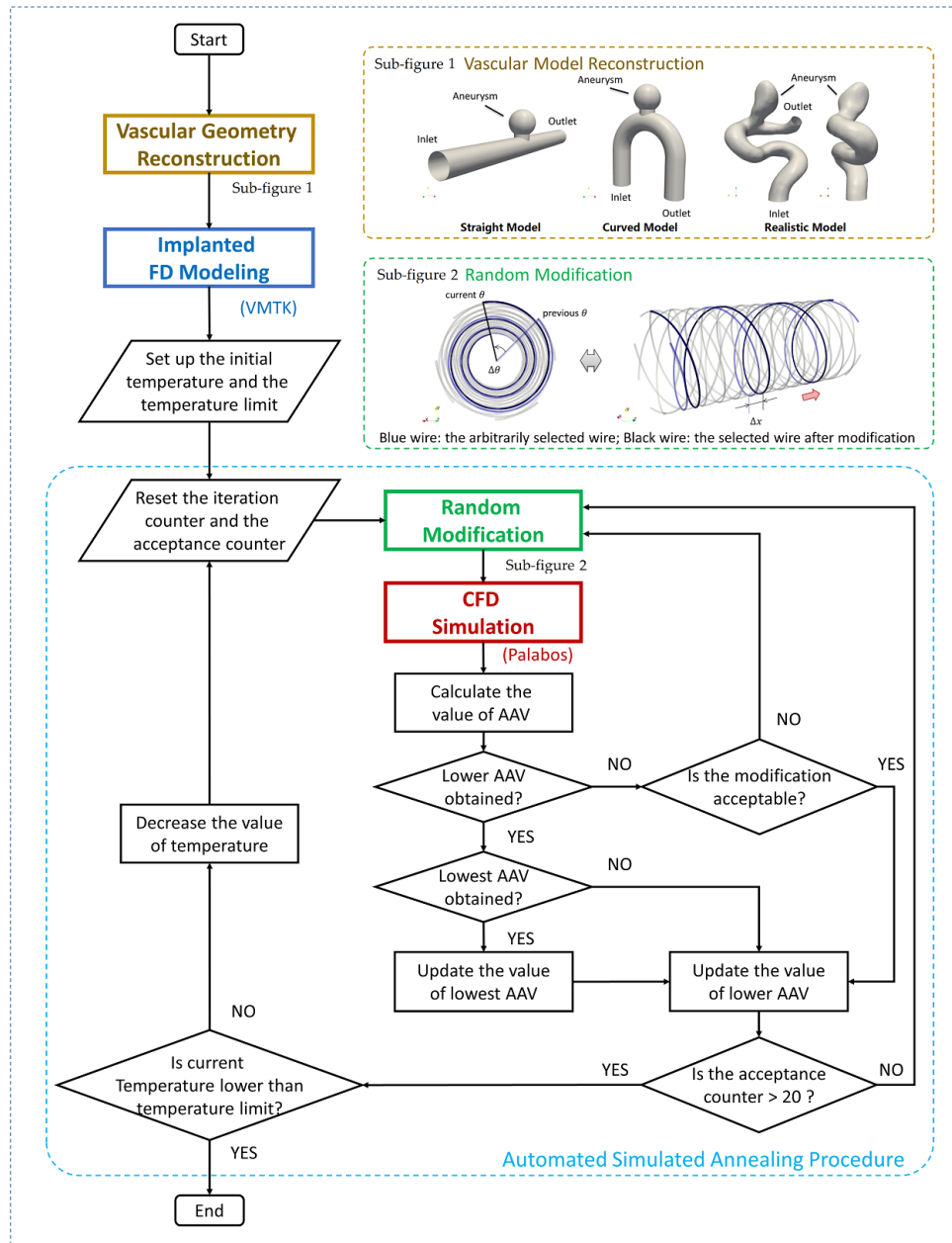


Figure 3-1: Schematic of the proposed optimisation procedure.

3.2.2 FD stent model

FD stents available on the market comprise clockwise and anti-clockwise woven wires with uniform starting phase arrangements. The starting phase of a wire filament refers to the location, corresponding to the centreline point of the FD stent's proximal or distal end, where the filament starts to be braided from (see Figure 3-2).

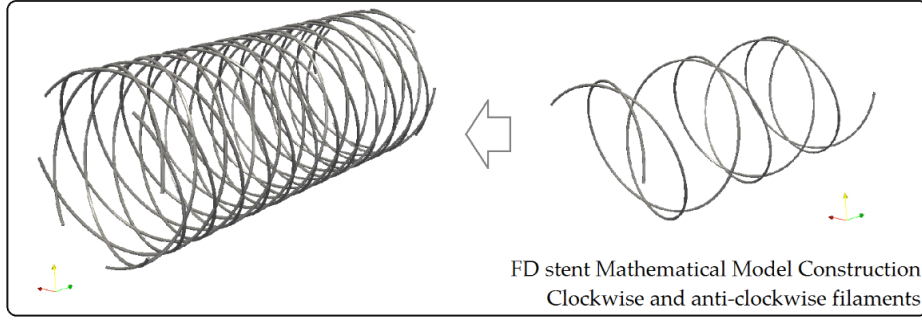


Figure 3-2: From clockwise and anti-clockwise helix filaments to an FD stent.

I therefore constructed the stent's mathematical description as a set of helices, using equations:

$$\text{Clockwise: } \begin{cases} x = [R + r \cdot \sin(\omega_\alpha + \theta_n)] \cdot \cos(\omega_\beta) \\ y = [R + r \cdot \sin(\omega_\alpha + \theta_n)] \cdot \sin(\omega_\beta) \\ z = r \cdot \cos(\omega_\alpha + \theta_n) \end{cases} \quad (3-1)$$

$$\text{Anti-clockwise: } \begin{cases} x = [R + r \cdot \cos(\omega_\alpha + \theta_m)] \cdot \cos(\omega_\beta) \\ y = [R + r \cdot \cos(\omega_\alpha + \theta_m)] \cdot \sin(\omega_\beta) \\ z = r \cdot \sin(\omega_\alpha + \theta_m) \end{cases} \quad (3-2)$$

where r is the maximal inscribed sphere radius (MISR) for the represented point along the helix, and R is the curvature radius of the aneurysmal parent artery centreline at the corresponding point; ω_α and ω_β are parameters respectively associated with the length and pitch of a helix; and θ_n or θ_m indicates the starting phase of a clockwise or anti-clockwise helix. The MISR and curvature radius varied with respect to the discrete points along the centreline of the parent artery. The coordinates of these discrete points and their corresponding MISRs were measured using the vascular modelling toolkit (VMTK version 1.2).

Considering the huge imposition of computational cost in the following CFD-based random modification, the test FD stent was assumed to consist of 8 wires: 4 clockwise

and 4 anti-clockwise. The initial stent has a uniform wire configuration and the starting phases of stent wires (as in Figure 3-2) are defined as

$$\theta_n = 2(n - 1) \cdot \frac{\pi}{4} \quad \text{and} \quad (3 - 3)$$

$$\theta_m = 2\left(m - \frac{1}{2}\right) \cdot \frac{\pi}{4}, \quad (3 - 4)$$

where n or $m \in (1, 2, 3, 4)$ indicates the sequence of either the four clockwise (n) or the four anti-clockwise (m) helical subsets.

3.2.3 Random modification of FD stent structure

A slight alteration of a helix's starting phase can result in a longitudinal displacement of the helix; the shape of this helix can be maintained during the displacement procedure (see Figure 3-3 for a demonstration). In order to keep the FD stent porosity unchanged, the starting phases of FD stent wires were therefore adopted to be the objects of optimisation.

In one step of random modification, a helix was arbitrarily chosen, and a stochastic variable

$$\Delta\theta \in \left(-\frac{\pi}{8}, \frac{\pi}{8}\right) \quad (3 - 5)$$

was then added to the starting phase θ (either θ_n or θ_m) of the selected helix:

$$\theta_{\text{current}} = \theta_{\text{previous}} + \Delta\theta \quad (3 - 6)$$

In this manner, the modification resulted in an axial displacement of the arbitrarily selected helix along the centreline of the parent artery, whereas the device porosity remained unchanged.

3.2.4 Simulated annealing

A simulated annealing (SA) procedure was employed to lead the random modifications to progress towards the optimal solution. The SA procedure is a probabilistic technique for the approximation of the global optimum of a given

function, *e.g.* the intra-aneurysmal average velocity (AAV) as determined in the present study, which involves the evaluation of states of the so-called neighbours, *i.e.* the FD wires' structure after one-stage random modification in this study.

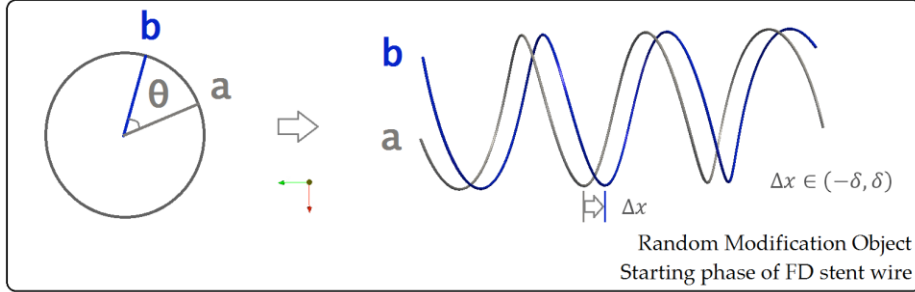


Figure 3-3: Demonstration of starting phase changes resulting in longitudinal displacements of a helix.

At each step of SA, some neighbouring states, *i.e.* a set of FD stent structures post random modification, of the current state, *i.e.* the FD stent structure based on which random modifications were performed, were considered, and then whether the “system” would move to one of the neighbouring states or stay in the current state was decided by a probability. The probabilities would lead the system to tend to move to states of lower energy, which would usually be repeated until the system reaches a state that is good enough for the application, or until a given computational budget has been exhausted.

Table 3-1: Initial temperatures and lower temperature limits for respectively the S, C, and R models.

	S model	C model	R model
Initial Temperature	6.02×10^{-5}	1.27×10^{-4}	1.01×10^{-3}
Lower Temperature Limit	1.08×10^{-7}	2.28×10^{-7}	1.81×10^{-6}

In the present study, the optimisation began with the homogeneous FD stent structure, with an initial temperature assigned, and was completed when the lower temperature limit was reached. The initial and the lower temperature limits were determined for a specific case following this strategy: 1) at first, one hundred random modifications were performed without the control of the SA algorithm; 2) based on the random modification results, the mean alteration of the objective parameter was then calculated to assign the initial temperature an acceptance probability of 0.5; and 3) the SA procedure was assumed to involve 60 decrements and each decrement has a

decreasing ratio of 90 %, compared to the temperature of the previous state. Following this strategy, the initial temperatures and the lower temperature limits for respectively the S, C, and R model were calculated as shown in Table 3-1.

3.2.5 Haemodynamic simulation

After each step of random modification, a CFD analysis was performed to measure the change in the objective function(s). Considering that the SA procedure can take up to one thousand steps of random modification, the computational cost of the following CFD simulation becomes a troublesome issue, especially when dealing with models described by a large amount of computational meshes, *e.g.* a realistic aneurysm geometry.

An automated open-source LBM library, Palabos (version 1.4) [121] was adopted, for its good flexibility and readiness for parallelisation. Because CFD simulation with Palabos requires a Cartesian mesh, manual computational grid generation was then avoided, which contributed to the complete automation of the entire optimisation procedure. A standard D3Q19 lattice topology was employed to describe the fluid lattices within the fluid domain. A spatial discretisation of 0.05 mm was determined, after a mesh dependency test was carried out, in which no obvious distinctions of intra-aneurysmal average velocity and flow patterns were found after the lattice grid resolution was doubled. With these parameters assigned, the number of fluid cells for the respective S, C, and R models were 3.57×10^6 , 3.01×10^6 , and 4.06×10^6 .

The blood was assumed to be an incompressible Newtonian fluid, with density and kinematic viscosity set as 1040 kg/m^3 and $4.0 \times 10^{-6} \text{ m}^2/\text{s}$. A bounce-back rule was implemented to impose a no-slip wall boundary, as well as to define the FD stent models. Inlet velocities of 0.23 m/s, 0.23 m/s, and 0.21 m/s were defined as parabolic profiles for respectively the S, C, and R models; a constant 0 Pa pressure boundary was imposed at all outlets. With these settings, the kinetic viscosity of the lattice (ν_{LB}) was chosen as 0.012, giving a relaxation time τ of $(6\nu_{LB} + 1)/2 = 0.536$. The convergence was assumed to be reached when the change in the average energy of fluid cells was less than $10^{-6} \text{ kg} \cdot \text{m}^2/\text{s}^2$.

To quantify the flow-diversion efficacy of a stent structure post random modification, an index of flow reduction rate (R_f) was defined:

$$R_f = \frac{V_{w/o} - V_{\text{withFD}}}{V_{w/o}} \times 100\%, \quad (3 - 7)$$

where $V_{w/o}$ and V_{withFD} are the intra-aneurysmal average velocities under no-stent condition and after FD implantation of a given wire configuration, respectively.

Considering the huge computational load, a scalar parallel computing system (SGI UV2000) was used at the Institute of Fluid Science, Tohoku University, to perform the CFD simulations. To reach a convergence in CFD simulation, the computational costs, using 256 cores, for respectively the S, C, and R models were about 30, 45, and 70 minutes.

3.2.6 Longitudinal displacement test

Manual delivery and deployment of an FD stent can lead to uncertain displacements along the longitudinal direction, in relation to the desired location identified by the optimisation. I therefore performed a longitudinal displacement test (LDT) to investigate the displacement effects on the post-treatment haemodynamics: for a given FD stent structure, the starting phases of all wires were changed by adding a variable θ_Δ , ranging from $-\pi$ to π , to produce an effect of longitudinal displacement. CFD simulations were then performed to obtain the intra-aneurysmal average velocities under displacement conditions.

3.2.7 Optimisation with different objective functions

Optimisation with different objective functions applied can produce different optimal solutions. To examine the effect of objective function on the optimal FD stent structure and its corresponding haemodynamic modifications, the same optimisation procedure was applied with intra-aneurysmal maximum velocity (AMV) set as the objective function to respectively the S and C model.

3.3 Results

3.3.1 Optimisation with the AAV objective function

It took respectively 916, 1035, and 976 SA steps before the lower temperature limits of the S, C, and R model were reached. In all three cases, a marked improvement of flow-diversion efficacy was observed in the initial hundred steps of SA, before it fluctuates and stabilises at a certain level, as demonstrated in Figure 3-4. the AAV differences before and after optimisation were presented in Table 3-2 for the three models.

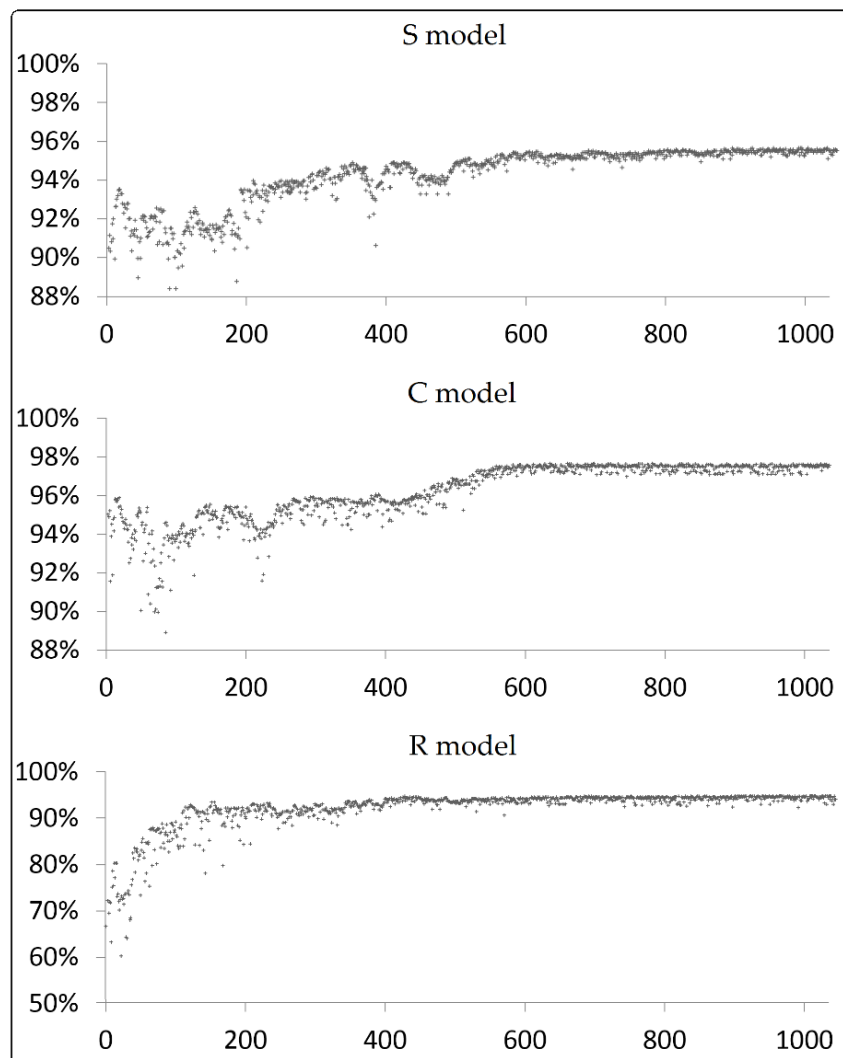


Figure 3-4: The SA procedures for the S, C, and R models. (Vertical axis: R_f , horizontal axis: steps of SA procedure.) Objective function: AAV.

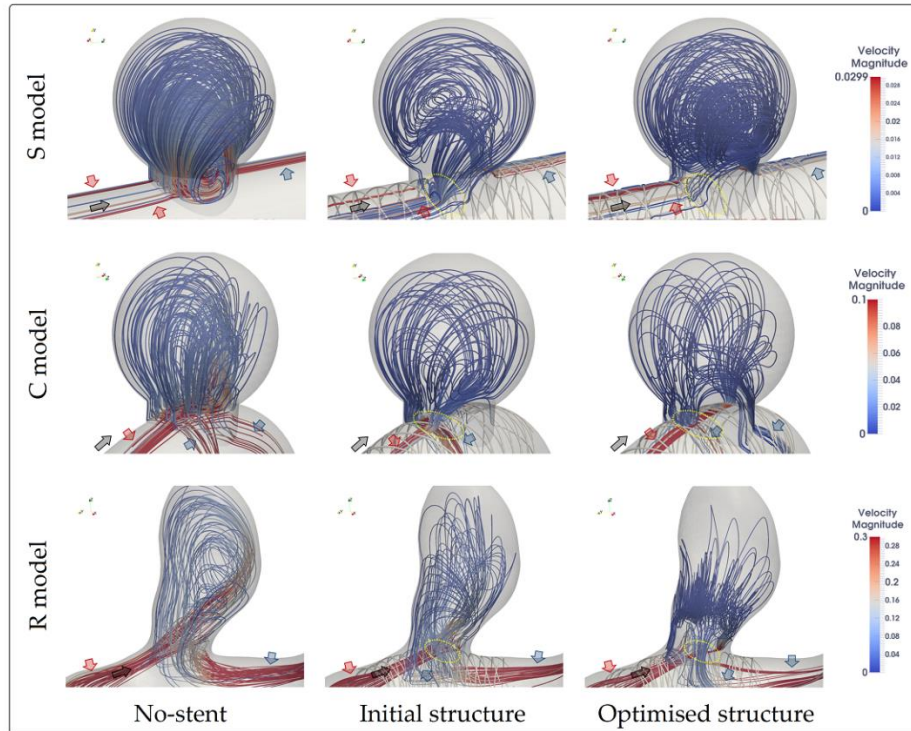


Figure 3-5: Visualisation of intra-aneurysmal streamlines, colour-coded by velocity magnitude, under no-stent conditions, and with stent before and after optimisations, for respectively the S, C, and R aneurysm models. (Black arrows: flow direction, red arrows: BOI, blue arrows: BOO, and yellow circles: inflow area.)

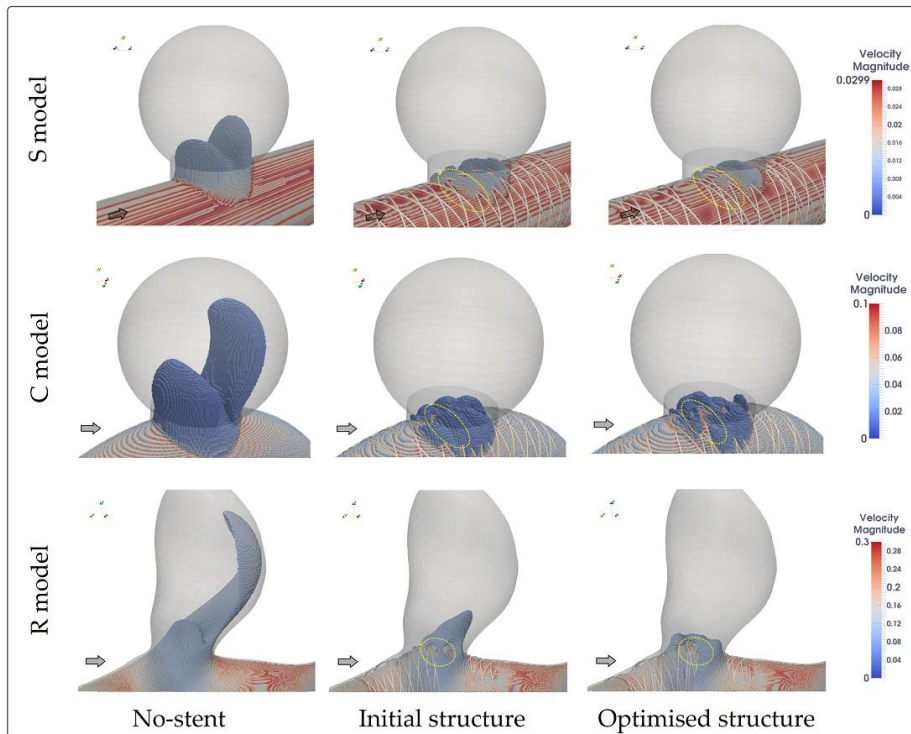


Figure 3-6: Visualisation of intra-aneurysmal iso-velocity surfaces, corresponding to 0.01, 0.015, and 0.1 m/s, under no-stent conditions, and with stent before and after optimisations, for respectively the S, C, and R models. (Black arrows: flow direction; yellow circles: inflow area.)

Figures 3-5 and 3-6 depict the streamlines (colour-coded by velocity magnitude) and iso-velocity surfaces (corresponding to 0.01, 0.015, and 0.1 m/s for respectively the S, C, and R models) for the three aneurysms under the conditions of no-stent, initial stent and optimised stent. Figures 3-7 and 3-8 show the velocity contours generated in the aneurysm neck plane and velocity vectors generated from the aneurysm ostium. Figure 3-9 demonstrates the results of LDT, which presents the differences of AAV with respect to the axial displacements for the initial homogeneous wire and the optimal FD wire structures.

To better present the inflow feature of the aneurysm haemodynamics, the concept of bundle of inflow (BOI) is introduced to describe a flow bundle that enters the aneurysm from its ostium. Likewise, the bundle of outflow (BOO) area indicates the regions where the blood exits an aneurysm. The red and blue arrows/circles in Figures 3-5 and 3-6 refer to the BOIs and BOOs in a corresponding condition; the yellow circles with dotted lines in Figure 3-6 depict the areas where BOI concentrates; and the black arrows indicate the flow directions in each corresponding condition.

Table 3-2: Intra-aneurysmal average velocities and R_f under the no-stent, initial stent, and optimal stent placements for respectively the S, C, and R models (Objective function: AAV).

	No-stent	Initial stent placement		Optimal stent placement	
	$V_{w/o}$ (10^{-3} m/s)	$V_{initial}$ (10^{-3} m/s)	$R_f(\%)$	$V_{optimal}$ (10^{-3} m/s)	$R_f(\%)$
S model	2.827	0.269	90.48	0.123	95.65
C model	10.629	0.528	95.04	0.249	97.65
R model	39.309	13.071	66.75	2.025	94.85

3.3.1.1 S model

Prior to treatment, the blood enters the S model from the distal end and exits through the proximal end. After treatment with a FD stent of the initial homogeneous structure, the intra-aneurysmal flow pattern changes: the streamlines within the aneurysm lumen become irregular and sparse; the BOI area was displaced from the central distal to the proximal end, with a negative radial offset; and a transition of the BOOs from the proximal to the distal end was identified. Flow recirculation inside the aneurysmal lumen was observed after optimisation. In addition, it can be observed that the optimisation resulted in a denser wire configuration within the BOI area (Figure 3-7).

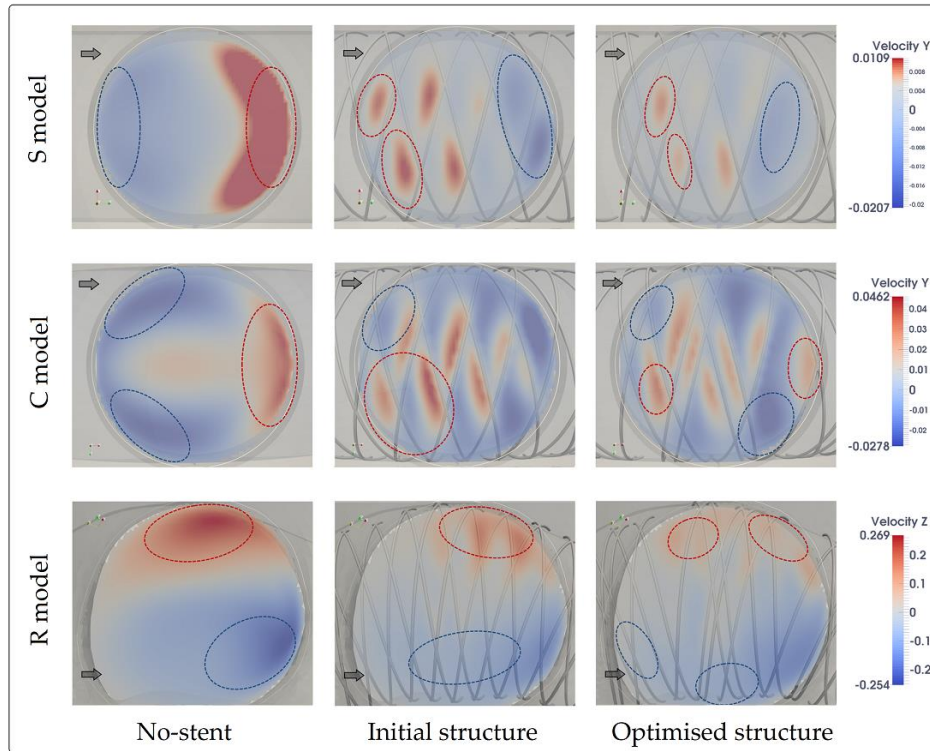


Figure 3-7: Visualisation of velocity components perpendicular to the aneurysm neck plane, under no-stent conditions, and with stent before and after optimisations, for respectively the S, C, and R models. (Black arrows: flow direction, red circles: inflow area, and blue circles: outflow area.)

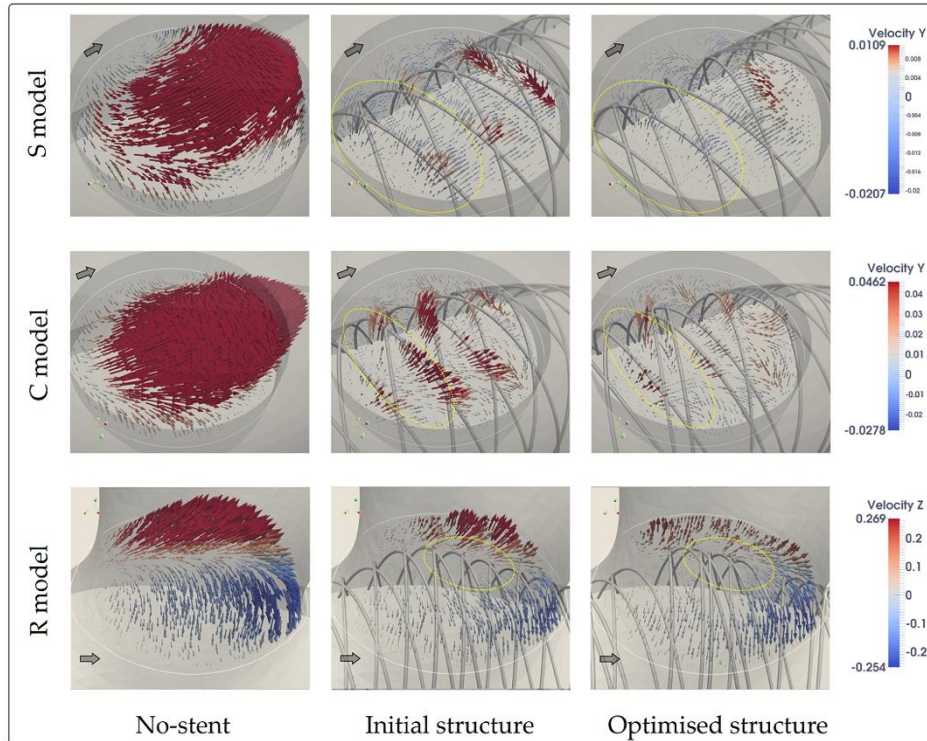


Figure 3-8: Visualisation of velocity vectors generated from the aneurysm neck plane, under no-stent conditions, and with stent before and after optimisations, for respectively the S, C, and R models. (Black arrows: flow direction; yellow circles: inflow area.)

3.3.1.2 C model

Before treatment, a strong BOI and two BOOs were observed respectively in the proximal and the distal ends of the aneurysm neck. The treatment with the initial FD stent considerably reduced the aneurysm inflow, confirmed by a high flow-diversion efficacy of around 90 %. Further reduction of aneurysmal inflow was introduced by the implantation of the optimal FD stent. A recirculation of blood flow within the aneurysm lumen was observed under this condition (Figure 3-5).

3.3.1.3 R model

Compared with the S and C models, the no-stent R model exhibits a strong and sharp impingement of the BOI, right against the wall of the aneurysm. After the treatment with the initial homogeneous FD stent, the magnitude of impingement of the BOI is markedly reduced. Treatment with the FD stent after optimisation further reduced the intra-aneurysmal flow activity, as suggested by the post-treatment iso-velocity surfaces and streamlines. Similar to the S and C models, blood flow recirculation within the aneurysm lumen was found in the C model (Figure 3-5).

3.3.2 Optimisation with the AMV objective function

The optimisation procedure required 913 and 908 SA iterations for respectively the S and C models, until the lower temperature limits (see Table 3-3) were reached. Compared with the initial uniform stent structures, the AMV reduction post treatment with the optimal stent structures were respectively improved by 9.12% and 2.74 %. The AMV and flow reduction rates for the no-stent, initial stent and optimised FD conditions are shown in Table 3-4.

Table 3-3: Initial temperatures and lower temperature limits of SA procedures for the S and C models.

	S model	C model
Initial temperature	2.414×10^{-3}	6.636×10^{-4}
Lower temperature limit	1.244×10^{-5}	3.420×10^{-6}

Figure 3-10 shows the SA developments for the S and C models. The flow reduction rate of the S model increased during the initial 400 iterations, rising from around 84%

at iteration 0 to approximately 92% at iteration 400, before stabilising at 92%. For the C model, the flow reduction fluctuated between 92% and 88% in the initial 200 iterations before the best flow reduction rate of 95.49% was finally achieved. The improvement of flow reduction shows a similar trend in the two models, which drastically increases in the initial hundreds of iterations and then stabilises at a certain level. No further improvement of flow-diversion efficacy was obtained during the final 100 iterations for either case.

Table 3-4: The AMVs and R_f under the no-stent, initial stent and optimised FD conditions of respectively the S and C models. (Objective function: AMV)

	Non-stent $V_{w/o}$ ($10^{-3}m/s$)	Initial stent placement $V_{initial}$ ($10^{-3}m/s$)	$R_f(\%)$	Optimal stent placement $V_{optimal}$ ($10^{-3}m/s$)	$R_f(\%)$
S model	36	6.13	83.63	2.61	92.77
C model	145	10.56	92.75	6.57	95.49

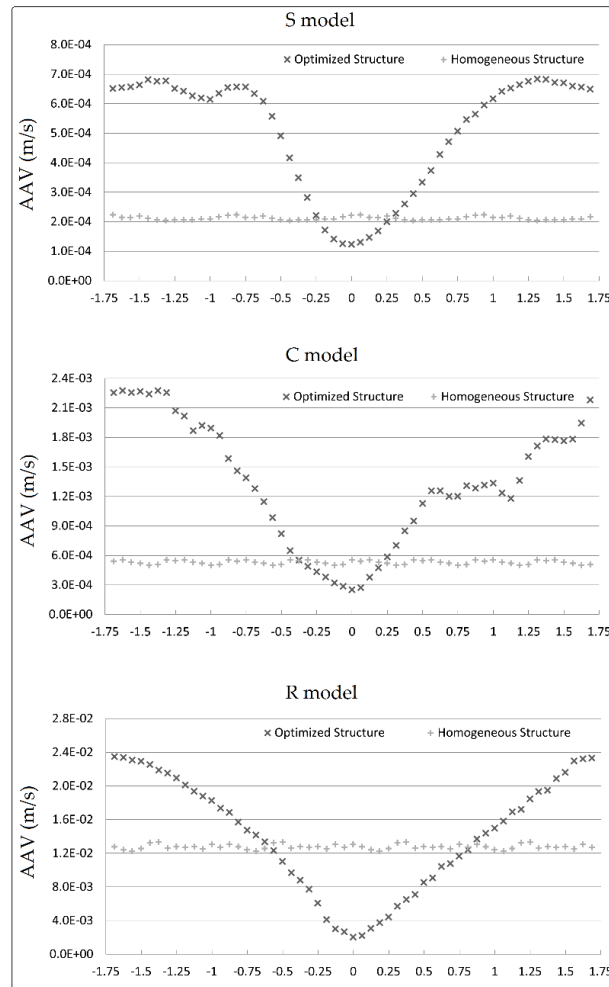


Figure 3-9: LDTs of the optimised FD stent structures for respectively the S, C, and R models (Horizontal axis: the longitudinal displacement of the respective FD stent structure).

Figures 3-11, 3-12, and 3-13 show the FD structures and the haemodynamic differences between treatments with the initial and the optimised FD stent structures. As observed in both cases, optimisation changed the structures of the FD stent wires: the homogeneous wire structures were disrupted and larger areas without metal coverage could be observed in the optimised FD structures. Compared to the initial FD stent intervention, the magnitude of velocity components perpendicular to the aneurysmal ostium markedly decreased after treatment with the optimised FD stent, particularly in the inflow area. The streamlines (colour-coded by velocity magnitude) demonstrate that the high-velocity magnitude inflow area located at the aneurysmal ostium was reduced.

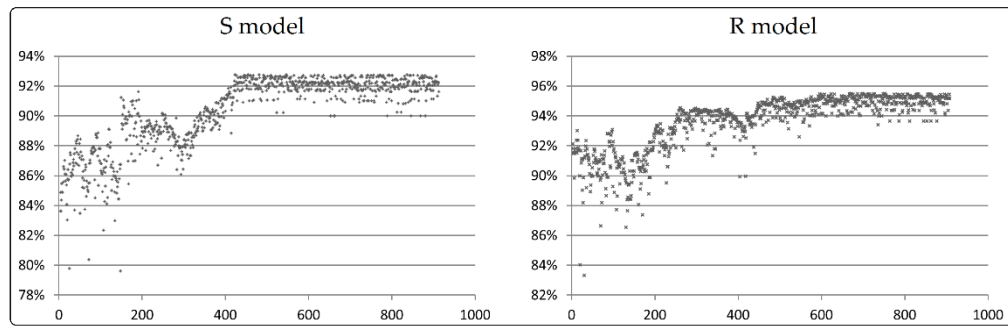


Figure 3-10: The SA developments for the S and C models. (Vertical axis: R_f , horizontal axis: steps of SA procedure.) Objective function: AMV.

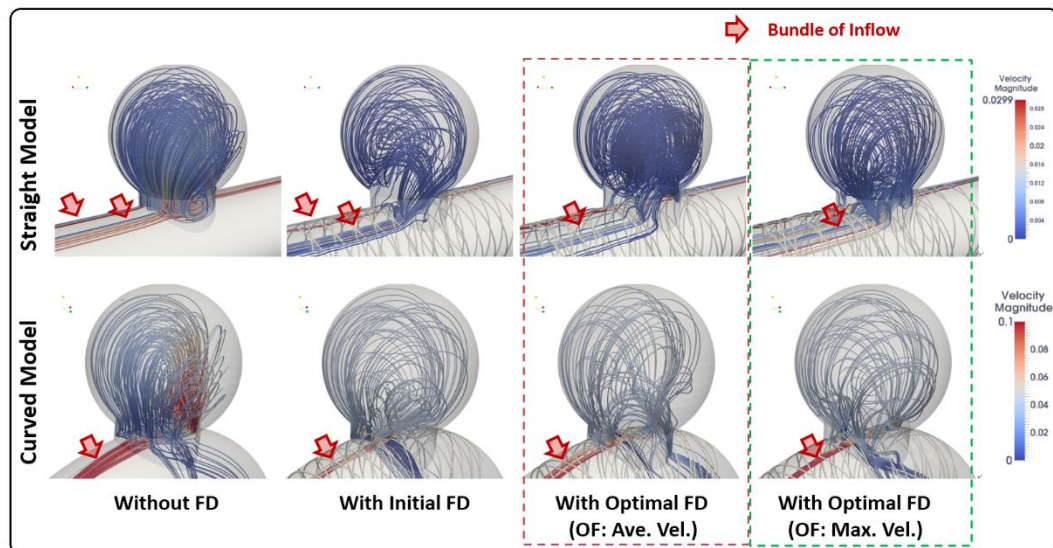


Figure 3-11: Visualisation of intra-aneurysmal streamlines, colour-coded by velocity magnitude, before and after optimisations, for respectively the S and C aneurysm models. (Red arrows: BOI, rectangle with red dotted lines: results obtained from adopting AAV as objective function, and rectangle with green dotted lines: results obtained from adopting AMV as objective function.)

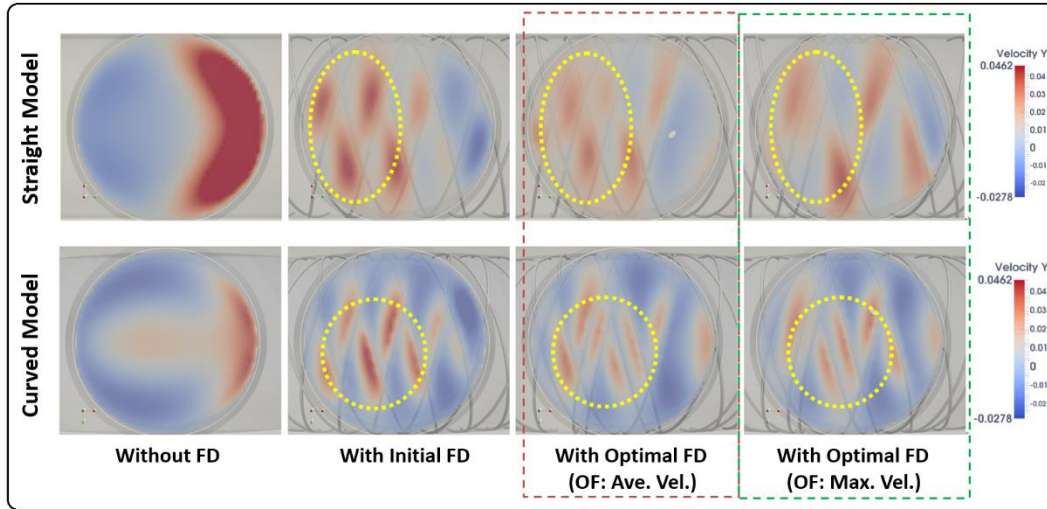


Figure 3-12: Visualisation of velocity components perpendicular to the aneurysm neck plane before and after optimisations, for respectively the S and C aneurysm models. (Yellow circles: inflow area, rectangle with red dotted lines: results obtained from adopting AAV as objective function, and rectangle with green dotted lines: results obtained from adopting AMV as objective function.)

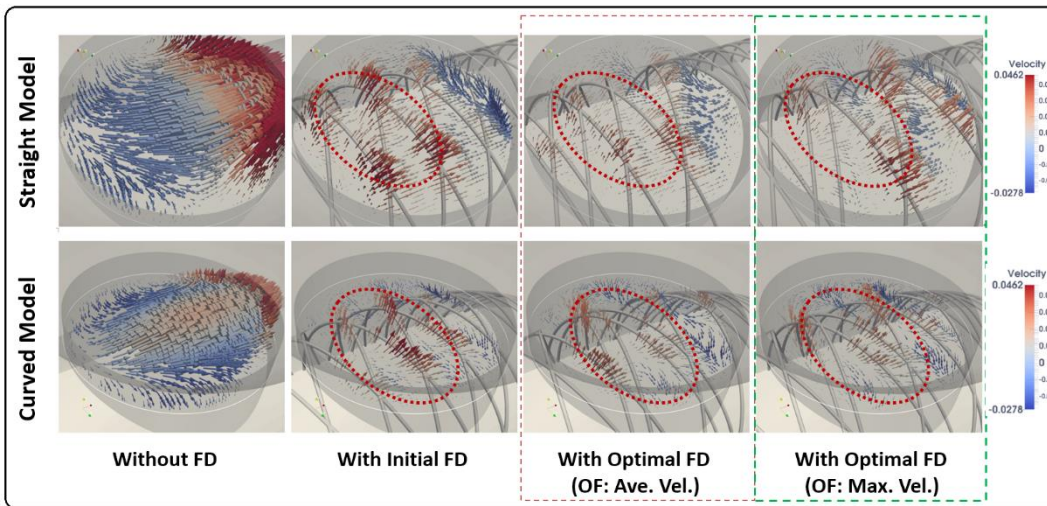


Figure 3-13: Visualisation of velocity vectors generated from the aneurysm neck plane before and after optimisations, for respectively the S and C aneurysm models. (Red circles: inflow area, rectangle with red dot lines: results obtained from adopting AAV as objective function, and rectangle with green dotted lines: results obtained from adopting AMV as objective function.)

Figure 3-14 demonstrates the alteration of AAV with respect to AMV during the optimisation process: a flow reduction improvement of AMV does not accompany that of AAV. For the S model, the highest flow reduction rate obtained was 92.77%, whereas the reduction rate of AAV was only around 93% at this point (refer to point A in Figure 3-14). The highest reduction rate of AMV was observed as point B (just over 94%), whereas the flow reduction of AAV was only approximately 87%. For the C model,

optimal solutions are observed to concentrate in region C (Figure 3-14); nonetheless, the maximum reductions of AAV (point D) and AMV (point E) are not at the same point.

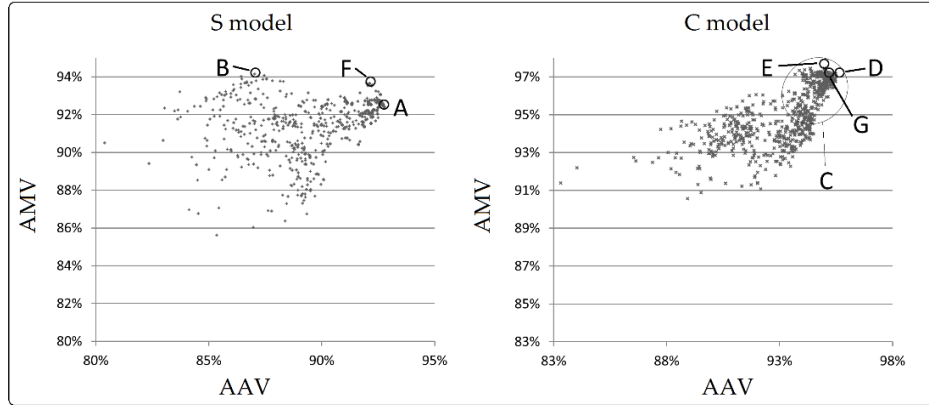


Figure 3-14: Visualisation of reduction rates of AMV and AAV of the S and C models. Objective function for optimisation: AMV.

3.4 Discussion

In this Chapter, a numerical approach applied to the optimal design of FD stents was shown. To improve the flow-diversion efficacy of the conventional FD stents with homogeneous wire configuration, this approach rearranged the starting phases of stent wires, so as to maximally block the aneurysmal inflow jets. With this optimisation approach, the flow-diversion efficacy can be markedly improved, while the overall porosity of the FD stent can be maintained.

3.4.1 Modification parameter used in optimisation

The stent wire starting phase was chosen as the modification parameter, owing to consideration of the correlation between FD stent porosity and post-treatment in-stent stenosis.

In fact, various other parameters that define a FD stent design were chosen in previous optimisation studies. Anzai *et al.* [68,70] modified the strut segment configurations within the aneurysm ostium, and found that the flow-diversion efficacy can be improved, whilst the stent porosity was maintained strictly at 80%. However, the isolated and disconnected strut segments denied the possibility of fabricating the

optimal stent structure. Lee *et al.* [85] adopted gap spacing and strut size as the modification parameters. Optimal FD stent designs were obtained in this study; however, the low device porosity post-optimisation becomes a problem. The starting phase is one of the parameters required in the design and manufacturing process of FD stents. The simulation demonstrates that the modification of wire starting phase could markedly improve the flow-diversion efficacy of a conventional homogeneous FD stent, without changing the stent's porosity.

3.4.2 Objective function and SA procedure

Optimisation outcomes vary with respect to the objective functions. A proper determination of objective function is of great importance for optimisation to make favourable FD stent designs. FD stent structural optimisation is driven by the pursuit of an improved treatment prognosis, but no consensus on critical parameter(s) that can clearly determine the prognosis has yet been reached. I chose AAV or AMV as the objective function because they were reported to be related to a shorter period of thrombotic occlusion of the aneurysm. In addition to average velocity, the optimisation approach accepts other objective functions that may predict a favourable prognosis.

In addition to AAV and AMV, many other parameters have been proposed in relation to a short period of aneurysm occlusion. Corbett *et al.* [122] performed an *in vitro* study, and reported that thrombosis could occur when shear stress or shear rate of bovine blood reaches a specific threshold. A review by Moiseyev *et al.* [58] concludes that the shear-induced activation of platelets is a requisite for blood coagulation. In contrast, Janiga *et al.* [74] reported that wall shear stress can be an important factor related to the occlusion of an aneurysm. Recently, Chung *et al.* [56] reported that the average velocity within the aneurysm lumen is related to a shorter period of complete aneurysm occlusion. As revealed by these studies, AAV and AMV might be correlated with thrombotic occlusion; however, further study is still needed before its clinical relevance can be confirmed.

Theoretically, SA procedure is able to identify a global optimum, provided that the initial temperature and cooling schedule are well determined. As shown in Figure 3-4,

to prevent optimisation from resulting in a local optimum, modifications of FD structure that have inferior flow-diversion efficacy might also be accepted according to the pre-defined cooling schedule.

The AAV was measured during optimisation of the S and C models with AMV set as the objective function. As observed in Figure 3-14, an enhanced AMV reduction does not always accompany the increment of AAV reduction. Thus, to achieve a condition with both lower AMV and AAV, the FD structures in the vicinity of point F and G in Figure 3-14 may be considered as the overall optimal solutions for respectively the S and C models. Alternatively, optimisation using multiple objective functions may be applied, when computational cost is no longer a concern.

3.4.4 Haemodynamic compatibility between FD structure and vascular geometry

Haemodynamic compatibility of an FD device refers to the suitability of its wire structural design, from which the local aneurysmal haemodynamics of the FD recipient could attain a desired modification. Superior haemodynamic compatibility leads to favourable blood flow modifications that finally contribute to a shorter period of thrombotic occlusion and a lower risk of post-stenting complications.

Currently, manufacturers provide many choices of FD products with different combinations of length and diameter, but the wire configurations of these FD stents remain homogeneous. Previous studies suggested that the efficacy of a homogeneous FD is primarily determined by its porosity. However, results shown in this paper, together with a study of asymmetric stent design, indicate that the efficacy of an FD depends not only upon its porosity but also upon its specific structural design. IAs have specific regions (BOI regions) in which strut placement can efficiently reduce aneurysmal inflow, whereas struts positioned outside the region show less effect. The optimisation, as a practical approach for the conventional homogeneous FD devices, shows that compacting FD stent wires into BOI areas may achieve a marked difference in blocking the aneurysmal inflow.

3.4.5 Reliability of the optimised FD structure

The reliability of the optimised FD wire structure was examined by a set of LDTs. In the LDTs, I found that greater flow reduction rates were produced by the optimised wire structures within displacement ranges of -0.25 to 0.25 (S model), -0.5 to 0.25 (C model), and -0.75 to 0.75 mm (R model), compared to those of the initial homogeneous structures (see Figure 3-9). This indicates that although FD stents with uniform wire configuration can non-specifically prevent a strong inflow jet from passing through an aneurysm ostium, the flow-diversion efficacy of stents with uniform wire configuration is inferior to that of the optimised wire configuration when a device was desirably deployed.

The reliability of an optimised FD is associated with the metal coverage mode within the aneurysm ostium. The optimised FD wires concentrate in BOI areas where aneurysmal inflow passes through, whereas only a small number of wires are assigned in the remaining areas where large holes can be found. This phenomenon explained why the optimised configuration has superior flow-diversion efficacy. However, if axial displacement occurs, the inflow jet has a chance to cross the orifice through the large holes, causing considerable fluctuations. It is our future task to improve the stability of an optimized FD by including a robustness test in the optimisation loop.

3.4.6 Disruption of BOIs determines flow-diversion efficacy

First introduced by Anzai *et al.* [70], disrupting the BOIs of an aneurysm is crucial to an effective blockage of aneurysm inflow. BOI refers to the inflow bundle of an aneurysm and can be visualised as the concentrated streamlines that enter an aneurysm. Regardless of objective functions applied (*e.g.* the AMV and AAV were respectively used), the same trend of wire strut rearrangements was observed: that stent wires were reallocated to better cover the BOI areas. This confirms the importance of BOI disruption, in order to obtain a higher flow-diversion efficacy.

3.5 Limitation and Future Work

Several limitations exist in this study. At first, the blood was assumed to be a Newtonian fluid in a rigid system. Since the objective of this study is to work out a feasible optimisation approach for FD stent structures, the computational cost was a serious issue especially when SA was adopted as the optimisation algorithm. When the computational cost is no longer a problem, the simulation settings are readily changed by adopting a time-dependent boundary condition and a non-Newtonian rheology in the LB solver.

The second limitation from the viewpoint of clinical practice is that deploying the optimised FD stent to the desired location would be a challenge for interventionists. This might be addressed in the future version of the optimisation approach by embedding a reliability test into the SA loop.

Another limitation is that I studied merely the haemodynamic improvements that an optimised FD stent would be able to provide; the mechanical and material properties of the optimised FD stents have not been investigated. It is for future work to have the optimised FD designs fabricated and tested *in vitro/vivo*.

3.6 Conclusion

In this Chapter, a practical optimisation approach for FD stents with initially homogeneous wire configurations was demonstrated. This optimisation approach is able to improve the flow-diversion efficacy of the conventional FD stents, by rearranging the starting phases of the helical metal filaments.

The proposed method was applied to the structural optimisations of three FD stents, with each corresponding to one aneurysm geometry. Without altering the pre-assigned overall stent porosity of 80 %, optimisation respectively improved the flow-diversion efficacies by 5, 2, and 28 % for the S, C, and R aneurysm model. Observing aneurysmal flow patterns post-optimisation, I confirmed that a disruption of the bundle of inflow is of great importance for reducing the intra-aneurysmal average

velocity. Furthermore, the reliability of the optimised stent structures was tested, and I found that the structure for the R model exhibits the best performance in tolerating the longitudinal displacements incurred during stent deployment.

The method developed can be used to identify the wire structure with the best flow-diversion efficacy for a given patient aneurysm geometry. By rearranging the helix wires' starting phases, a homogeneous FD stent can be tailored to an inhomogeneous one with maximal flow-diversion efficacy for a patient aneurysm. In addition, the developed approach does not alter a pre-assigned stent porosity after optimisation, which potentially protects patients against post-stenting in-stent stenosis.

Chapter 4

Haemodynamic Simulation of Flow-Diversion Treatments with Stent Compaction Applied

4.1 Objective

Apart from the effort made to improve flow diversion by individualising the FD stent structure, clinicians also endeavour to better block the aneurysmal inflow by special manipulations performed in the process of stent deployment. Compacting an FD stent is an emerging technique to create a denser wire configuration across the aneurysm ostium. However, quantitative post-treatment haemodynamics affected by the compaction level of different stent diameters have not been completely understood.

Literature review suggests that a few studies have focused on this stent compaction technique. Makoyeva *et al.* [95] studied the stent compaction effects on wire configurations across the aneurysm ostium *in vitro*. Gentric *et al.* [88] confirmed in animal experiments that stent compaction can improve angiographic occlusion of wide-neck aneurysms. An optimisation study by Janiga *et al.* [72] found that stent compaction within a certain segment across the aneurysm ostium led to a further reduction of aneurysmal inflow. Applying the finite-element method, a recent study by Xiang *et al.* [80] simulated FD stent deployment under a maximum-compacted condition. In this condition, haemodynamic modifications were reported to be twice as effective as those achieved in the non-compacted condition.

In interventional practice, pursuing a maximum compaction is not the safest approach, as over-compacting a stent may result in a stent prolapsing into the aneurysm lumen or migrating, causing treatment failure [88]. In addition, the haemodynamic effects of stent size cannot be neglected [87]. Therefore, it is of great importance to quantify the haemodynamic effects of stent diameter, along with compaction level, thereby assisting neuroradiologists with information that contributes to a favourable treatment plan.

In this Chapter, I propose to quantify the flow-diversion efficacies following treatments with FD stents of different diameters under compaction at different levels. To meet this need, I virtually deployed FD stents of three diameters, with each diameter modelled at four compaction levels, into two clinically observed aneurysms — one successful case, the other unsuccessfully treated with a *Silk+* FD stent — to

contrast the haemodynamic alterations after treatments of a total of 24 stenting scenarios.

4.2 Methods

4.2.1 Aneurysm and FD stent model

The successful and unsuccessful aneurysm models introduced in Section 2-1 were employed in this study after institutional ethical approval was obtained. The successful case was clinically categorised as a ‘successful’ one, because complete aneurysm occlusion was confirmed by CTA scan taken upon the follow-up 6 months after treatment, whereas CTA scan confirmed that the unsuccessful aneurysm remained patent 6 months after treatment (refer to Chapter 2-1 for a detailed description).

4.2.2 FD stent modelling and deployment

Given the large variation of diameter in the parent artery, FD stent treatment using a range of device diameters — 4, 4.5, and 5 mm — was investigated for each aneurysm, to survey the possible haemodynamic differences affected by the treating clinicians’ experience. This is because any of these diameters could plausibly be selected based upon the clinicians’ judgements and because stents with the diameters of 4.0 and 4.5 mm were respectively used in the real treatment of the two patients. Refer to Section 2-3-2 for the methodologies used to model the FD stents and Section 2-3-3 for the process used to simulate the deployment process.

4.2.3 Stent compaction ratio

In this study, an FD model was constructed based upon the structure of the *Silk+* stent following an FD description previously reported by Lieber and Sadasivan [34]. For an

FD device with a nominal diameter D and length L , the metal coverage rate (MCR) at the nominal condition can be estimated by

$$\text{MCR (\%)} = \frac{nd\sqrt{p^2 + \pi^2 D^2}}{\pi p D} \times 100, \quad (4 - 1)$$

where n is the number of wires that comprise an FD stent; d is wire thickness; and p is the pitch of a helical wire, which can be measured from the stent model geometry. An FD stent has a theoretical limiting condition of maximum compaction in which the MCR equals 100%, that is, no space exists between any two neighbour wires. The pitch at maximum compaction can therefore be derived, which corresponds to the minimum pitch, p_{\min} , by letting $\text{MCR} = 100\%$. Under this condition, a fully compacted wire configuration across the aneurysm ostium can be produced by axially pushing the FD a length of

$$\Delta L_{\max} = \left(\frac{p_1}{p_{\min}} - 1 \right) \cdot L_{\text{neck}} \quad (4 - 2)$$

into the aneurysm neck segment, where L_{neck} denotes the longitudinal length of the aneurysm neck segment, and p_1 is the pitch in the neutrally expanded condition, prior to compaction. In interventional practice, complete compaction of an FD device is unrealistic, as aggressively compacting an FD can result in pushing its wires into the aneurysm lumen — a serious concern related to aneurysm rupture. Therefore, I investigated the effects of four levels of compaction ratio — *i.e.* 0% (I), 25% (II), 50% (III), and 75% (IV) — acting on each choice of stent diameter within the aneurysm neck segment. The compaction ratio is computed as

$$\text{CPT} = \frac{\Delta L}{\Delta L_{\max}} \quad (4 - 3)$$

Based on the values of CPT determined corresponding to the four levels of compaction ratio, the MCRs were calculated and set in the program simulating the process of stent deployment.

4.2.4 Haemodynamic simulation

The mesh dependence for the two geometries was studied in the previous work [31,104]. In this study, ICEM-CFD (ANSYS, Canonsburg, USA) was used to generate a tetrahedral mesh with maximum sizes of respectively 0.5, 0.1, and 0.01 mm for volume, aneurysm surface, and FD surface. The number of mesh ranged from 8 to 15 million in total, across different cases, and the mesh elements falling between any two wires (with an average of around 20 elements) were considered to be sufficient to characterise the flow behaviours in between the wires. The vascular wall and FD surface were assumed to be rigid and a no-slip condition was then imposed at these boundaries.

Since neither a time-varying inflow velocity nor an outlet pressure profile was available to us for these patients, steady flow simulations were performed for each scenario under a range of inflow conditions (130, 190, 250, 310, and 370 mL/min at the ICA inlet) that covers the possible diastole-to-systole range of inflow in normal patients. A fixed 0 Pa static pressure boundary was applied to all outlets of each geometry. The numerical results were obtained by solving the Navier–Stokes equations for 3D steady laminar flow using the CFX computational fluid dynamics (CFD) solver in the ANSYS 15.0 package (ANSYS, USA). With acceptable justifications [39], as in other CFD simulations performed in blood vessels, the blood was assumed to be an incompressible Newtonian fluid, with density and viscosity fixed to 1050 kg/m³ and 0.0035 Pa·s, respectively. The convergence criteria for the normalised continuity and velocity residuals were both chosen as 10⁻⁵; with these settings, an average computational time of 5 hours was taken for each scenario using 16 cores on a Z840 workstation (Hewlett-Packard, USA).

Streamlines, iso-velocity surfaces, and wall shear stress (WSS) were examined for each scenario, and the consequent modifications of MCR, aneurysmal average velocity (AAV), mass flowrate (MF), and energy loss (EL) were investigated. EL is believed to be one of the factors in the development and final rupture of aneurysms [36]. It refers to the energy difference between the aneurysmal inflow and outflow:

$$EL = \sum_{i=1}^{n_{in}} Q_{in,i} \left(\frac{p_{in,i}}{\rho} + \frac{1}{2} u_{in,i}^2 \right) - \sum_{j=1}^{n_{out}} Q_{out,j} \left(\frac{p_{out,j}}{\rho} + \frac{1}{2} u_{out,j}^2 \right), \quad (4-4)$$

where Q denotes MF; p is static pressure; ρ is fluid density; u is inflow or outflow velocity, as denoted by the subscripts; and i and j are indices referring to locations in the measurement domain.

4.3 Results

4.3.1 FD wire structures and MCR after compaction

Figures 4-1 and 4-2 show the virtual deployment processes for the successful and the unsuccessful cases. Figures 4-3 and 4-4 depict the deployed FD structures at four compaction levels for the successful and the unsuccessful cases. Figure 4-5 shows the corresponding MCR values measured across the aneurysmal ostium.

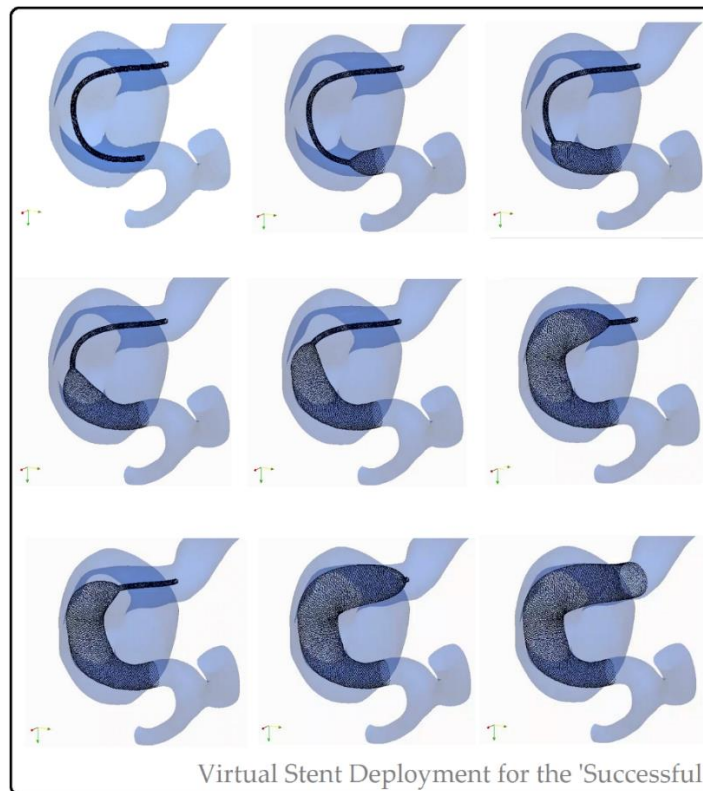


Figure 4-1: FD stent deployment process of the successful aneurysm case. (From top-left to bottom-right: stent vertices fully crimped to fully expanded)

In the non-compacted condition, the average MCRs across the aneurysmal ostium were measured to be 29% (successful case) and 26% (unsuccessful case). When stents were compacted at level IV, MCRs were raised to 62% (successful case) and 51%

(unsuccessful case). For scenarios at the same compaction level, the MCR measured in the successful case was higher than that measured in the unsuccessful one. Interestingly, with the increase of compaction ratio, the MCR gap between the successful and the unsuccessful cases was widened further. Selection of different device diameters showed less effect on MCR, with maximum differences less than 5% for both the successful and unsuccessful cases.

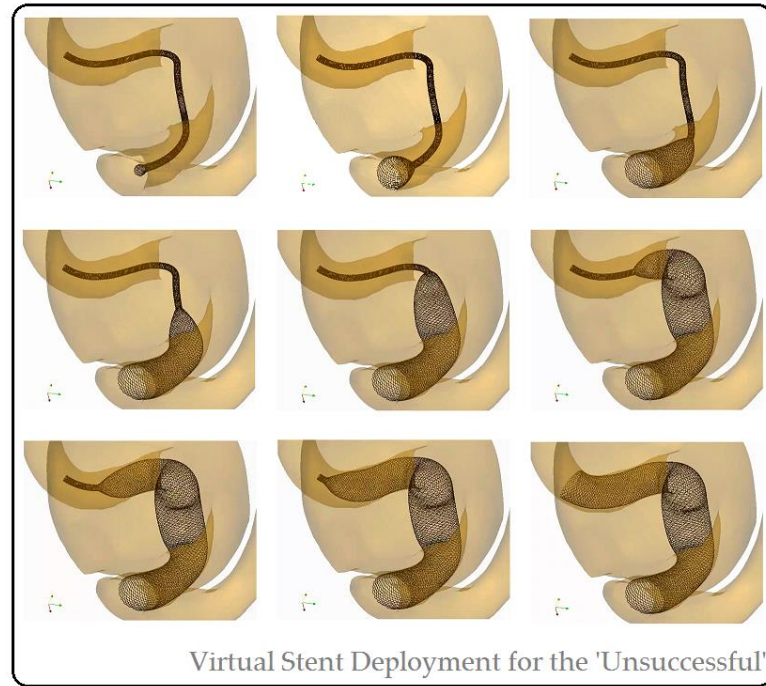


Figure 4-2: FD stent deployment process of the unsuccessful aneurysm case. (From top-left to bottom-right: stent vertices fully crimped to fully expanded)

Table 4-1: The average improvements of flow reduction with each level's (25%) advancement of compaction ratio, compared to the no-stent conditions. Values are the average for the five inflow boundary conditions.

	Haemodynamic Parameters	Stent Diameter			Ave. Imp.
		4.0 mm	4.5 mm	5.0 mm	
Successful case	AAV	14%	15%	13%	14%
	MFR	12%	12%	11%	12%
	EL	10%	9%	8%	9%
Unsuccessful case	AAV	6%	9%	11%	9%
	MFR	6%	10%	10%	9%
	EL	7%	11%	10%	9%

AAV: aneurysmal average velocity, MFR: mass flow rate, EL: energy loss, and Ave. Imp: the average of a given haemodynamic parameter for different diameters.

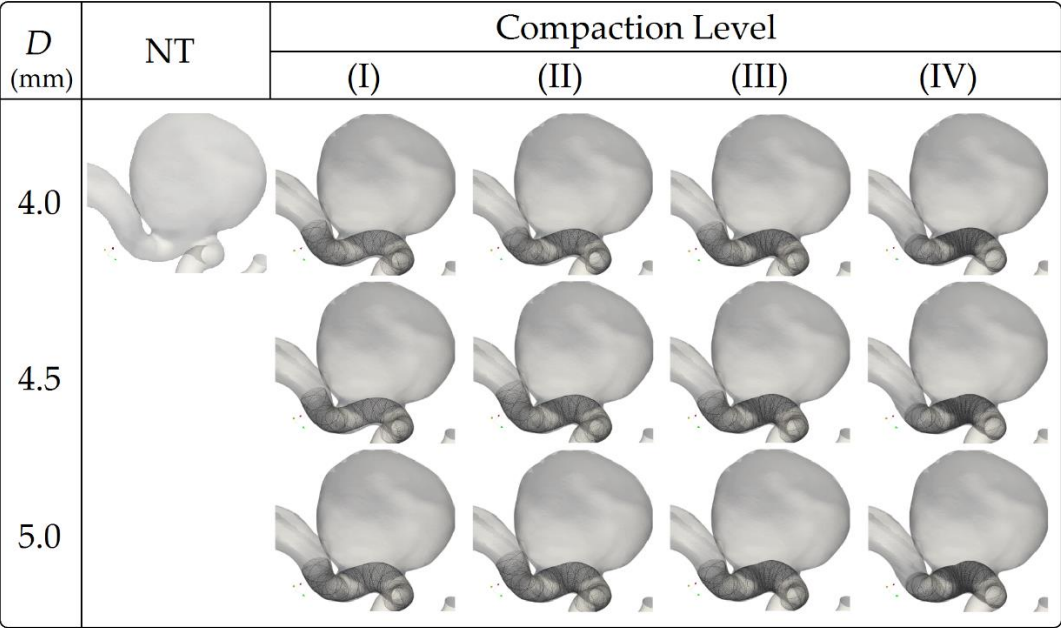


Figure 4-3: FD stent configurations of treatments with FD stents of three different diameters, D , at four compaction levels in the unsuccessful case. The untreated case is also shown for comparison. (NT: untreated condition; CPT: compaction level.)

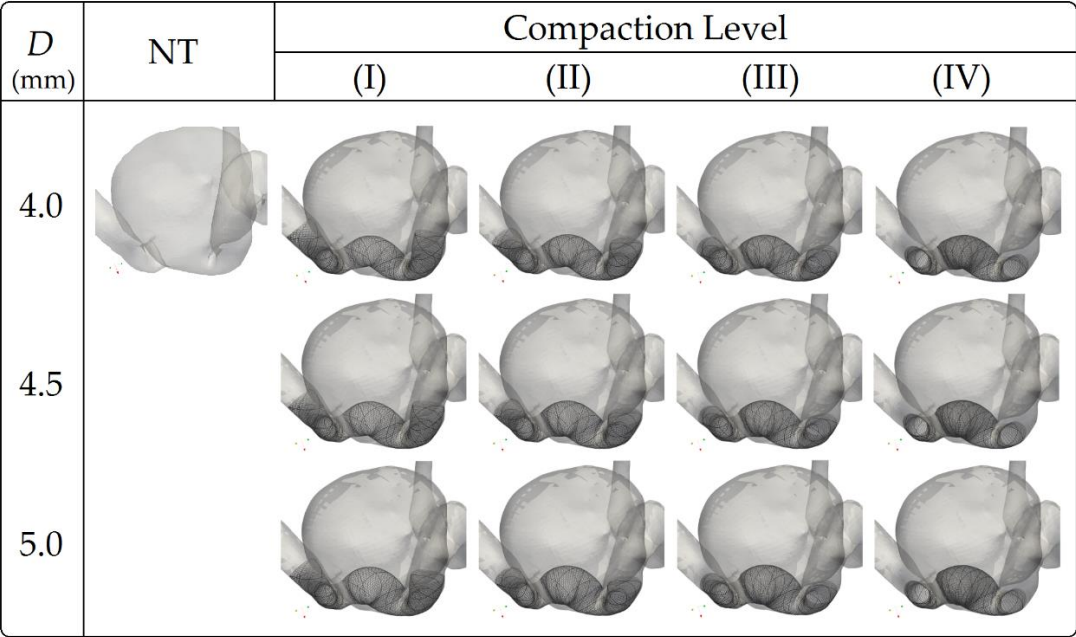


Figure 4-4: FD stent configurations of treatments with FD stents of three different diameters, D , at four compaction levels in the unsuccessful case. The untreated case is also shown for comparison. (NT: untreated condition; CPT: compaction level.)

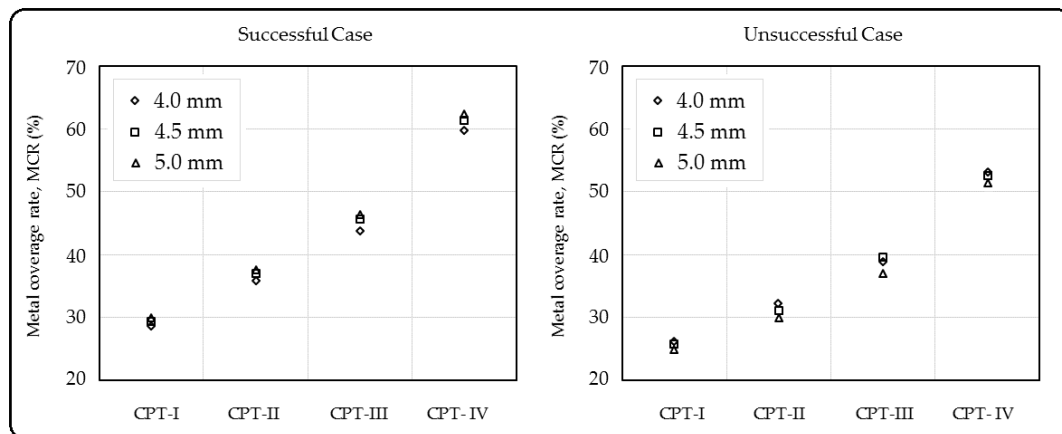


Figure 4-5: Metal coverage rates measured across the aneurysm ostium for the successful (left) and the unsuccessful (right) cases.

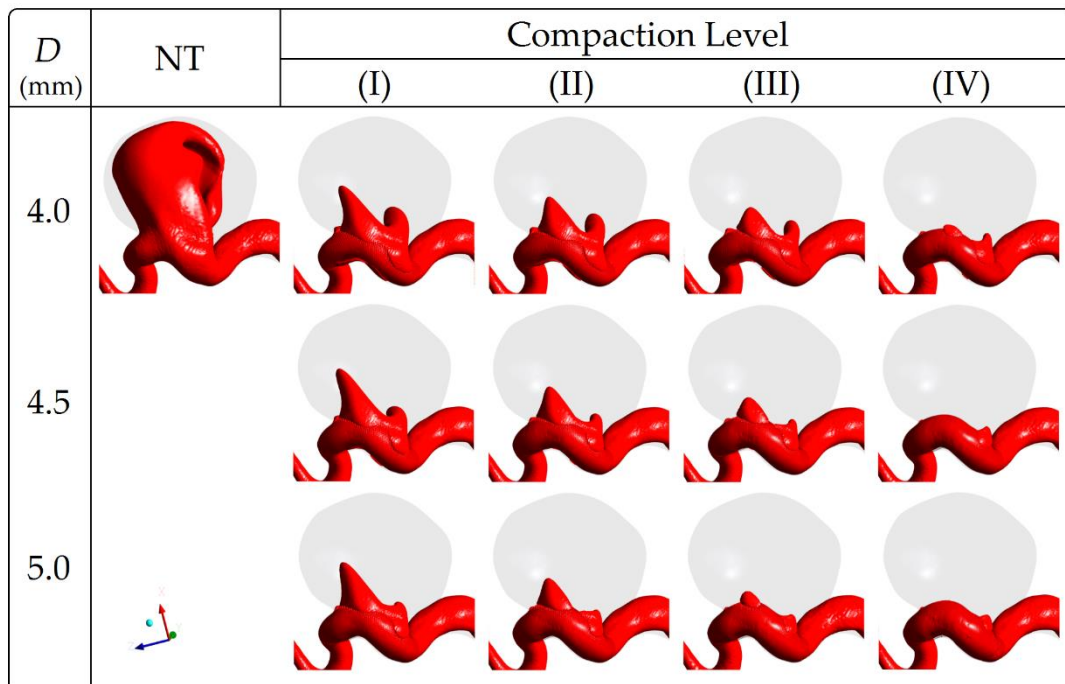


Figure 4-6: Iso-velocity visualisation of treatments with FD stents of three different diameters, D , at four compaction levels in the successful case. Inflow boundary condition = 130 mL/min. The untreated case is also shown for comparison. (NT: untreated condition; CPT: compaction level.)

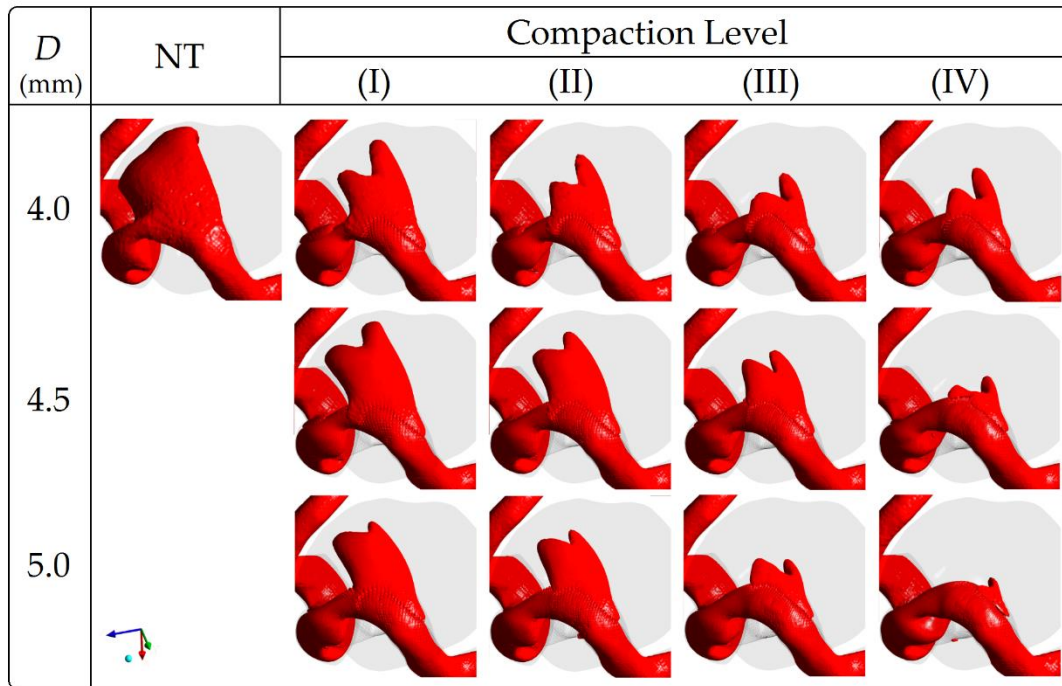


Figure 4-7: Iso-velocity visualisation of treatments with FD stents of three different diameters, D , at four compaction levels in the unsuccessful case. Inflow boundary condition = 130 mL/min. The untreated case is also shown for comparison. (NT: untreated condition; CPT: compaction level.)

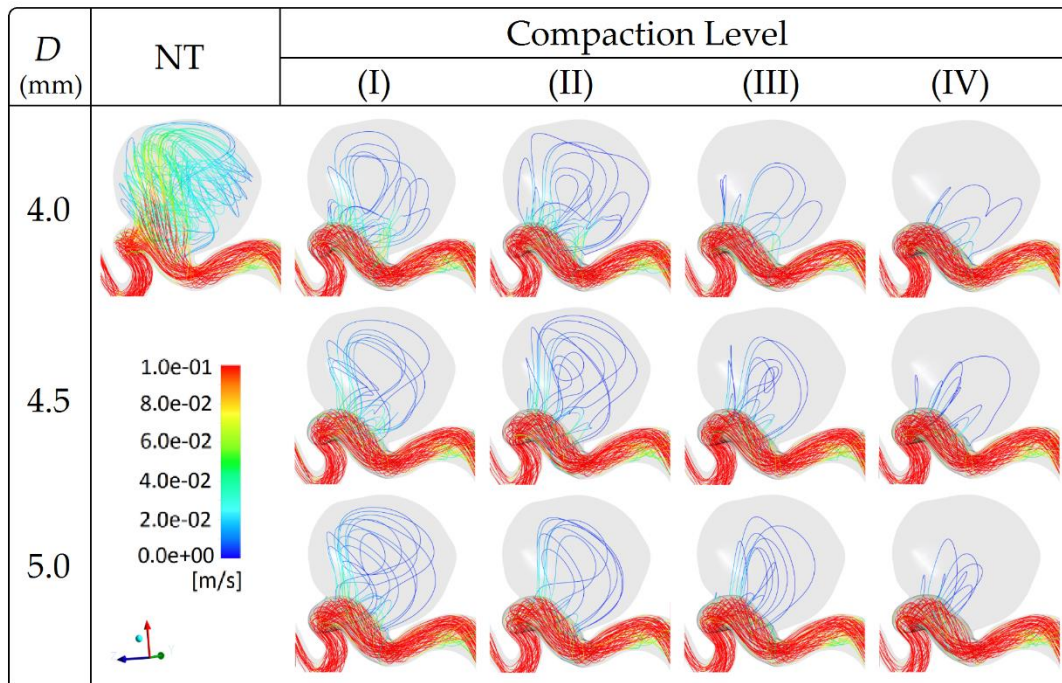


Figure 4-8: Streamline visualisation for treatments with FD stents of three different diameters, D , at four compaction levels in the successful case. Inflow boundary condition = 130 mL/min. The untreated case is also shown for comparison. (NT: untreated condition; CPT: compaction level.)

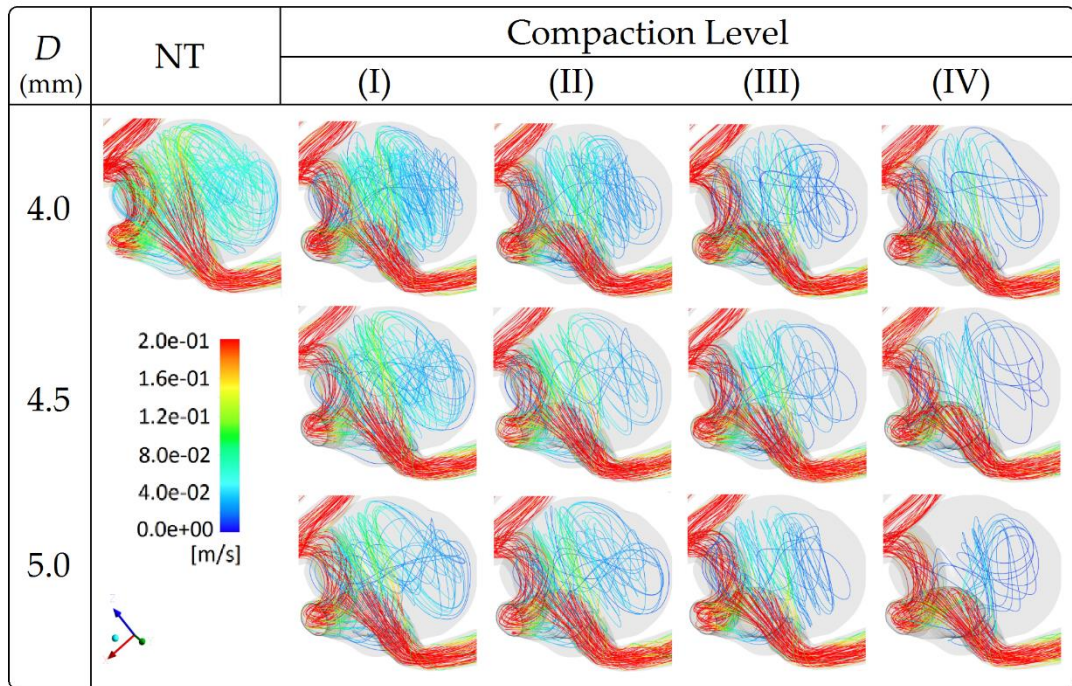


Figure 4-9: Streamline visualisation for treatments with FD stents of three different diameters, D , at four compaction levels in the unsuccessful case. Inflow boundary condition = 130 mL/min. The untreated case is also shown for comparison. (NT: untreated condition; CPT: compaction level.)

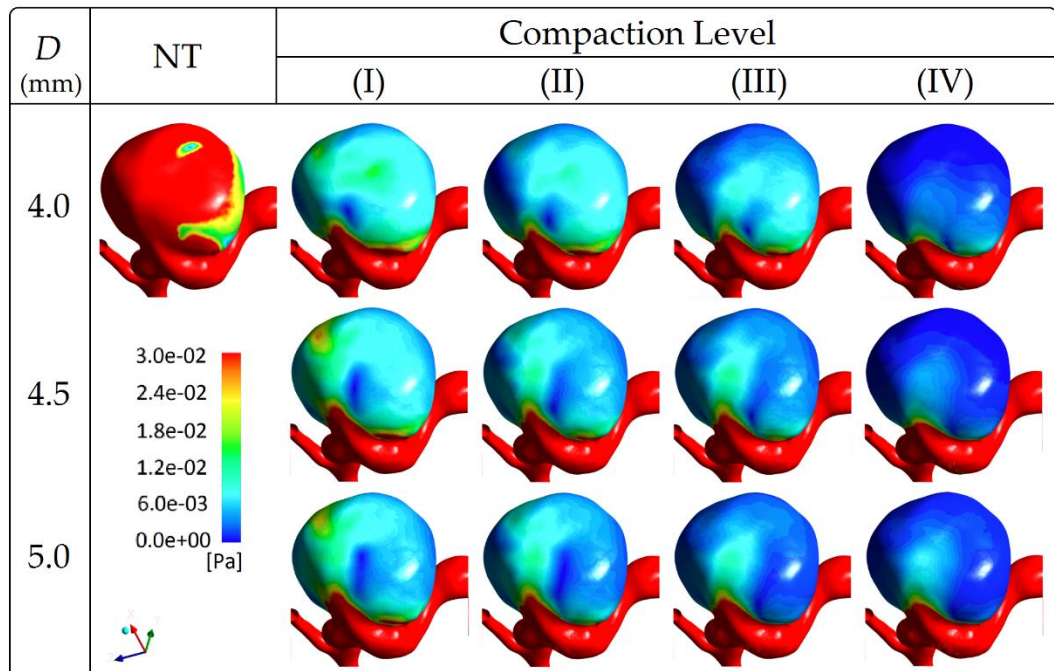


Figure 4-10: WSS visualisation of treatments with FD stents of three different diameters, D , at four compaction levels in the successful case. Inflow boundary condition = 130 mL/min. The untreated case is also shown for comparison. (NT: untreated condition; CPT: compaction level.)

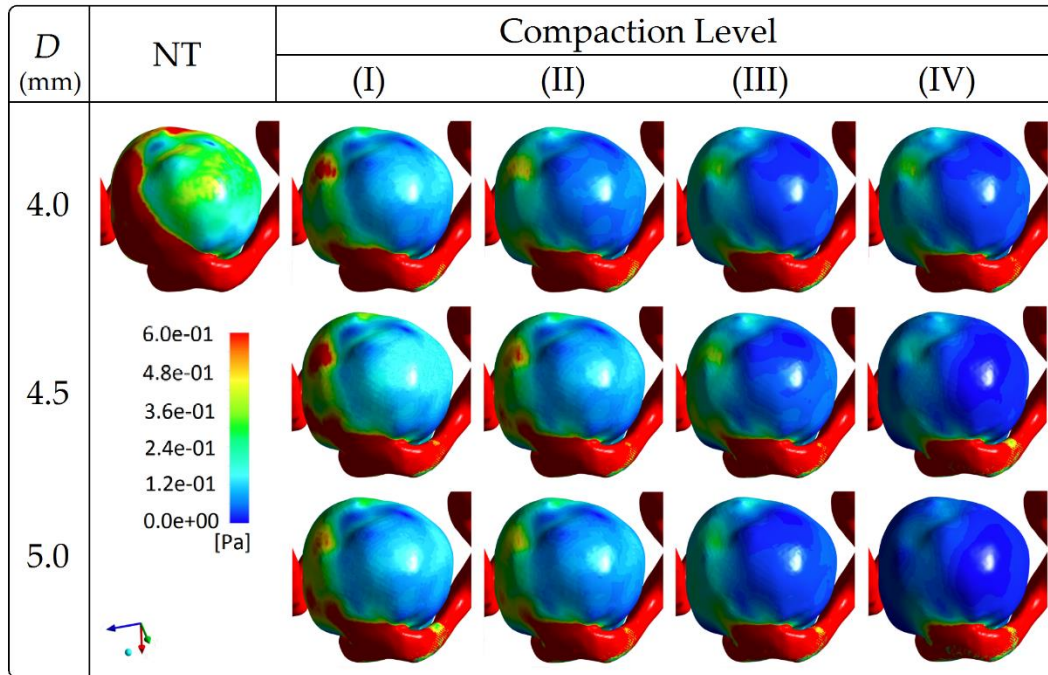


Figure 4-11: WSS visualisation of treatments with FD stents of three different diameters, D , at four compaction levels in the unsuccessful case. Inflow boundary condition = 130 mL/min. The untreated case is also shown for comparison. (NT: untreated condition; CPT: compaction level.)

Table 4-2: The difference between the maximum and the minimum value of each haemodynamic parameter at a given compaction level, considering five inflow conditions and three diameters. Values are the proportional differences compared to the no-stent conditions.

	Haemodynamic Parameters	Stent Compaction Level				Ave. Diff.
		I	II	III	IV	
Successful case	AAV	2%	9%	19%	5%	10%
	MF	2%	5%	11%	4%	6%
	EL	8%	10%	13%	1%	8%
Unsuccessful case	AAV	8%	7%	8%	15%	10%
	MF	7%	7%	8%	13%	9%
	EL	10%	9%	8%	10%	9%

AAV: aneurysmal average velocity, MF: mass flow rate, EL: energy loss, and Ave. Diff: the averaged difference of a given haemodynamic parameter across different stent compaction levels.

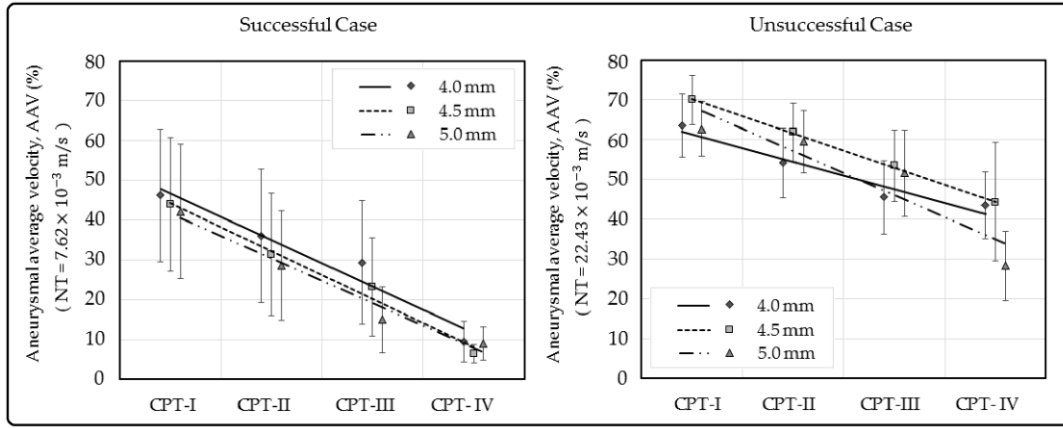


Figure 4-12: Relative values of AAV after treatments with a FD stent for three different diameters and four compaction levels. Symbols are plotted at the average for the five inflow boundary conditions; vertical error bars indicate the standard deviation for each such condition. The untreated condition (NT) represents the 100% level in each graph.

Unlike the successful case, in which an approximately tubular stent-mesh surface covers the aneurysm ostium, in the unsuccessful case, the stent mesh dilated into the aneurysm lumen. This phenomenon is associated with the distinctions of parental artery morphology: the successful case has a less-curved centreline, whereas the unsuccessful case has a highly-curved one.

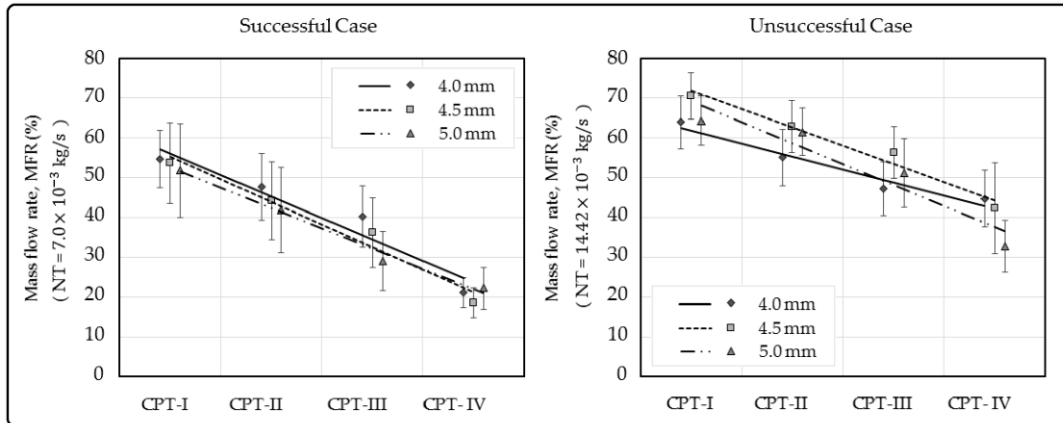


Figure 4-13: Relative values of MF after treatments with a FD stent for three different diameters and four compaction levels. Symbols are plotted at the average for the five inflow boundary conditions; vertical error bars indicate the standard deviation for each such condition. The untreated condition (NT) represents the 100% level in each graph.

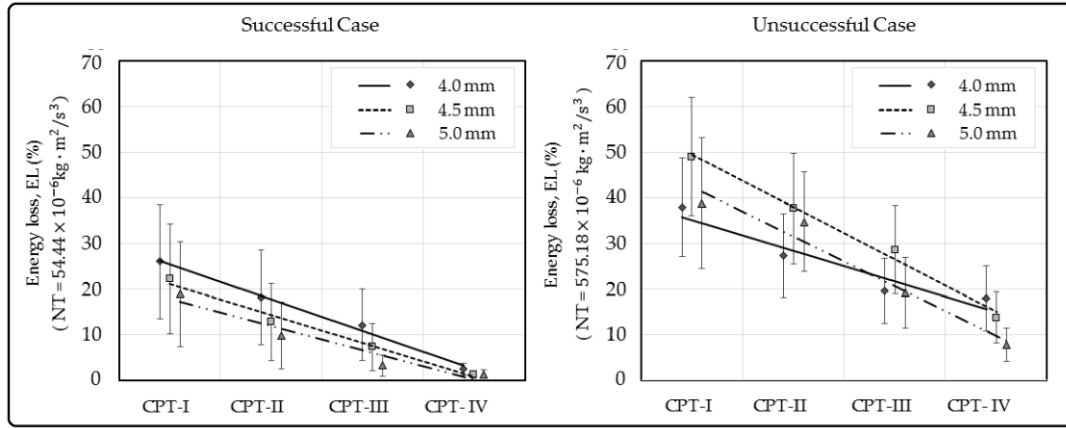


Figure 4-14: Relative values of EL after treatments with a FD stent for three different diameters and four compaction levels. Symbols are plotted at the average for the five inflow boundary conditions; vertical error bars indicate the standard deviation for each such condition. The untreated condition (NT) represents the 100% level in each graph.

4.3.2 Observation of aneurysm flow patterns

CFD results under all five inflow boundary conditions were analysed quantitatively. For additional qualitative examination, representative flow patterns for the inflow condition of 130 mL/min are presented in Figures 4-6 to 4-11. The iso-velocity surfaces (corresponding to respectively 0.025 and 0.1 m/s for the successful and the unsuccessful case) are shown in Figures 4-6 and 4-7; Figures 4-8 and 4-9 depict the streamlines (colour-coded by velocity magnitude) and Figures 4-10 and 4-11 show the wall shear stress (WSS) distributions on the vascular wall.

Before treatment, both successful and unsuccessful cases manifest strong inflow jets. After treatment, whereas an obvious reduction of inflow occurred in the successful case, interestingly, the inflow to the aneurysm in the unsuccessful case remained strong. With the increase of compaction ratio, the inflow jet can hardly be observed in the successful case (at level IV), whereas it still can clearly be identified in the unsuccessful one, suggesting an inferior flow-diversion improvement produced by compaction.

In addition, flow patterns demonstrate no obvious distinctions for different diameters of FD stent at the same compaction ratio.

4.3.3 Reduction of AAV, MF, and EL

Figures 4-12 to 4-14 demonstrate the proportional reduction of AAV, MF, and EL at each compaction level for both cases. Table 4-1 presents the average improvements of flow reduction with one-level advancement of compaction ratio. Table 4-2 gives the maximum differences of flow reduction attributable to the selection of stent diameter and inflow at the same compaction level.

For the respective successful and unsuccessful cases at compaction level I, relative to the values for the untreated condition, the AAV were reduced to 44 and 65 percentage points; the intra-aneurysmal MF decreased to 53 and 66 percentage points; and the EL were reduced to 22 and 42 percentage points (average values for the five inflow boundary conditions). From compaction level I to IV, each 25% increase in compaction ratio leads to average improvements of 14 (AAV), 12 (MF), and 9 (EL) percentage points for the successful case, and 9 (AAV), 9 (MFR), and 9 (EL) percentage points for the unsuccessful case, relative to the untreated condition.

At a given compaction ratio, the averaged maximum differences between values for the three stent diameters were calculated as 10 (AAV), 6 (MF), and 8 (EL) percentage points for the successful case, and 10 (AAV), 9 (MF), and 9 (EL) percentage points for the unsuccessful one.

4.4 Discussion

In this Chapter, a total of 24 virtual treatment scenarios using FDs were demonstrated, with different stent diameter and compaction level applied, for a successfully treated aneurysm case and an unsuccessful one. Results indicate that:

- 1) for a given stent diameter, a 25% increase in compaction ratio led to a further improvement of around 10 percentage points (relative to the untreated condition) in AAV, MF, and EL reduction; and
- 2) at a given compaction level, treatments using different stent diameters could result in a maximum difference of around 9% (compared to the untreated condition) in flow-diversion performance.

4.4.1 Morphological distinctions between the successful and the unsuccessful case

It is found that whether an MCR (equivalent to the unloaded condition) can be achieved post-deployment may depend upon the parent-arterial curvature of the treated aneurysm. Furthermore, compactations performed along a highly-curved artery, with an aneurysm located at the curvature apex, result in a smaller increase in MCR at the ostium.

At compaction level I, the target MCR (predicted based on the unloaded condition) was the same, while the morphology of both treated aneurysms differed markedly. Stents deployed along a highly-curved artery (unsuccessful case), with the aneurysm located at the curvature apex, resulted in a lower MCR (26%); stents deployed along an artery with little curvature (successful case) resulted in a greater MCR (29%). (Figure 4-5)

This phenomenon follows from geometrical constraints. Fitting a stent into a curved artery requires the FD wires to bend towards the curvature apex. Because of this, when an aneurysm is located at the apex, the stent wires located within the aneurysm ostium would dilate into the aneurysm lumen due to the restoring force acting inside the FD (Figure 4-15). In the same way, compacting the stent would push the wires further into the aneurysm lumen, causing a larger discrepancy between the expected and the achieved wire density across the aneurysm ostium. Along with other factors that may affect the achieved MCR [123], the fact that applying the same compaction technique in different patients may not result in the same MCR is something that must be kept in mind by medical doctors.

The FD wires have a potential to dilate into the aneurysm lumen due to the restoring force acting internally inside the FD device, especially if a push-and-pull technique, *i.e.* a technique to deploy FD stent with compaction, was applied during deployment. This is a common phenomenon, which has been addressed in many published studies by not only clinical groups but also simulation teams.

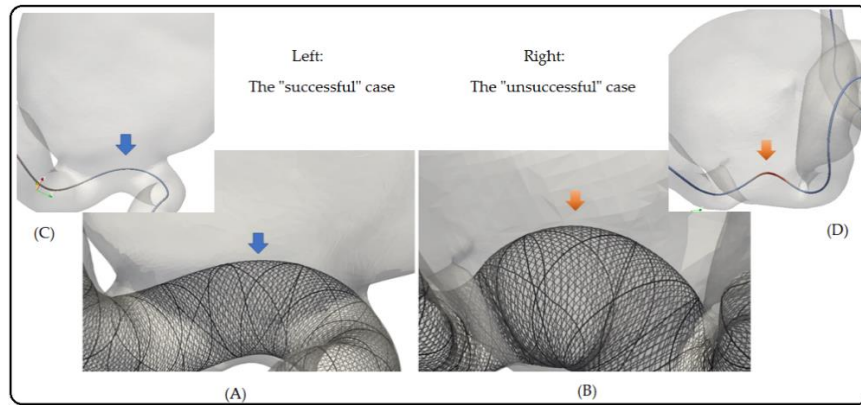


Figure 4-155: The magnified view of FD wire dilation into the aneurysm lumen. Sub-figures (A) and (B) show the FD wires after deployment in respectively the successful and the unsuccessful case; Sub-figures (C) and (D) depict the centerlines extracted from the respective aneurysm geometry for comparison.

In this study, the restoring forces acting inside the FD stent were mimicked by the fictitious springs that connect the FD wire intersections (the substance of the Spring–Mass model). The intensity of the restoring force was controlled by the stiffness of the fictitious springs, and the value of the stiffness I used was adopted from published and validated literature [84,107].

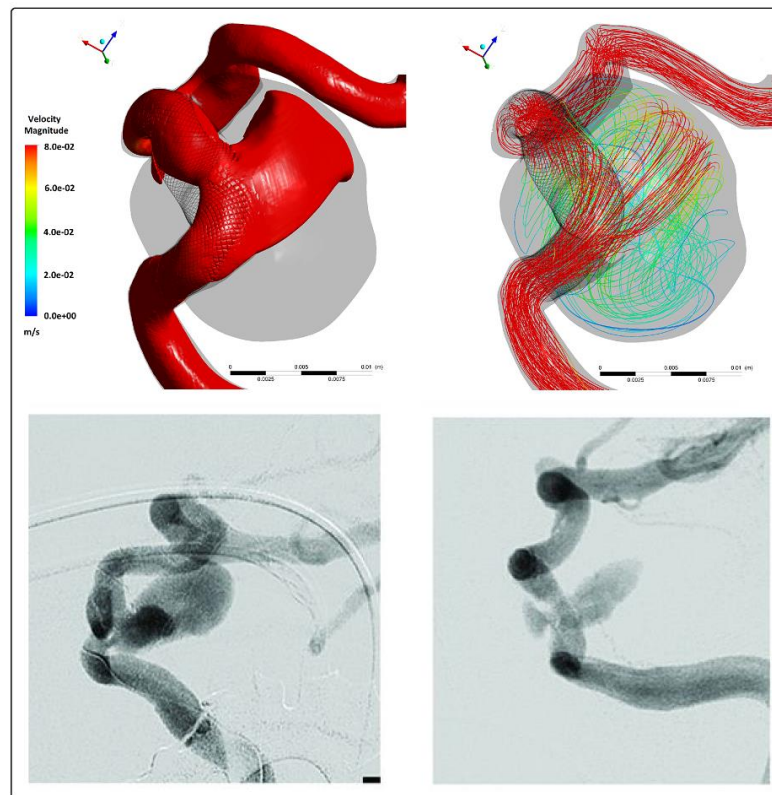


Figure 4-166: Comparison of CFD simulations and angiographic medical imagery for the unsuccessful case. Top: CFD results of iso-velocity surface (left) and streamlines (right); Bottom: DSA images taken upon the 6th month's follow-up after treatment.

The setting of spring stiffness was the same for both the successful and the unsuccessful case, considering that the *Silk+* stents I simulated had the same material properties. In this study, once the value of spring stiffness was assigned during initialisation, no manual intervention was introduced in the later simulation procedure.

As can be identified in Figure 4-7, a jet flow was produced as an additional consequence of the parent artery's morphology in the unsuccessful case. The jet flow enters the aneurysm through a gap between the stent mesh and the arterial wall, which makes the flow unable to be blocked by an FD, even with a level-IV compaction applied. Angiography taken upon the 6-month follow-up revealed the existence of this jet flow, and it matches the CFD simulation results in this study (Figure 4-16). It suggests that FD treatment might be an unsuitable choice for those aneurysms having a similar parent artery morphology to the unsuccessful case in the present study.

4.4.2 Haemodynamic effects of stent compaction

The haemodynamic simulations suggested that each one-level advancement of stent compaction (corresponding to an increment in compaction ratio of 25%) could contribute to a further reduction of aneurysmal inflow, measured on average as AAV: 11, MF: 10, and EL: 9 percentage points of the untreated condition. This study also demonstrated that the proportional reduction of inflow follows a linear trend ($R^2 > 0.85$) with respect to compaction ratio, regardless of the selection of stent diameter or the morphology of a recipient aneurysm (Figures 4-12 to 4-14). Performing stent compaction therefore may be encouraged during stent deployment where practical.

However, it should be noted that FD treatment, even with the maximum compaction, cannot guarantee complete aneurysm occlusion post-treatment. The stent compaction effect can be considerably compromised when compaction is performed along a curved vessel, *e.g.* the unsuccessful case, as in which a level-IV compaction only reduced the AAV, MF, and EL to a degree that can be achieved without compaction in the successful case. This notion was also addressed by previous studies which investigated the FD deployment procedure and post-treatment haemodynamics [124,125].

Over-compacting an FD stent during deployment can result in tragedy, since aggressively advancing the proximal end of an FD might push the wires into the aneurysmal lumen or force the distal end of the FD stent to migrate [88]. I therefore only examined a maximum compaction ratio of 75%. An alternative approach, which only creates a small denser-wire region where blood enters the aneurysm lumen [72], may avoid over-compaction. However, it would be a great challenge for neuroradiologists to find a practicable technique to create such a locally denser wire segment within a small region in the aneurysm ostium.

4.4.3 Haemodynamic effects of device diameter

It can be noticed that the flow-diversion efficacy was affected by the implanted stent diameter. Furthermore, I found that the best stent diameter, *i.e.* the diameter that can produce the highest flow diversion, may differ with respect to compaction levels. For instance, by evaluating the maximal inflow reduction, a 4 mm stent was shown to be the best choice for the unsuccessful case at compaction level I, II, and III, while it turned out to be the worst at compaction level IV (Figures 4-12 to 4-14). This suggests that a deployment rehearsal, along with CFD simulations, could be helpful in deciding a favourable stent diameter and deployment strategy.

A previous haemodynamic study of device oversizing effects reported that treatments using FDs with nominal diameters equal to those of the recipient arteries can maximally reduce the aneurysmal inflow rate, which can be up to 50 % higher than the reductions achieved by using oversized ones [87]. In the present study, I confirmed the existence of a device diameter that could maximally reduce the inflow, and, furthermore, showed that the selection of device diameter needs to take its proposed compaction ratio into consideration.

Finally, it should also be noted that determining the diameter equivalent to that of the recipient artery can be challenging, especially for the aneurysms exhibiting large variation in parent artery diameters. Neuroradiologists faced this problem in dealing with the two aneurysms in this study, since both had large variations in diameter (refer to Chapter 2 for a detailed description). This study demonstrated a numerical approach

which could be used by neuroradiologists to identify the most suitable stent size and treatment strategy that contribute to a favourable haemodynamic modification.

4.4.4 Validation of the FD wire structures post-treatment

In the present study, restricted by the ethics, it is almost impossible to perform *in vivo* validation of FD treatments at different compaction levels, or even to compare the treatments using FD stents of different sizes in a single patient. As an on-going work, my colleagues are performing *in vitro* particle image velocimetry (PIV) experiments to compare the haemodynamics after treatments using different brands of FDs in silicone models. Including some observations from that project would be helpful to verify the deployment simulation in this Chapter.

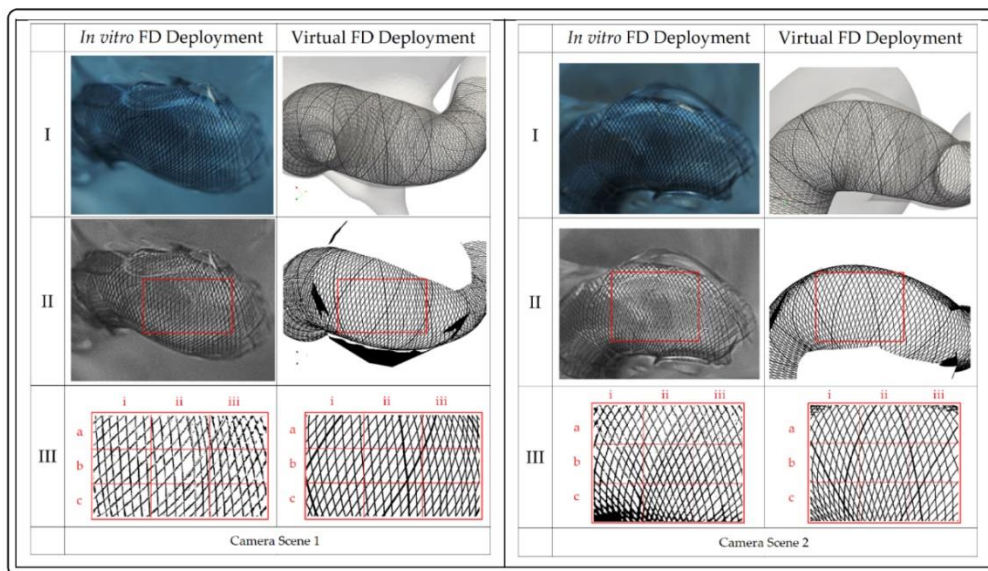


Figure 4-17: The comparison of FD wire structures between *in vitro* and virtual deployments. (Row I: raw images, row II: selecting the region of interest (ROI), and row III: subdomains post image processing. Left and right series are FD wires observed from two camera angles)

As a validation of the deployed stent configuration in this study, the FD wire structures obtained from the virtual deployment were compared with those from a *Silk+* FD stent (with nominal diameter of 4.5 mm and length of 16 mm under unloaded condition) that the medical doctors deployed into a thin-wall silicone model.

Figure 4-17 shows the *in vitro* and the virtual deployment results. A qualitative comparison of the figures suggests that the two sets of results may be compatible.

Table 4-3: The pore-density, porosity, and wire braiding angle measured from the FD structures after virtual and *in vitro* deployments.

Subdomain	Pore-density (pore number)		Porosity (%)		Braiding Angle (degrees)	
	<i>In vitro</i>	Virtual	<i>In vitro</i>	Virtual	<i>In vitro</i>	Virtual
<i>Scene 1</i>						
a(i)	29	28	78.9	72.5	44.2	40.3
a(ii)	28	30	78.3	74.4	47.2	42.8
a(iii)	32	38	74.7	67.7	39.2	38.1
b(i)	25	28	76.4	74.6	48.6	41.6
b(ii)	25	25	79.1	74.4	45.3	45.6
b(iii)	32	33	75.7	72.9	39.1	37.8
c(i)	30	29	75.7	70.1	46.6	43.6
c(ii)	29	26	77.8	71.0	43.2	41.8
c(iii)	28	31	76.5	70.6	45.4	43.4
<i>Scene 2</i>						
a(i)	40	42	78.5	77.3	60.6	56.3
a(ii)	35	39	77.7	81.4	53.3	50.6
a(iii)	40	39	79.7	78.6	57.8	56.3
b(i)	34	35	73.8	73.2	49.2	42.5
b(ii)	35	32	78.0	72.4	49.3	42.5
b(iii)	31	34	78.3	76.6	49.1	49.7
c(i)	47	41	64.1	62.3	44.8	41.2
c(ii)	47	42	72.1	67.4	43.2	38.4
c(iii)	36	35	77.1	73.7	48.9	46.7

To quantify the discrepancies between the two results, the region of interest (ROI, as shown in row II with thick red borders) was divided into nine subdomains (as shown in row III with thinner red borders), and the pore-density, porosity, and wire braiding angle in each paired subdomain were then measured and compared (see Table 4-3 and Figure 4-18).

The pore-density of FD wires was calculated as the total number of pores within one subdomain area. The porosity was defined as

$$\text{porosity}(\%) = \frac{S_{\text{total}} - S_{\text{metal}}}{S_{\text{total}}} \times 100 \quad (4 - 5)$$

where S_{total} denotes the surface area of the subdomain in scene 1 or 2; S_{metal} denotes the total area of the FD wire projections in the corresponding scene plane. The braiding angle was calculated as the average value of all the acute angles in each subdomain.

The data of Table 4-3 demonstrate good agreement in all three structural parameters, which is summarised in Figure 4-18. A paired-samples *t*-test was also performed, and

I confirmed that the simulation results could be interpreted as having the same characteristics as *in vitro* observations ($p < 0.05$).

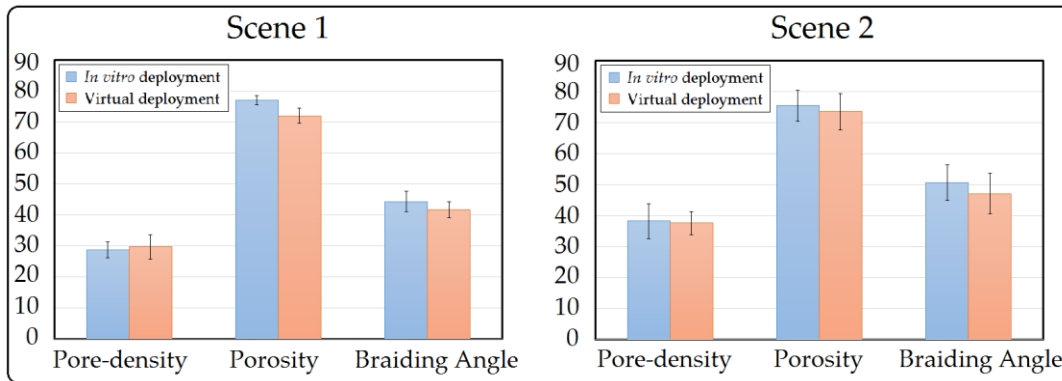


Figure 4-18: Comparison of FD wire characteristics between *in vitro* and virtual deployments in Scenes 1 and 2. Vertical error bars indicate the standard deviation (SD) of the data for each condition.

4.5 Limitation and Future Work

The deployment simulation method did not consider the interaction between the arterial wall and the stent. Although the favourable compliance of the *Silk+* limits its influence on artery deformation, further study is still needed to examine the effects of stent-and-arterial wall interaction on post-stenting wire structures. As it is well-known that the characteristics of artery elasticity are hard to accurately simulate, this will be a challenge of the future work.

Two ICA aneurysm cases were studied, while aneurysms located on other intracranial arteries or with different morphological characteristics need to be examined to confirm the findings reported in this study. It is the future work to include more cases to investigate the correlation between simulation results and clinical outcomes, and likewise to quantify the correlation between parent artery curvature and haemodynamic effects.

4.6 Conclusion

In this Chapter, a total of 24 virtual stenting scenarios were demonstrated for two patient-specific aneurysm cases — one was clinically categorised as a successful

treatment and the other unsuccessful. By contrasting the haemodynamics in the successful and the unsuccessful treatment scenarios, the results indicate the following findings for the first time:

- 1) With stent compaction technique applied, the flow-diversion efficacy in the unsuccessful case can be improved to a level similar to that in the successful case without compaction;
- 2) The change of flow-diversion efficacy with respect to the compaction level follows a linear trend ($R^2 > 0.85$), regardless of the selection of stent diameter or the morphology of a recipient aneurysm;
- 3) The same level of compaction applied to different FD sizes (*i.e.* the stent diameter) could result in different treatment outcomes (with a maximum difference of about 10% in flow-diversion efficacy);
- 4) The virtual stent deployment techniques developed in this study could be used to perform treatment rehearsals, to predict the treatment outcomes.

These findings could plausibly be referred to by clinicians in many circumstances: For example, in the unsuccessful case, if a level-IV compaction had been applied, the treatment outcomes could be improved significantly (a further reduction of inflow by more than 30% of the untreated condition); moreover, clinicians may realise the importance of paying additional attention in dealing with aneurysms located at highly-curved parent arteries.

While the main purpose of the research is to help improve the understanding of a stent compaction technique, under the influence of different device diameters, the 1) FD modelling technique, 2) stent compaction classification, and 3) virtual stent deployment method established in this study, on the other hand, will certainly contribute to the simulation methodologies used in future FD-related research and development.

Chapter 5

Haemodynamic Simulation of Flow-Diversion Treatment with Multiple Flow-Diverting Stents

5.1 Objective

Flow-diversion treatment for IAs sometimes requires the deployment of a second FD stent, due to the insufficient flow diversion produced by the first device. Nonetheless, quantitative haemodynamic analyses before and after the second stent implantation have not yet been systematically carried out.

Various studies have been performed to understand the deployment of FD stents, as well as the haemodynamic alterations caused by the implanted device [31,80,126,127]. Complete aneurysm occlusion is generally believed to be associated with sufficient flow diversion produced by the stent's metal wires that partially cover the aneurysm ostium.

For most treatments, one FD stent would be enough to achieve a favourable haemodynamic modification. Nevertheless, a number of treatments still need the implantation of an additional device (or devices), either planned in the original treatment or added in a subsequent procedure (*e.g.* upon the identification of a residual aneurysm lobule at a routine follow-up), due to the insufficient flow diversion produced by the earlier-deployed one. In a recent retrospective review of treatments with the *Pipeline* stent, it is reported that an average of two devices were used for each aneurysm treatment [128]. However, review of the wider literature suggests that few studies have focused on the possible haemodynamic variations caused by different stent diameters in a multiple FD intervention.

In this Chapter, I seek to quantify the haemodynamic differences caused by the deployment of a second FD, considering the sizing effects of both the earlier- and the later-deployed stents. To meet this objective, a virtual stent deployment technique was employed to create a total of 18 dual-FD stent treatment scenarios, with different combinations of stent diameters implanted into two clinically observed aneurysms. The post-treatment stent wire structures were examined, and the corresponding haemodynamic outcomes were then investigated by CFD simulations.

5.2 Methods

5.2.1 Aneurysm and FD models

The successful and unsuccessful patient aneurysms (see Chapter 2.1 for visualisation of their geometries) were used with an intention of comparing their responses to treatments with multiple FD stents. The patient aneurysm data was accessed after the institutional ethics approval was granted.

In clinical treatments, the successful case attained complete aneurysm occlusion, as confirmed by CTA 6 months' post-treatment. Whereas the CTA scan for the unsuccessful case 6 months post-treatment shows that the aneurysm sac remained transparent. In a second intervention for that patient, neuroradiologists implanted an additional stent into the earlier-deployed one; unfortunately, a residual aneurysm lobule can still be identified 6 months after that treatment. This case may therefore provide some cues of treatment failure if the haemodynamic circulations after each stage's treatment were examined.

The devices I modelled were the *Silk+* FD stents, the same brand as deployed in the real treatments. A spring-mass analogue was employed in the computational modelling of the *Silk+* stent structure and deployment. (Refer to Section 2.2 for a detailed description.)

5.2.2 Multiple FD Implantation

For the deployment of a single stent, the boundary constraint was only the vascular wall. For the deployment of a second stent, I first performed a surface fitting of the fully expanded vertices of the earlier-deployed stent, and then set the fitted surface (treated as a vascular lumen), along with the vascular wall, as the boundary constraints for the deployment of the second stent (see Figure 5-1 for the schematic). A fully expanded status was reached when the movement of each node was less than 1 μm . After this status was reached, I finally converted the FD nodal information to an FD

model by sweeping a circular cross-section through the connected fictitious springs using Paraview.

Given the large variation in the parent-arterial diameter of both cases, a range of stent diameters could plausibly be selected based upon the treating doctors' judgements. I therefore investigated treatments with various device diameters — namely 4.0, 4.5, and 5.0 mm — for the first-deployed stent in each aneurysm. To simulate the follow-up treatments, I deployed an FD stent at each of those three sizes into each of the earlier deployed ones for both patient cases, to examine the possible changes attributable to the size of the second device.

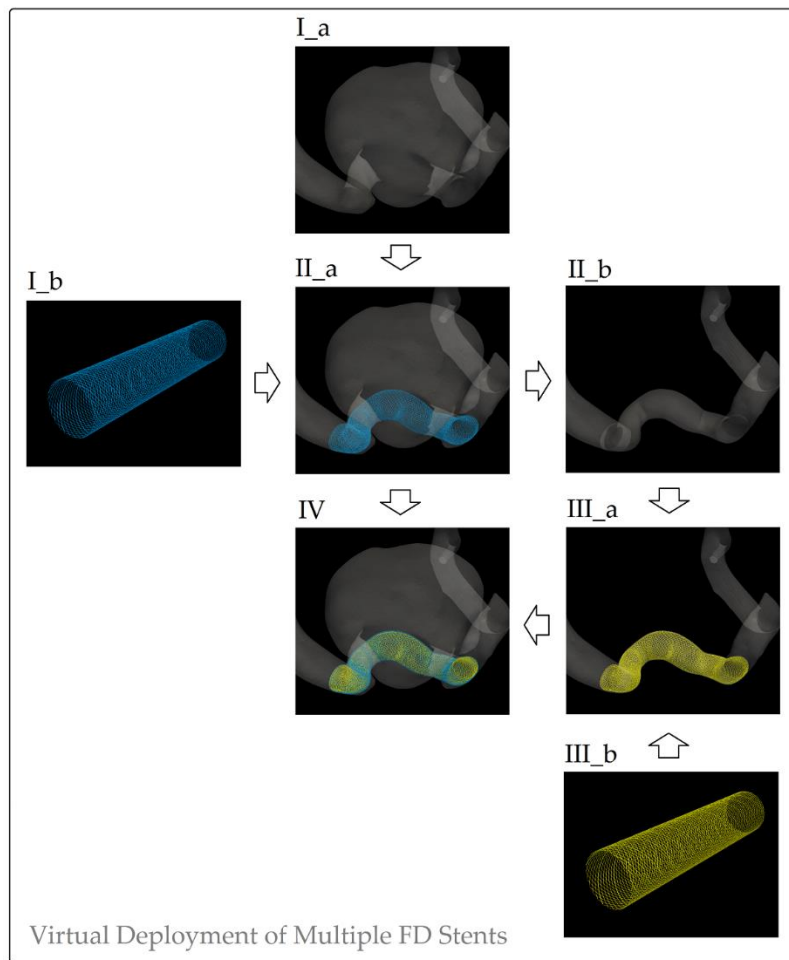


Figure 5-1: Schematic of virtual stent deployment of two FD devices. (I_a: recipient aneurysm geometry, I_b: the first FD stent to be deployed, II_a: deployment of the first stent, II_b: surface fitting of the first deployed stent, III_a: deployment of the second stent, III_b: the second FD stent to be deployed, and IV: aneurysm with two FD stents implanted.)

5.2.3 Haemodynamic Simulation

The arterial wall and stent surface were assumed to be rigid and no-slip condition was imposed at these boundaries. At the inlet of the parent artery, a volume flowrate condition (130 mL/min) was imposed following the previous study [104]; at each outlet, a fixed 0 Pa static pressure was applied. In order to impose a fully developed flow condition at both the inlet and the outlet, the inlet domain was extended 20 times the diameter of the ICA in an upstream direction, and so was the outlet domain in a downstream direction. With acceptable justifications, steady-state flow simulation was performed with assumptions of Newtonian, laminar, and incompressible fluid flow adopted; the density and viscosity of the blood were set respectively as 1050 kg/m³ and 0.0035 Pa·s.

The previous work presented a computational grid generation strategy for the two aneurysm cases [104]. In the present study, the same strategy was applied to generate a tetrahedral grid with maximum sizes of 0.5, 0.08, and 0.008 mm for respectively volume, aneurysm surface, and stent surface, using ICEM-CFD (ANSYS, Canonsburg, USA). (See Figure 5-2 for the representative mesh elements.) Across different cases, the total number of computational grid elements ranged from 12 to 20 million, and the mesh elements falling between any two wires (with an average number of around 20 elements) were considered to be sufficient enough to characterise the flow behaviours in between the wires. The simulation results were obtained by solving the Navier–Stokes equations using the CFX solver for CFD in the ANSYS 16.2 package (ANSYS, USA). The criteria of convergence were chosen as 10⁻⁵ for the normalised continuity and velocity residuals.

Iso-velocity surfaces, streamlines, and wall shear stress (WSS) were examined for each treatment scenario. To quantify the treatment outcomes of each scenario, I calculated the stent wire porosity and pore-density (see Figure 5-15 for the measurement plane) across the aneurysm ostium, intra-aneurysmal mass flowrate (MF), and energy loss (EL).

5.3 Results

Figures 5-3 and 5-4 depict the wire configurations in virtual treatments with a single FD stent ('SFD') or dual FD stents ('DFD') for respectively the successful and unsuccessful cases. Figures 5-5 to 5-10 show the iso-velocity surfaces (corresponding to 0.035 and 0.12 m/s for respectively the successful and the unsuccessful case), streamlines (colour-coded by velocity magnitude), and wall shear stress distributions for respectively the successful and the unsuccessful case. Figures 5-11 and 5-12 present the values of porosity and pore number within the measurement neck planes for respectively the successful and the unsuccessful cases. Figures 5-13 and 5-14 show the relative values of MF and EL after treatments with single or dual FD stents for the two cases. Table 5-1 presents the average reduction of MF and EL after the implantation of a second FD.

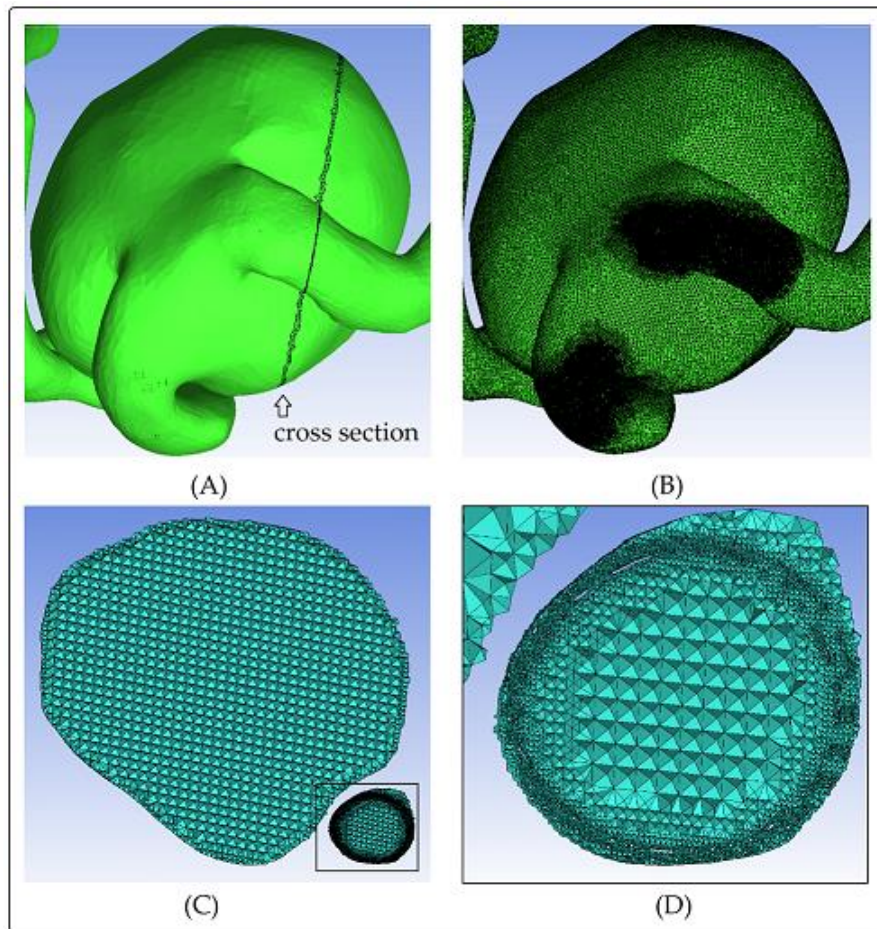


Figure 5-2: The computational mesh of the aneurysm model with two stents deployed in the parent artery. (A) model geometry; (B) model surface mesh; (C) volume mesh in the cross section depicted in 'A'; and (D) magnified view of the stent mesh details enclosed in a square in 'C'.

Table 5-1: The MF and EL reduction (compared to the untreated condition) after treatments with single or dual FD stents. The results for two FD stents are summarised with the means and standard deviations (SD), in which the earlier deployed stent has the same diameter as the single stent in the same row.

	Diameter of outer FD (mm)	MF reduction (%)			EL reduction (%)		
		Single FD	Dual FD		Single FD	Dual FD	
			Mean	SD		Mean	SD
Successful Case	4.0	46.2	30.2	0.3	9.8	1.60	0.1
	4.5	42.7	25.2	1.8	6.4	0.7	0.2
	5.0	38.9	23.2	3.1	4.0	0.4	0.2
	Grand mean	42.6	26.2		6.8	0.9	
Unsuccessful Case	4.0	57.1	43.3	4.2	29.5	13.1	3.2
	4.5	65.3	40.3	4.9	42.8	8.3	2.4
	5.0	58.9	39.0	2.4	32.2	7.4	1.2
	Grand mean	60.4	40.9		34.8	9.6	

MF: mass flowrate, EL: energy loss, and SD: standard deviation.

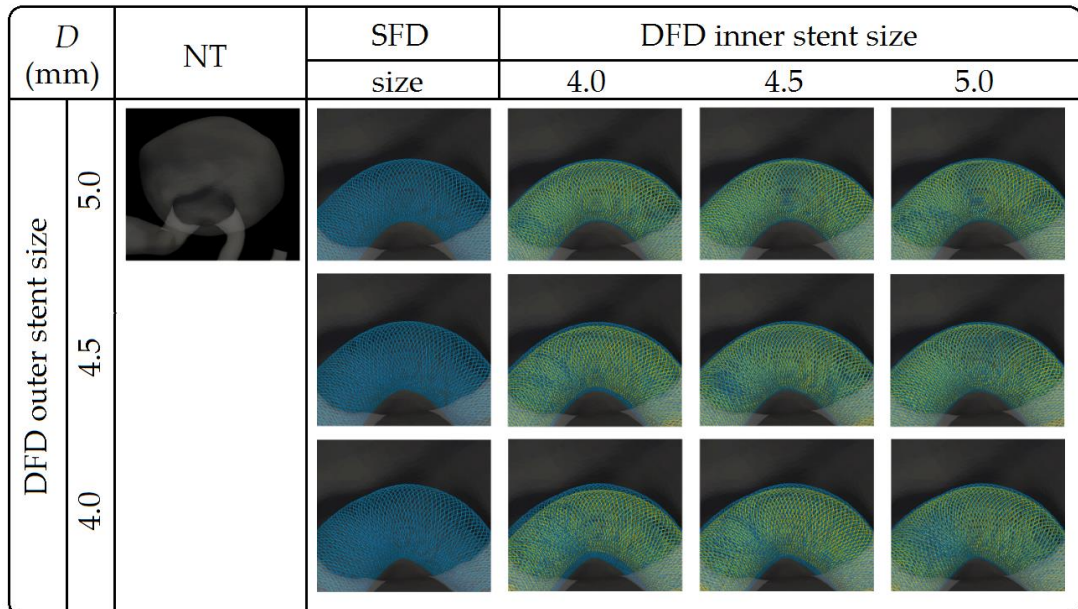


Figure 5-3: FD stent configurations of treatments with single or dual FD stents for the successful case. The untreated case is also shown for comparison. (NT: the untreated condition; SFD: single FD treatment; and DFD: dual FD stent treatment.)

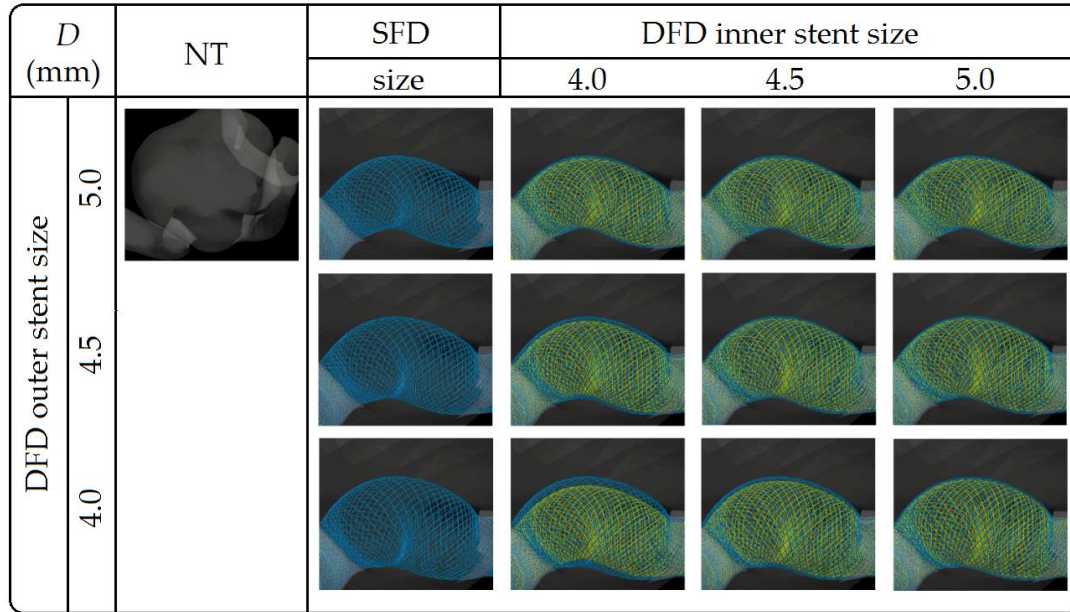


Figure 5-4: FD stent configurations of treatments with single or dual FD stents for the unsuccessful case. The untreated case is also shown for comparison. (NT: the untreated condition; SFD: single FD treatment; and DFD: dual FD stent treatment.)

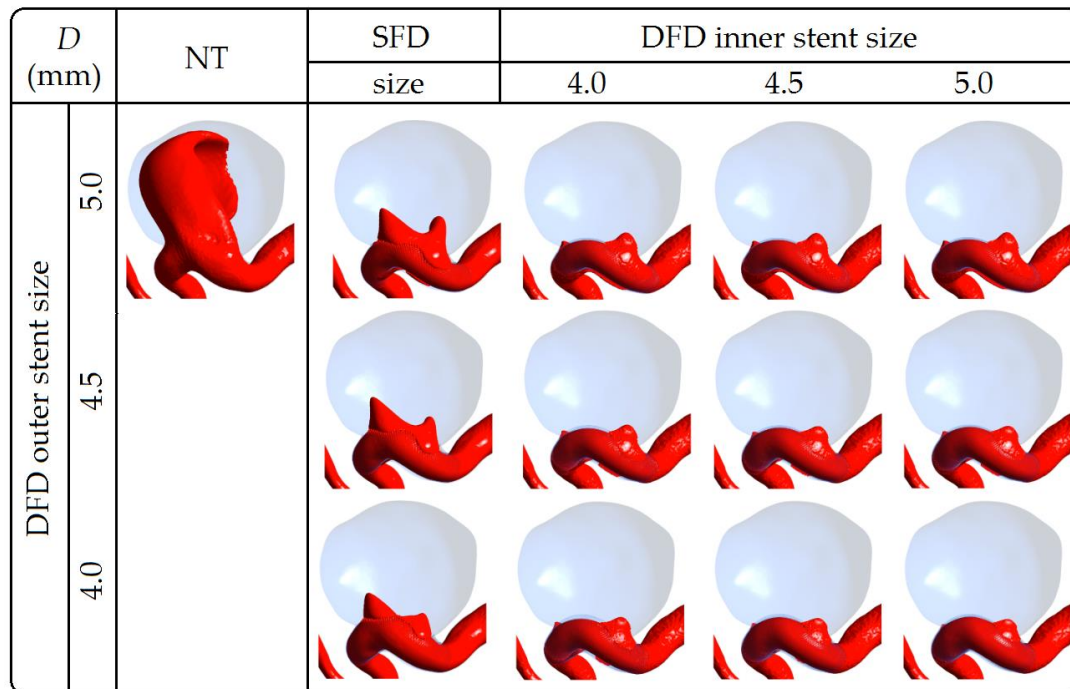


Figure 5-5: Iso-velocity surfaces of treatments with single or dual FD stents for the successful case. The untreated case is also shown for comparison. (NT: the untreated condition; SFD: single FD treatment; and DFD: dual FD stent treatment.)

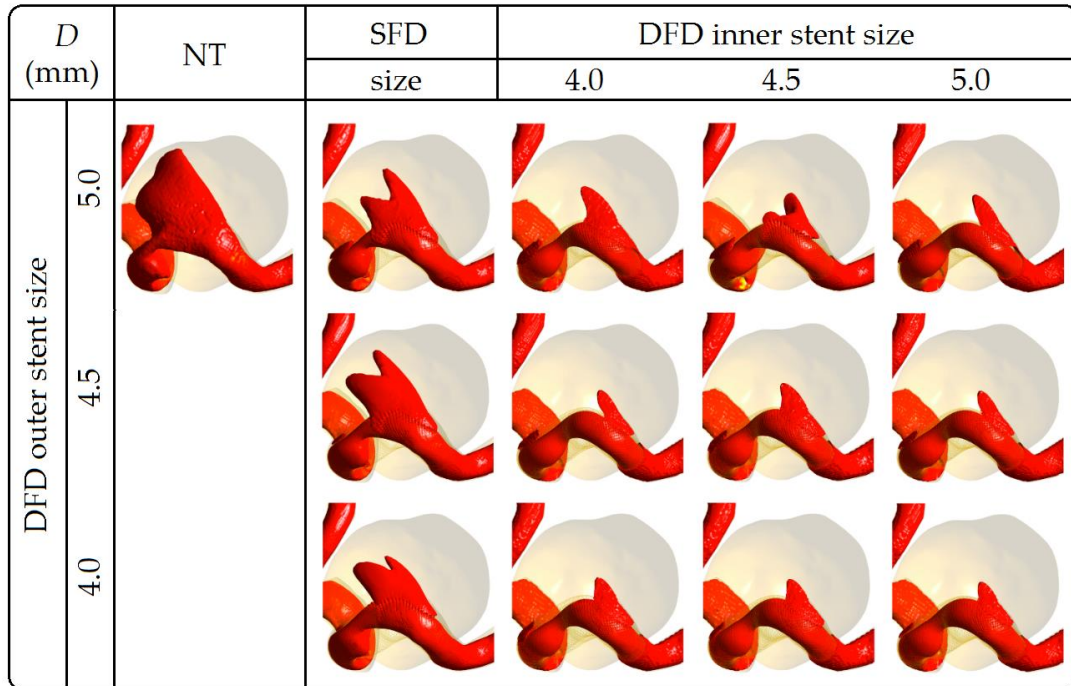


Figure 5-6: Iso-velocity surfaces of treatments with single or dual FD stents for the unsuccessful case. The untreated case is also shown for comparison. (NT: the untreated condition; SFD: single FD treatment; and DFD: dual FD stent treatment.)

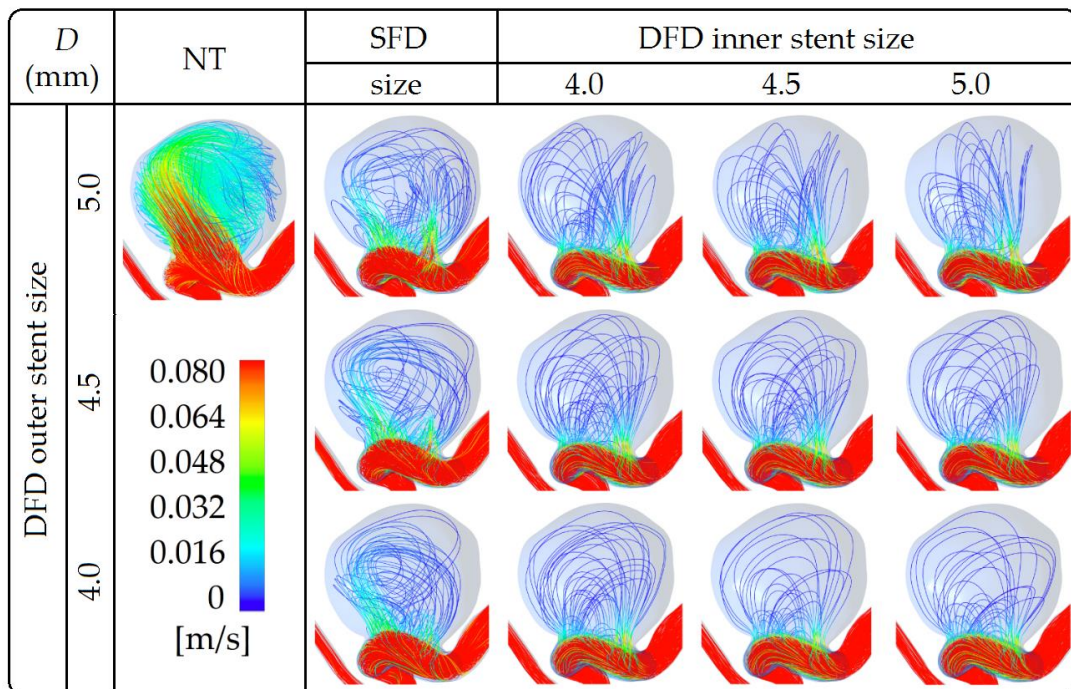


Figure 5-7: Streamlines of treatments with single or dual FD stents for the successful case. The untreated case is also shown for comparison. (NT: the untreated condition; SFD: single FD treatment; and DFD: dual FD stent treatment.)

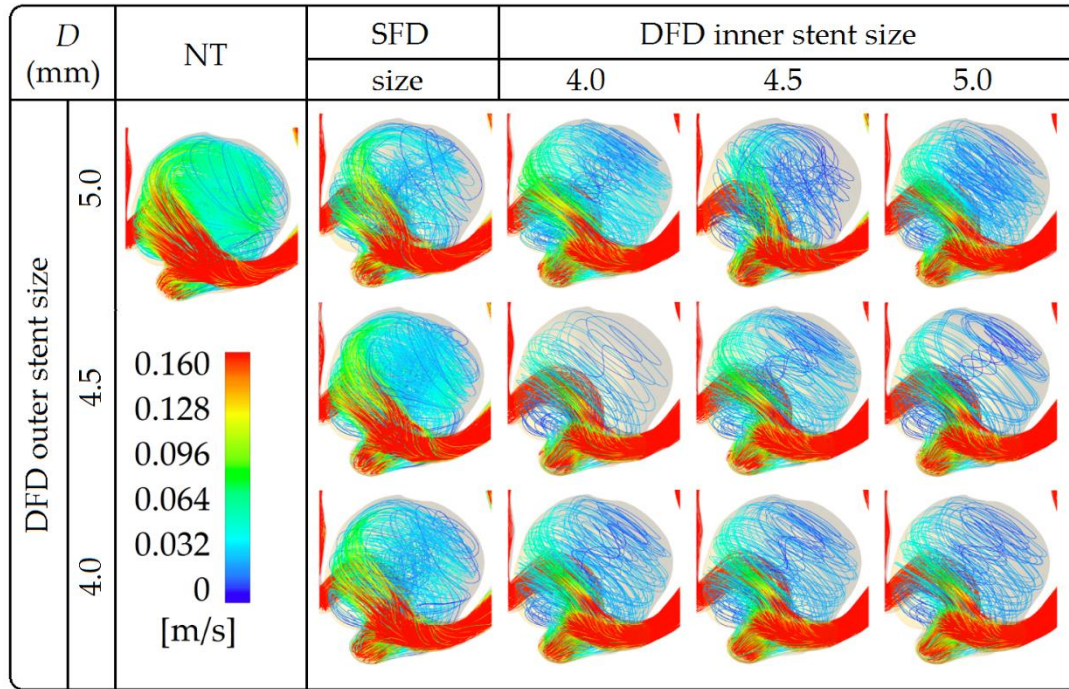


Figure 5-8: Streamlines of treatments with single or dual FD stents for the unsuccessful case. The untreated case is also shown for comparison. (NT: the untreated condition; SFD: single FD treatment; and DFD: dual FD stent treatment.)

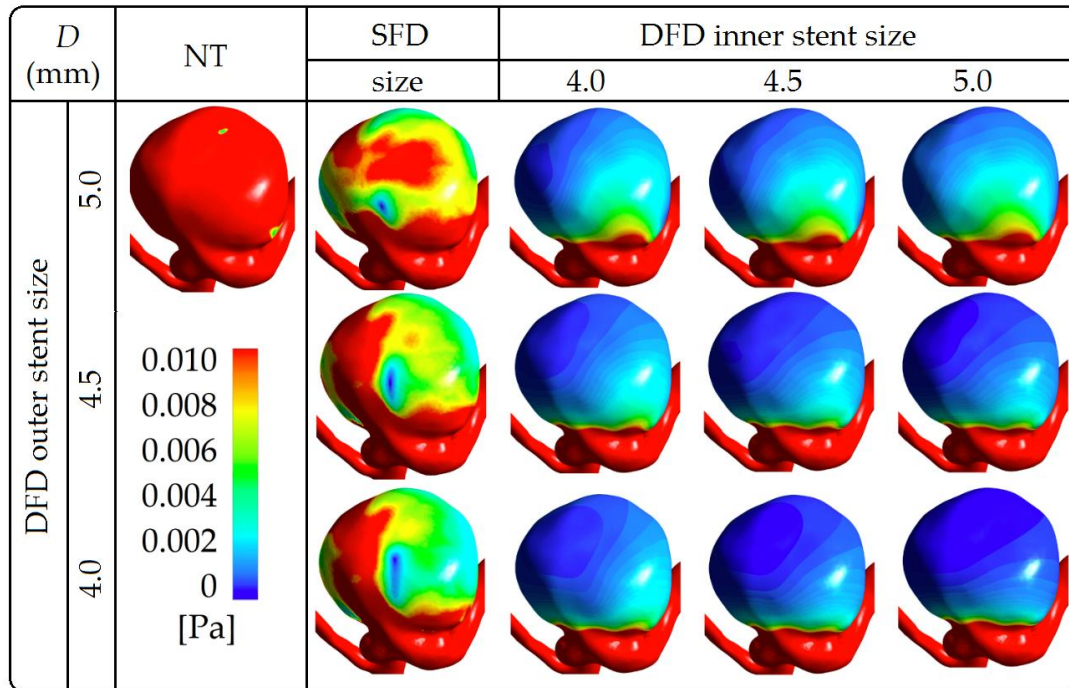


Figure 5-9: WSS of treatments with single or dual FD stents for the successful case. The untreated case is also shown for comparison. (NT: the untreated condition; SFD: single FD treatment; and DFD: dual FD stent treatment.)

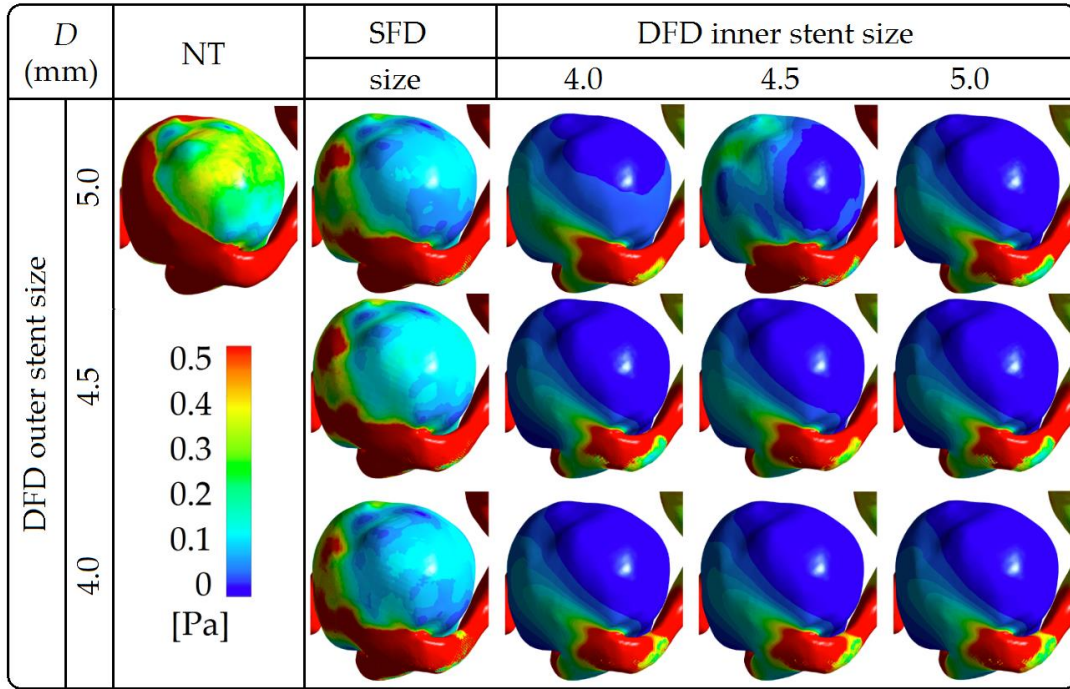


Figure 5-10: WSS of treatments with single or dual FD stents for the unsuccessful case. The untreated case is also shown for comparison. (NT: the untreated condition; SFD: single FD treatment; and DFD: dual FD stent treatment.)

5.3.1 Stent wire configurations, porosity, and pore-density

Figures 5-11 and 5-12 present the values for porosity and number of pores within the neck measurement planes. As reported by Shapiro *et al.* [129], the mesh density would not just be simply doubled after the deployment of a second device, but would lie in a range between the conditions of completely overlapped stent wire braids and perfectly half-phase separated braids, depending upon the recipient artery's morphology. In the present study substantial increases in mesh density was observed: for the successful case, the average number of pores rose from 1020 ('SFD') to 2260 ('DFD'), and the average porosity was reduced from 60% ('SFD') to 45% ('DFD'); for the unsuccessful case, the average number of pores was elevated from 1000 ('SFD') to 2090 ('DFD'), and the average porosity decreased from 78% ('SFD') to 58% ('DFD'). Note that the numbers of pores were calculated based upon the same respective measurement planes for the successful and unsuccessful cases; therefore, they are immediately correlated with the pore density corresponding to each such measurement plane.

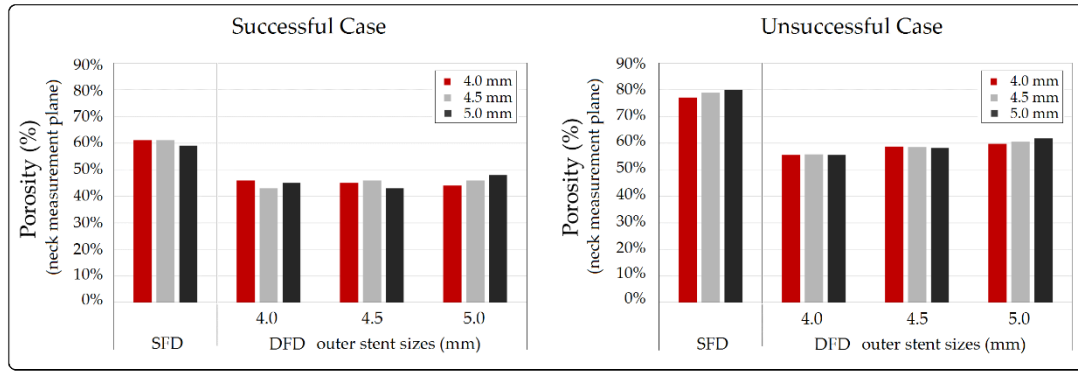


Figure 5-11: Porosities within the neck plane after treatments with single or dual FD stents for respectively the successful and the unsuccessful cases. Stent sizes on the horizontal axis indicate the outer (earlier deployed) stent diameter; stent sizes represented by different colours in the legend indicate the inner (later deployed) stent diameter. (SFD: treatments with a single FD stent and DFD: treatments with two FD stents.)

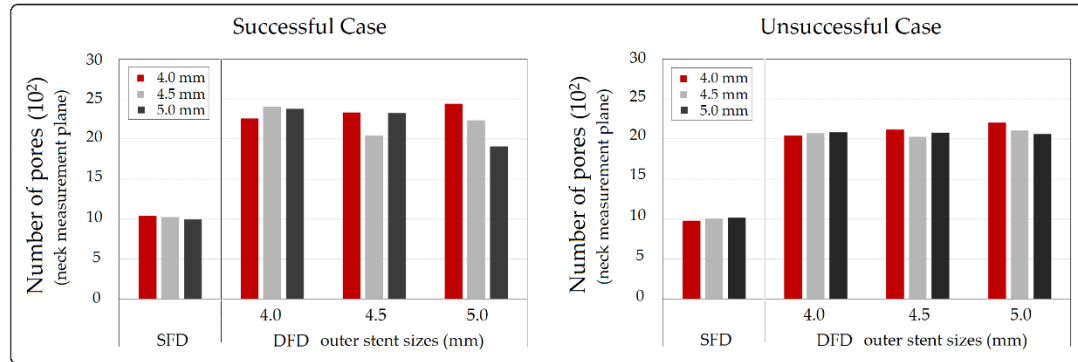


Figure 5-12: Number of pores within the neck plane after treatments with single or dual FD stents for respectively the successful and the unsuccessful cases. Stent sizes on the horizontal axis indicate the outer (earlier deployed) stent diameter; stent sizes represented by different colours in the legend indicate the inner (later deployed) stent diameter. (SFD: treatments with a single FD stent and DFD: treatments with two FD stents.)

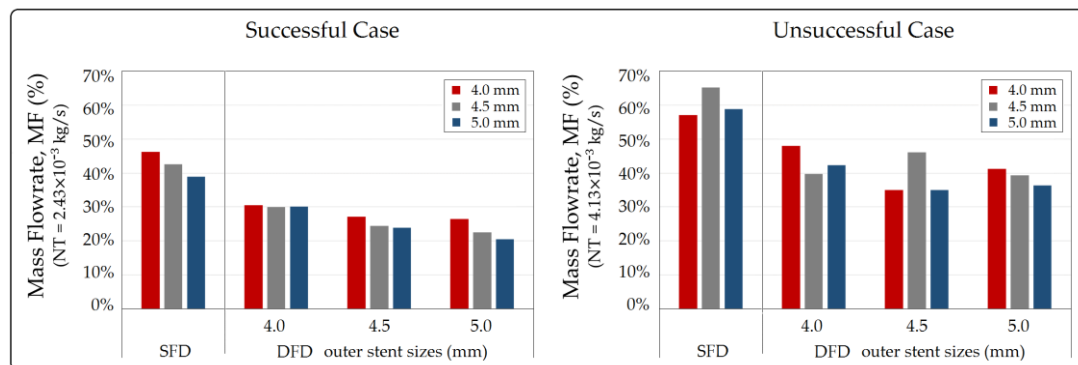


Figure 5-13: Relative values of intra-aneurysmal MF after treatments with single or dual FD stents for respectively the successful and the unsuccessful cases. Stent sizes on the horizontal axis indicate the outer (earlier deployed) stent diameter; stent sizes represented by different colours in the legend indicate the inner (later deployed) stent diameter. (SFD: treatments with a single FD stent and DFD: treatments with two FD stents.)

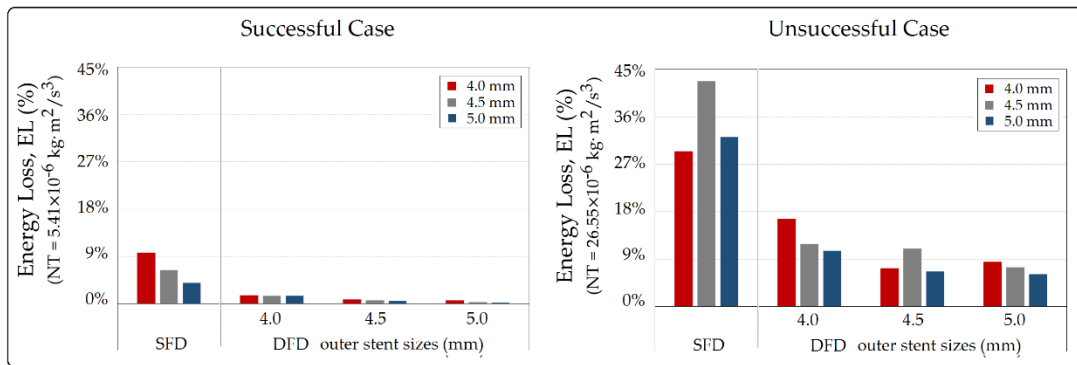


Figure 5-14: Relative values of intra-aneurysmal EL after treatments with single or dual FD stents for respectively the successful and the unsuccessful cases. Stent sizes on the horizontal axis indicate the outer (earlier deployed) stent diameter; stent sizes represented by different colours in the legend indicate the inner (later deployed) stent diameter. (SFD: treatments with a single FD stent and DFD: treatments with two FD stents.)

Comparing the wire structures between treatments using dual FD stents, gaps can clearly be observed between stent layers, when a stent of smaller diameter was deployed into another of larger diameter, *e.g.* when a 4 mm stent (inner) is inside a 5 mm stent (outer). For the successful case, the lowest pore density and the highest porosity were obtained when the later- and earlier-deployed stents were of identical diameters. For the unsuccessful case, the lowest pore density accompanies treatments with dual FD stents of identical diameters, whereas no obvious according trend in porosity was found except for the 5 mm into 5 mm case, compared to the scenarios with dual stents of different diameters.

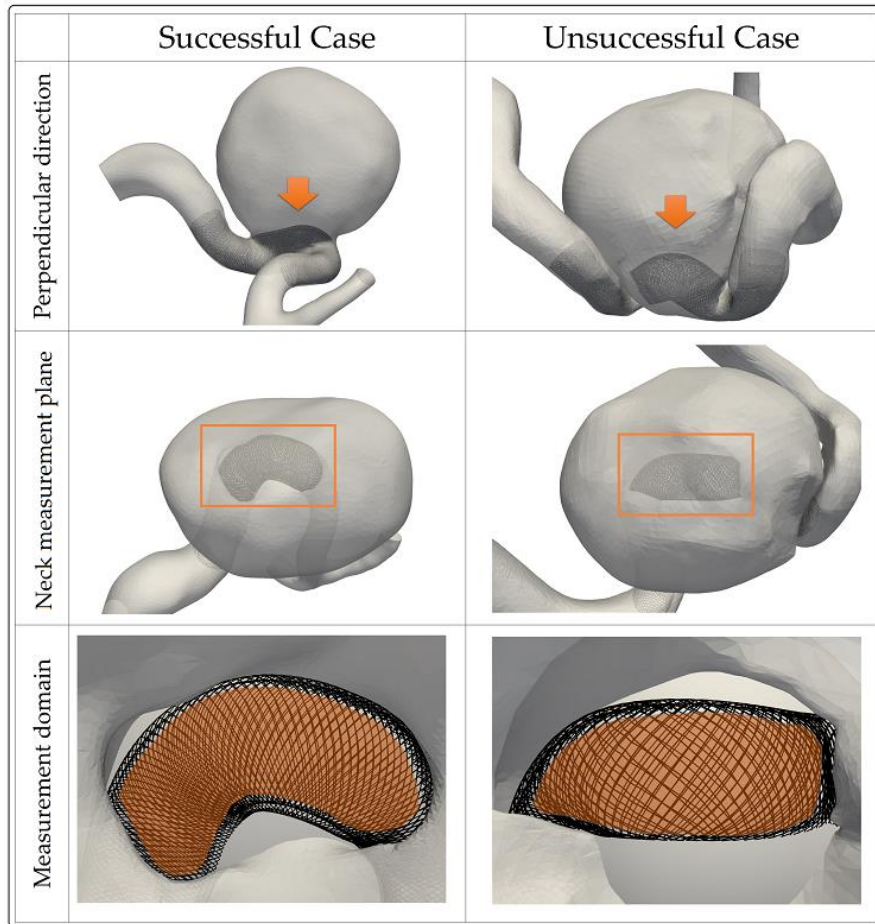


Figure 5-15: The measurement domains selected for calculating porosity and number of pores in both aneurysm cases. Arrows indicate the perpendicular direction to the neck planes; rectangles show the boundaries of neck measurement planes; and the orange areas indicate the domains used for calculating the porosity and number of pores.

5.3.2 Aneurysmal flow patterns

Under the untreated condition, a strong impingement flow can be observed entering the aneurysm lumen in both cases. After the treatment with one FD stent, the impingement flow was markedly reduced in the successful case, whereas it remained strong in the unsuccessful one. With the deployment of a second stent, the successful case manifests no obvious impingement flow; in contrast, an inflow jet can easily be identified in the unsuccessful case. As can be observed in Figures 5-7 to 5-10, the WSS and the velocity magnitude on streamlines traversing the aneurysm sac are further reduced by treatments with dual FD stents.

5.3.3 Aneurysmal haemodynamics

After the implantation of the second FD stent, the intra-aneurysmal MF and EL reductions were further improved. Relative to the values of the untreated condition, the average MF and EL decreased from 42.6% and 6.8% ('SFD') to 26.2% and 0.9% ('DFD') for the successful case; and from 60.4% and 34.8% ('SFD') to 40.9% and 9.6% ('DFD') for the unsuccessful case. No substantial difference was observed in post-treatment haemodynamics between scenarios with a second FD of different diameters (standard deviation < 5% for both MF and EL).

5.4 Discussion

In this Chapter, eighteen virtual FD treatments with dual stents of different sizes deployed were characterised for successfully and unsuccessfully treated aneurysms. Results indicate that:

- 1) deployment of a second FD could lead to a further reduction of intra-aneurysmal MF of about 20 percentage points, compared to the treatment with a single device;
- 2) haemodynamic differences attributable to the size of the later-deployed device were modest, with a standard deviation less than 5 %; and
- 3) flow diversion achieved with two stents in the unsuccessful case was similar to that with only one FD implanted in the successful case. (All values are relative to the untreated condition.)

Each of these key findings are discussed in more detail below.

5.4.1 Mesh density and flow diversion enhanced by the second device

After the treatments with a second device, an additional 20 percentage points (on average) decrease of porosity, and an approximate doubling of pore density were gained, compared to the treatments with a single FD. These parameters are in good agreement with the mesh-density increment reported in previous multi-FD stent studies [129–132]. Moreover, I found that the increase in mesh density due to the

second device may vary from aneurysm to aneurysm: herein the unsuccessful case accrued a greater improvement than did the successful one (Figure 5-12). This may, most likely, be due to the morphological characteristics of the aneurysm parent arteries as discussed in the previous study.

The larger improvement of mesh density in the unsuccessful case may be the reason for a subsequent greater additional reduction of aneurysm inflow: the additional MF reductions (see Figure 5-13) were respectively 16 and 20 percentage points for the successful and the unsuccessful case, and the EL reductions 6 and 25 percentage points — the unsuccessful case received a greater benefit from the second device. However, interestingly, the final flow diversion achieved in the unsuccessful case was only improved to a level similar to that with a single FD implanted in the successful case: intra-aneurysmal MF and EL values of 40.9% and 9.6% (the unsuccessful case with ‘DFD’) versus 42.6% and 6.8% (the successful case with ‘SFD’).

These findings indicate that: 1) the deployment of a second FD stent generally improve the flow-diversion efficacy, regardless of the stent diameters to be deployed or the morphology of the aneurysm to be treated; 2) the significance of additional flow diversion by a second device might be dependent upon the recipient artery’s morphology; and 3) it is not guaranteed that the deployment of an additional device would convert an otherwise unsuccessful case into a successfully treated one.

5.4.2 Effects of different stent diameters in dual-FD treatment

It can be observed that the overlap of two FD stents with the same diameter produced the lowest pore density, compared to treatments with stents of different diameters. This phenomenon can be explained by a previous study [129], which found that treatments with two identical-diameter stents can lead to a lower coverage gain than those with two different-diameter stents. A possible cause is that the braids of the two identical-diameter stents can overlap with each other due to the similar braiding angles post-deployment. (See Figure 5-16 for the nearly-overlapped and the uniformly distributed wire braid configurations observed from the simulation.)

Simple theories of fluid mechanics indicate that flow resistance would depend upon porosity as well as pore size, with pore density being a surrogate measure for the latter [133]. Nonetheless, a higher pore density does not necessarily produce a higher flow diversion, *e.g.* the dual 5 mm stents (with the lowest pore density observed in the successful case) achieved the highest flow diversion. Stent size is just a single piece of the puzzle that would affect haemodynamics post-treatment; the selection of stent diameter for a multi-FD treatment should take many factors into consideration, such as the possible over- or under-sizing effect, the specific geometry of a patient aneurysm, the region where the main aneurysm inflow occurs, *etc.*

In addition, partially overlapping two stents provides an extra advantage when dealing with aneurysms that have a large variation in parent-arterial diameter, especially when the variation is large between the stent's distal and proximal landing zones [129]. This technique usually applies to a fusiform aneurysm, creating a partial overlap of two devices, with the diameter of each stent respectively matched to that of the distal and the proximal landing zones. However, the haemodynamic changes for fusiform aneurysms following treatments applying this technique deserve further investigation.

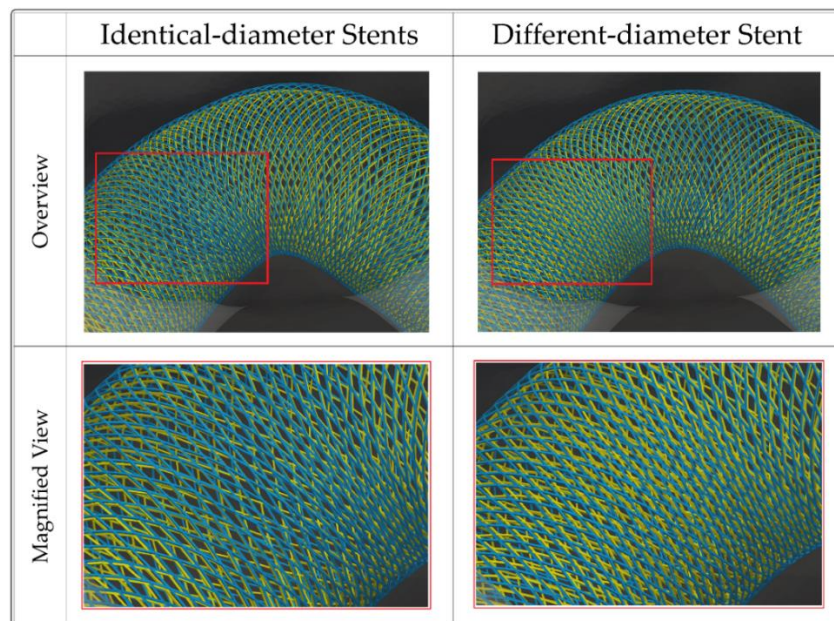


Figure 5-16: The stent wire configurations observed in dual-FD stent treatments with identical-diameter stents (inner stent 5 mm, outer stent 5 mm) and with different-diameter stents (inner stent 5 mm, outer stent 4.5 mm) for the successful case. Top row: overview of the two scenarios. Bottom row: magnified view of the rectangular region (identifying the aneurysmal inflow segment) outlined in red in the overview images.

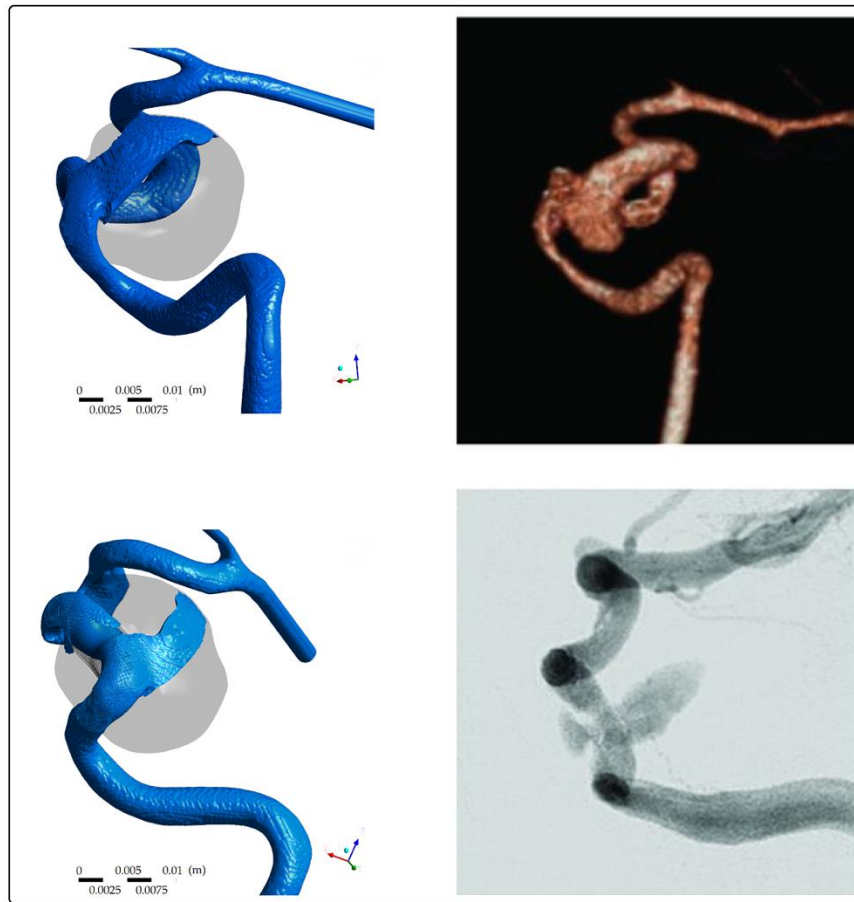


Figure 5-17: Comparison of CFD simulations and angiographic medical imagery for the unsuccessful case. Left: CFD results of iso-velocity surfaces visualised from two different angles; Right: three-dimensional CTA (top) and DSA image (bottom) taken after the second FD stent treatment.

5.4.3 Different haemodynamic outcomes in two patient aneurysms

Treatments for the successful aneurysm, with a single FD device applied, resulted in considerable haemodynamic changes, regardless of the device diameter. This can be observed from the markedly weakened inflow jets, which impinge against the aneurysm wall under the untreated condition (Figure 5-5).

The mechanism of a successful treatment may plausibly be explained from the viewpoint of haemodynamics that an effective blockage of any inflow jet might contribute to complete occlusion of the aneurysm. The same speculation was addressed and discussed in detail by Fischer *et al.* [134]. In addition, the study confirmed that even with an impressive flow diversion achieved by one FD, as in the

successful case, further inflow reduction is still attainable by the implantation of a second device.

Unlike the successful case, the various treatments of the unsuccessful aneurysm with FD stents produced limited disruption of inflow, even after the deployment of a second FD had increased the wire density across the aneurysm ostium (Figures 5-4, 5-11, and 5-16). The appearance and location of the persisting inflow jet observed from CFD simulation match the inflow lobule identified in the CTA scan taken at the 6 months' follow-up after the second treatment (Figure 5-17). Observing the inadequate outcomes from clinical treatment, consistent with the modelling results, FD stent implantation might therefore be categorised as an unsuitable solution for this patient's aneurysm.

The finding of a strong persisting inflow after dual FD stent treatment in the unsuccessful case suggests that haemodynamic simulations prior to the real *in vivo* treatment might reveal some clues as to the sufficiency of the flow diversion effect, such that unsuitable treatments can be avoided, and other effective approaches can be considered to better benefit the patient and achieve the desired outcome.

5.5 Limitation and Future Work

This study has several limitations. For the simulation of stent deployment, I did not consider the interaction between the earlier- and the later-deployed stents, as well as the interaction between the stent wire and the arterial wall, due to the lack of information about stent mechanical properties, elasticity of arterial wall, *etc.* Twin challenges of the future work will be to obtain relevant physical property data for these parameters and then to incorporate this information into more complicated mathematical models of the behaviours of the stent and vascular wall.

Another limitation is the quantity of patient models. I proposed to study representative aneurysms clinically classified as successfully treated and unsuccessfully treated, and the good agreement of the results with the patients' follow-up scans provides reassurance as to the validity of the modelling. Still, even though distinct

haemodynamic outcomes were confirmed for the successful and the unsuccessful patient aneurysm in the present study, whether those findings apply to other cases may need further investigations. It is the on-going work to perform haemodynamic simulations for additional clinically observed cases from the aneurysm database.

Finally, the discussion of treatment outcome relies on an association between haemodynamics and occlusion (or, conversely, risk of rupture), as has been presented previously in the literature [36,71]. Currently the ability to computationally model the process of thrombosis leading to partial or complete occlusion of an aneurysm is still being developed, although progress is being made [135,136].

5.6 Conclusion

In this Chapter, virtual stent deployments and haemodynamic simulations were performed for a total of 18 dual-FD treatments, with different combinations of stent diameter considered for two clinically observed aneurysms — one successfully treated with an FD and the other unsuccessful after two FDs were implanted.

Using a virtual deployment technique, I first implanted FD stents of respectively three sizes — 4.0, 4.5, and 5.0 mm — into both aneurysms; and then deployed a second device of respectively the same three sizes into each of the earlier deployed ones. Finally, I compared the stent wire configurations across the 18 treatment scenarios, and investigated the post-stenting haemodynamics by computational fluid dynamics (CFD) simulations.

Attributable to the second device, results indicate that 1) the stent porosity can be further decreased by approximately 20 percentage points and the pore-density doubled; 2) an additional reduction of aneurysmal inflow (around 20 percentage points) can be gained; and 3) diameter of the later-deployed device has limited effects on post-treatment aneurysmal haemodynamics (standard deviation < 5%).

Despite a greater flow-diversion improvement resulting from the second device, the final haemodynamic status in the unsuccessful case was only comparable to that with

one FD implanted in the successful case, suggesting that FD stents might be an unsuitable choice for the unsuccessful aneurysm.

This illustrates that haemodynamic simulation is helpful in the estimation of treatment outcome, so as to assist clinicians in choosing a favourable treatment plan.

Chapter 6

Investigation of Incomplete Stent Expansion Effects on Aneurysmal Haemodynamics

6.1 Objective

For deployment of a FD stent, complete expansion of stent wires and firm wall apposition of stent struts are recommended to resist post-treatment stent migration as well as in-stent stenosis. This is because recent experimental studies reported that a better wall apposition plays an important role in inducing aneurysm occlusion [137,138], whereas malapposition of stent wires may cause delayed stent endothelialisation and even pose risks for stroke-related complications [139,140].

Although incomplete stent expansion (IncSE) — also termed stent malapposition when the collapse of wires occurs at the proximal or the distal end of a stent — is not a common condition, research into it has been recently reported thanks to the advancement of medical imaging approaches: *e.g.* optical coherence tomography (OCT), and high-resolution contrast-enhanced cone-beam computed tomography [132,140,141]. In those studies the biological consequences raised by IncSE were intensively investigated; however, the effects of IncSE on aneurysm haemodynamics have not yet been characterised, even though the haemodynamics are thought to constitute a vital factor that affects aneurysm occlusion [30,31,34].

In this Chapter, I attempt to quantify the aneurysm haemodynamics affected by different severities of IncSE that occurs in different segments of the aneurysm's parent artery, so as to better understand the mechanism of late aneurysm occlusion related to IncSE. To meet this need, virtual FD treatments were performed with IncSE respectively modelled at two severity levels — severe (S) and intermediate (I) — located in the proximal, central, and distal segments of the parent artery of two aneurysms where IncSE was identified in the real treatment. The morphological characteristics of FD stents in the 14 treatment scenarios were examined and the aneurysm haemodynamics were investigated by use of CFD.

6.2 Materials and Methods

6.2.1 Patient Aneurysms

Institutional ethics approval was obtained before I accessed the patient aneurysm data. Two cavernous aneurysm treatments were studied, in which IncSE was identified by digital subtraction angiography (DSA) — one was located at the right internal carotid artery (ICA) (case ‘A’), and the other was at the left ICA (case ‘B’).

Case ‘A’ was treated with a 5.0×18 mm *Pipeline Embolization Device* (PED, Medtronic Neurovascular, U.S.A.), and IncSE was identified within the segment of the aneurysm orifice. Case ‘B’ was treated with a 5.0×20 mm PED stent, in which a severe stent malapposition was found at the FD stent’s distal end.

6.2.2 Classification of IncSE

Along the length, a deployed FD stent was classified into three segments — ‘*p*’, ‘*c*’, and ‘*d*’ — which respectively refer to the segment of stent proximal to the aneurysm, bridging the aneurysm orifice, and distal to the aneurysm. IncSE may occur within any of the three segments, or throughout two consecutive segments, depending upon the morphological characteristics of the parent artery [137]. (See Figure 6-1 for the morphological analysis of the parent arteries of the two cases.)

As IncSE does not occur frequently, to investigate a wide variety of IncSE scenarios, FD treatments were studied with IncSE respectively modelled at two severity levels — severe (S) and intermediate (I) — located in each of three defined FD stent segments — the ‘*p*’, ‘*c*’, and ‘*d*’ segments — which yielded 6 IncSE scenarios (‘*p-S*’, ‘*p-I*’, ‘*c-S*’, ‘*c-I*’, ‘*d-S*’, and ‘*d-I*’) for each of the two cases.

As malapposition occurring in the ‘*p*’ or ‘*d*’ segment may be associated with high curvature of an artery [141,142], two locations (‘*pM*’ and ‘*dM*’, as depicted in Figure 6-1) with large centreline curvature were assumed to be the positions where IncSE could occur. To quantify the severity of IncSE, stent diameters measured from their cross-

sectional planes at these two locations were adopted: I assumed that a severe (S) or an intermediate (I) level of IncSE had a diameter of 30 or 60% of that when the stent was ideally deployed. Likewise, for IncSE occurring in the 'c' segment, stent radius measured from the cross-sectional plane at location 'cM' (see Figure 6-1) was used to quantify the IncSE severity: a severe (S) or an intermediate (I) level of IncSE was assumed to be 50 or 75% of that under the ideal deployment condition. (See Figure 6-2 for a schematic illustration of IncSE classification.)

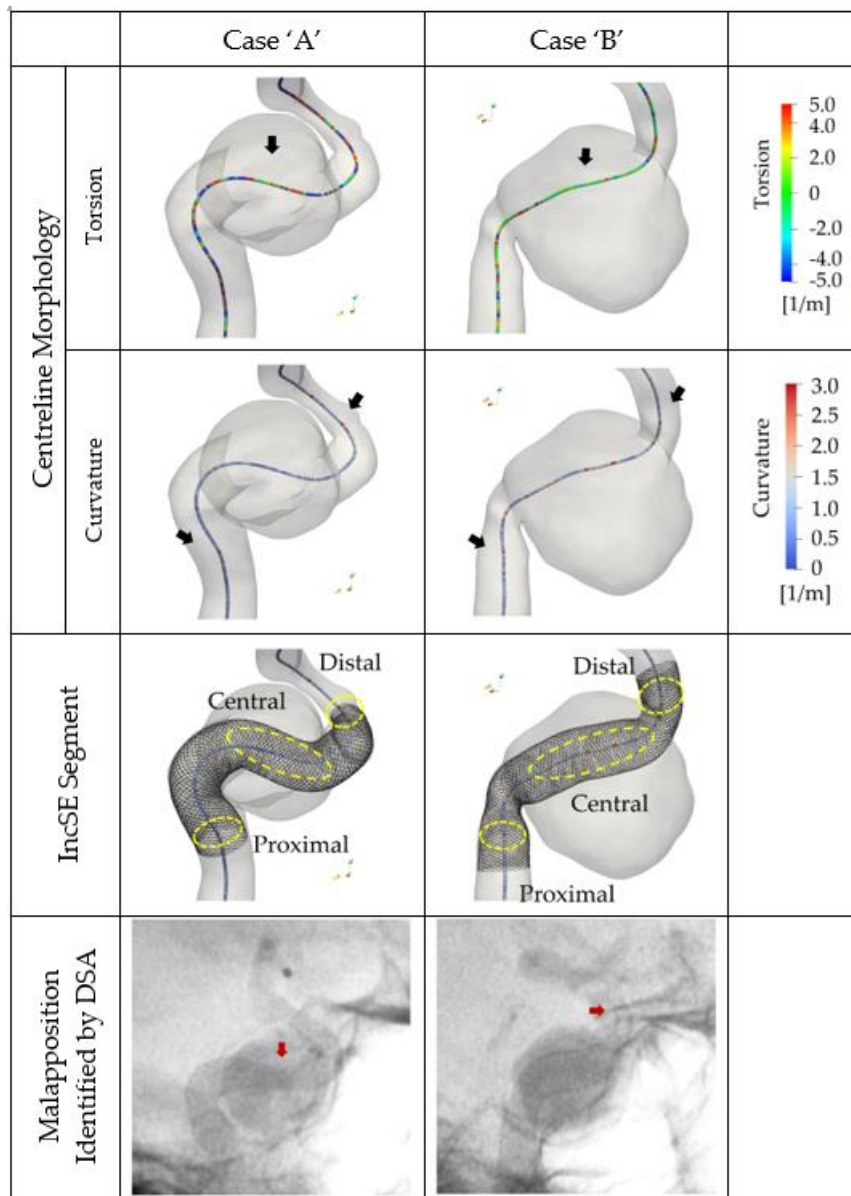


Figure 6-1: Centreline trajectories colour-coded by curvature (row 1) and torsion (row 2); segments of stent where IncSE may occur (row 3); and the IncSE observed *in vivo* (row 4) for case 'A' and 'B'. Red arrows indicate the observed IncSE; black arrows indicate reference location for quantifying degree of IncSE; and yellow dashed circles and ovals indicate the location of the labelled regions.

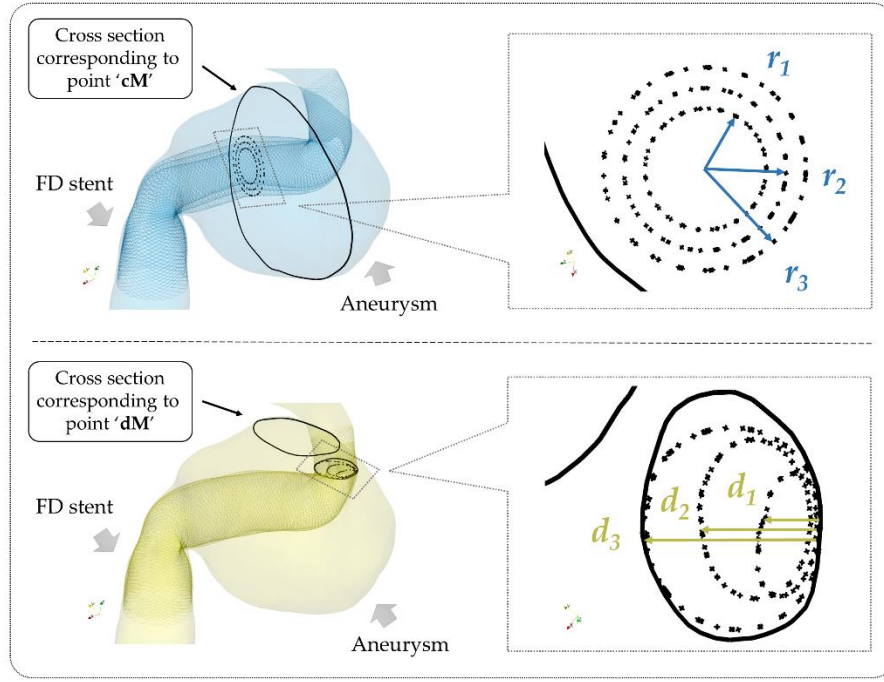


Figure 6-2: Schematic for the determination of different levels of IncSE occurring in the central (top) and the distal (bottom) segment of a FD stent. A central IncSE is classified by the radius measured from the stent cross section corresponding to the centreline point 'cM' — r_1 (50% of r_3), r_2 (75% of r_3), and r_3 respectively indicate a stent at the severe level of IncSE, at the intermediate level, and under the fully expanded condition. A distal (or a proximal) IncSE is classified by the diameter corresponding to the centreline point 'dM' (or 'pM') — d_1 (50% of d_3), d_2 (75% of d_3), and d_3 respectively indicate a stent at the severe level of IncSE, at the intermediate level, and under the fully expanded condition.

6.2.3 Virtual Stent Deployment

The *PED* is a flexible FD stent braided from 48 metal strands [143]. For a stent, the occurrence of post-treatment IncSE can be related to its length, as well as to the specific location of the stent tip when the sheath is withdrawn. In order to generate stent models for all specified scenarios, IncSE was assumed to occur only within its designated segment, whilst complete stent expansion was achieved in all the remaining segments along the stent's length. Hence, stents of different lengths were modelled according to their mode of IncSE; however, the diameter of each stent was strictly fixed at 5 mm in all models as used in the real treatments.

In the simulation of stent deployment, the stent was first assumed to be crimped in alignment with the centreline of the recipient artery, and then to expand to its unloaded condition, driven by the internal restoring forces. In the restoring process, a

contact detection algorithm was employed to stop the stent nodal movements a short distance (20 μm) away from the vascular boundaries [144].

For simulation of the ideal deployment, the constraint is only the vascular boundaries. For simulation of the stent deployment in which IncSE occurred, apart from the boundary constraints, radial expansion of stent nodes was also constrained with reference to the level of IncSE, corresponding to the respective location 'pM', 'cM', or 'dM', *i.e.* stent nodes stopped expanding towards the measurement direction of radius (for 'c') or diameter (for 'p' or 'd'), when the expansion reached the specified level of IncSE during deployment. However, nodal expansion in other directions would not be affected unless it triggered the boundary detection check.

6.2.4 Aneurysmal Haemodynamics

The patient-specific inflow conditions were acquired through phase contrast magnetic resonance imaging (pcMRI), and respectively set the arithmetic means of the volume flowrate over a cardiac cycle as the inflow boundaries for case 'A' and 'B', which were 3.33 and 2.34 mL/s. (See Figure 6-3 for the pcMRI measurement.) At the outlet of each case, a zero relative pressure condition was assigned. To impose a fully developed flow condition, both the inlet and the outlet domain were extended 20 times the diameter of the ICA in respectively an upstream and a downstream direction.

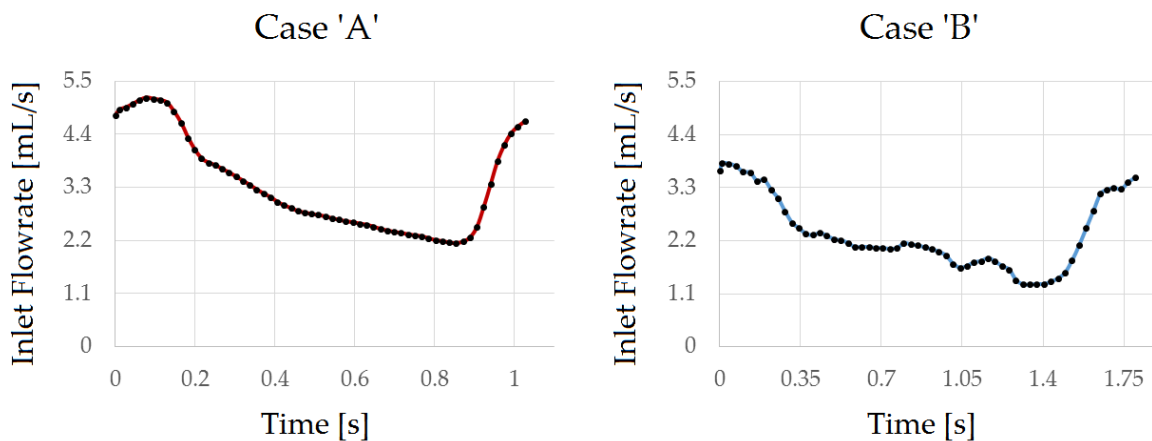


Figure 6-3: Flowrates measured by pcMRI at the inlets of ICA for respectively case 'A' and case 'B'.

The vascular wall and stent wire surface were assumed to be rigid, and a no-slip condition was imposed at these boundaries. With acceptable justification [39], the

assumption of Newtonian, laminar, and incompressible fluid flow was adopted; steady flow simulation was performed with the blood density and viscosity set as 1050 kg/m³ and 0.0035 Pa·s.

The previous work presented a computational grid generation strategy for the simulation of aneurysms with a FD stent implanted [145]. Following the same strategy, a tetrahedral grid was generated with maximum sizes of 0.4, 0.1, and 0.01 mm for respectively volume, aneurysm surface, and stent surface using ICEM-CFD (ANSYS, Canonsburg, USA). I acquired the simulation results by solving the Navier–Stokes equations using the CFX solver for CFD in the ANSYS 18.0 package (ANSYS, USA). The criteria of convergence were chosen as 10^{-5} for the normalised continuity and velocity residuals.

The stent wire configurations, parent-artery flow patterns, iso-velocity surfaces, and wall shear stress (WSS) were examined for each treatment scenario. I quantified the haemodynamic changes by calculating the pressure drop over the parent artery, the intra-aneurysmal mass flowrate (MF), energy loss (EL) [36], average velocity (AV), and velocity curl (VC) for each scenario.

6.3 Results

6.3.1 *In Vivo* and Virtually Deployed FD Stent Configurations

Figure 6-4 (a) depicts the stent wire configurations in treatments with different degrees and locations of IncSE. For both patient cases I observed that stent wires collapsed further with the incrementing of IncSE degree; however, the achievement of adequate wire coverage of the aneurysm orifice was unaffected in all simulated IncSE scenarios (in comparison to the ideally deployment scenarios), *i.e.* no uncovered space can be observed between the stent wires and the aneurysm wall within the aneurysm orifice.

Figure 6-5 shows the stent wire structures observed *in vivo* and in the present simulation. Comparison of these suggests that the severities of IncSE that occurred *in*

vivo are consistent with the simulated scenarios 'c-S' (case 'A') and 'd-S' (case 'B'), both at the more severe level of IncSE.

6.3.2 Aneurysmal Haemodynamics

Figures 6-4 (b) to (d) respectively show: the iso-velocity surfaces (corresponding to 0.125 and 0.065 m/s for cases 'A' and 'B'), the streamlines colour-coded by velocity magnitude, and the wall shear stress distributions for both cases. In all scenarios, I observed no significant additional inflow jets caused by IncSE that enter the aneurysm sac from a position or following an impingement angle different from those in the ideal treatment.

Figure 6-6 presents the normalised values of the intra-aneurysmal MF, EL, AV, and average VC measured from each scenario in comparison to the untreated condition. For both cases, when IncSE occurred in the central or the distal segment, the intra-aneurysmal MF, EL, AV, and VC were respectively elevated by 2.1, 6.0, 3.5, and 5.1 percentage points ('central'), and by 5.4, 10.1, 5.7, and 5.6 percentage points ('distal') compared to the ideal treatments, *i.e.*, a considerable degradation of aneurysmal flow reduction performance. Counter-intuitively, when proximal IncSE occurred, I observed an increase of the aneurysmal flow reduction, with MF, EL, AV, and VC decreasing by 4.4, 3.5, 6.2, and 8.1 percentage points on average, respectively. This effect can clearly be seen in scenarios 'p-S' for both cases.

6.3.3 Pressure Drop and Flow Patterns inside the Parent Artery

Figure 6-7 shows the shear stress distribution on the stent-wire surface, along with a few indicative streamlines, in scenarios where the more severe IncSE occurred in one of the three segments, compared with the ideal treatment for both cases.

For scenarios where IncSE occurred in the 'c' or 'd' segment, blood flow entered the aneurysm sac directly from the lumen formed by stent wires. In this mode, the aneurysmal inflow passed through stent wires once, at the aneurysm orifice. When proximal IncSE occurred, the behaviour was very different. A portion of the

aneurysmal inflow firstly passed through the ‘collapsed’ wires into the stent lumen, and then entered the aneurysm sac across another layer of stent wires at the aneurysm orifice. Under this condition, abnormally high shear stresses were observed on the surface of those collapsed wires that persist in the centre of the parent artery.

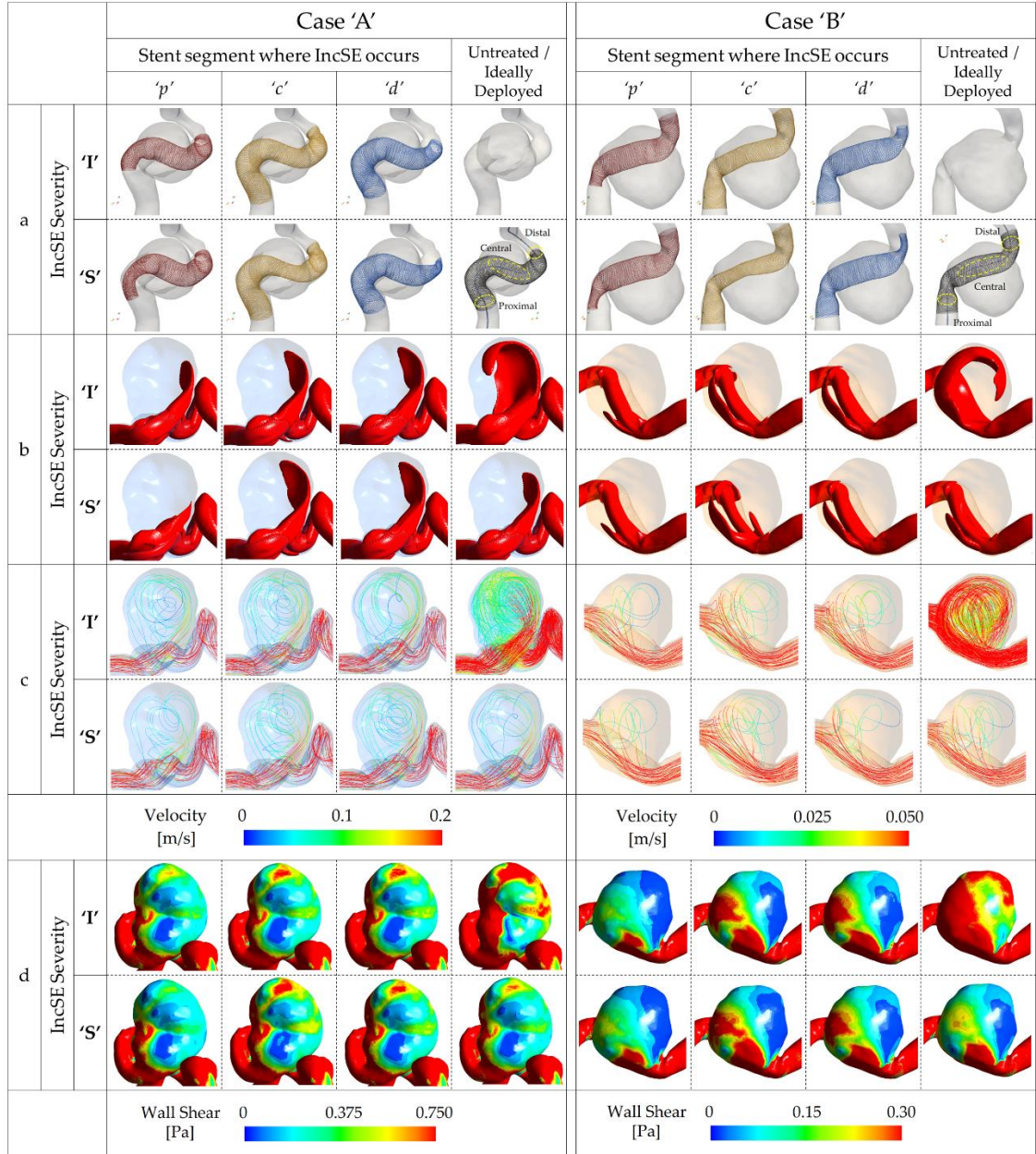


Figure 6-4: FD stent configurations and haemodynamic visualisations of treatments in which IncSE occurs at different levels of severity: (a) FD stent wire configurations; (b) iso-velocity surfaces; (c) streamlines; and (d) wall shear stress distributions. The untreated condition and the treatment with FD stents ideally deployed are also shown for comparison.


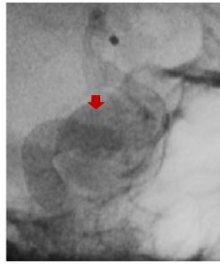
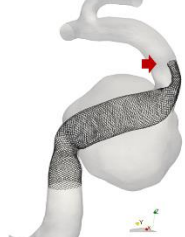


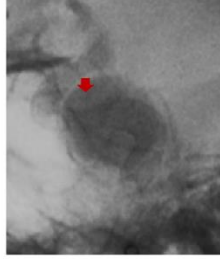

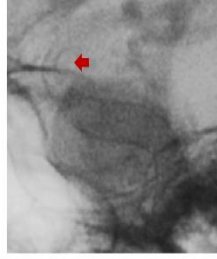
	Case 'A'		Case 'B'	
	Virtual Deployment	<i>In vivo</i> Deployment	Virtual Deployment	<i>In vivo</i> Deployment
Camera View 1				
Camera View 2				
	Scenario 'c-S'		Scenario 'd-S'	

Figure 6-5: Comparison of stent wire configurations between virtual and *in vivo* deployment (DSA imagery) from two different camera views for the two cases. IncSE scenarios 'c-S' and 'd-S' were respectively compared to *in vivo* deployments for case 'A' and 'B'. (Red arrows indicate the segments where stent wire malapposition occur.)

Table 6-1 presents the pressure drop of blood flow through the parent artery. In both cases, the ideal treatment manifests the lowest pressure drop, whereas the distal IncSE scenarios manifest the highest, with the largest differences between them being 45 and 40 Pa respectively for case 'A' and 'B'. In each paired IncSE scenarios, the more severe IncSE exhibits a pressure drop higher than or equivalent to that for the intermediate IncSE.

Table 6-1: Pressure drop (Pa) of blood flow from the inlet to the outlet through the parent artery in different IncSE scenarios for the two cases.

	Ideal Deployment	IncSE Scenario					
		'p-S'	'p-I'	'c-S'	'c-I'	'd-S'	'd-I'
Case 'A'	1003	1020	1011	1030	1010	1048	1049
Case 'B'	288	299	295	318	305	327	321

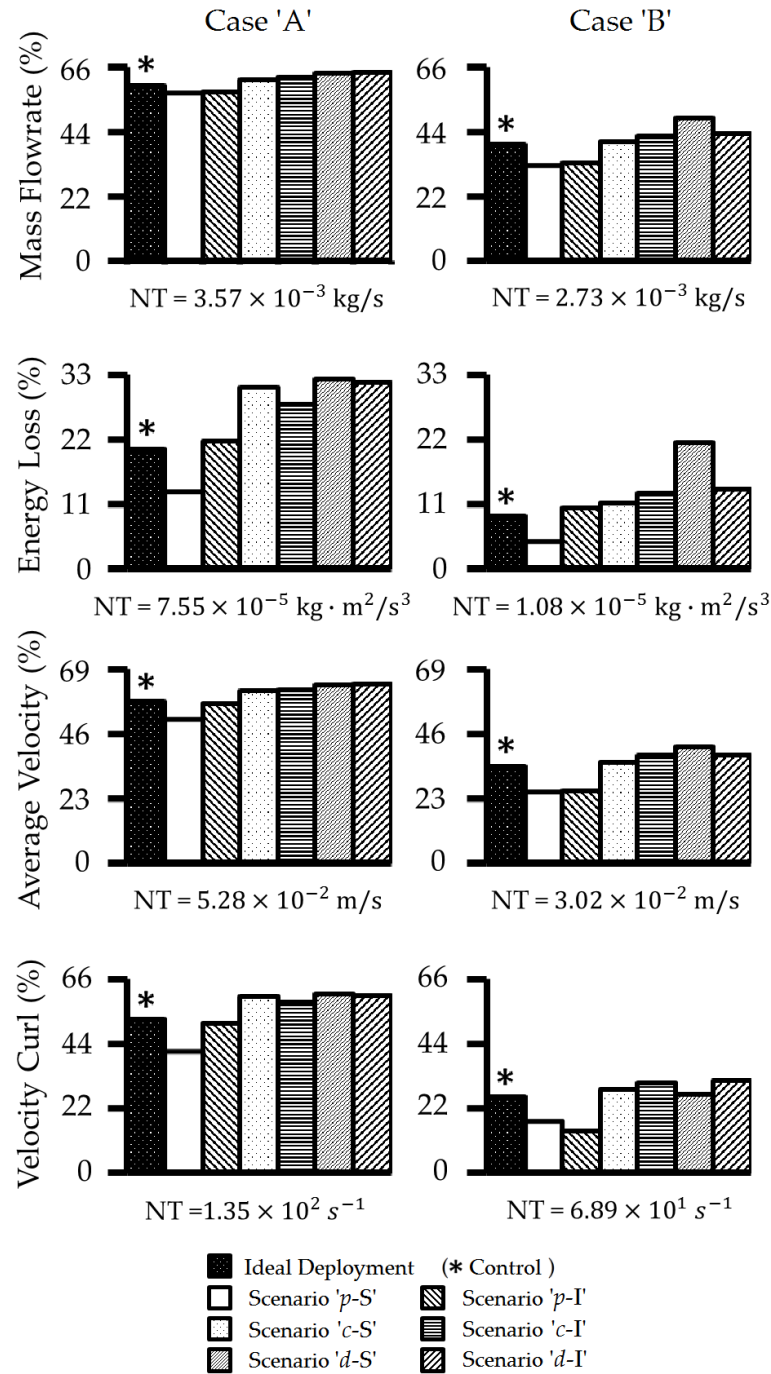


Figure 6-6: Normalised values of the intra-aneurysmal mass flowrate (MF), energy loss (EL), average velocity (AV), and average velocity curl (VC) measured from the ideal deployment scenarios (control group, indicated with '*') and IncSE scenarios 'p-S', 'p-I', 'c-S', 'c-I', 'd-S', and 'd-I' for both aneurysms. The untreated condition (NT) represents the 100% level in each bar chart.

6.4 Discussion

6.4.1 IncSE and Its Association with the Parent Artery's Morphology

The aneurysm treatment cases studied herein were angiographically classified as unfavourable due to the occurrence of IncSE. IncSE is a condition that occasionally occurs after stent intervention, and its effects on aneurysmal haemodynamics might be very negative — as demonstrated herein. Previous studies [146] concluded that the occurrence of IncSE can be associated with the morphological characteristics of the recipient artery. In addition, I found that IncSE in different segments of the parent artery may be caused by different factors.

The occurrence of IncSE at the proximal or the distal end may be attributable to a highly-curved parent artery. This is because the restoring forces acting inside a stent, *i.e.* the force encouraging the stent to regain its unloaded status, may resist the intensive bending imposed by the recipient artery and thus cause the collapse of stent wires. Following this concept, proximal and distal IncSE were modelled at locations with small curvature radius in the present study, and comparison of stent configurations between the IncSEs generated in this study and those occurring *in vivo* demonstrate good agreement.

Unlike the proximal or distal IncSE, the occurrence of central IncSE might be associated with the localised torsion of the parent artery within the aneurysm orifice. This may most likely be due to an enhanced radial constraint produced by the twisted wires, which limits the stent's radial expansion before it reaches its unloaded condition, analogous to the wringing of a towel.

To reduce the likelihood of post-treatment IncSE, two key pieces of advice may be given based upon the present study. Firstly, both the proximal and distal ends of a FD stent are recommended to be located within the parent artery where variation of its curvature is small — a morphological analysis of the parent artery prior to treatment may help to determine an appropriate length of FD stent. Secondly, when a large variation of the erstwhile parent artery's centreline torsion is found immediately

adjacent to the aneurysm orifice, then (where applicable) the deployment of a stent with a larger diameter might neutralise the IncSE effect [86,87,144].

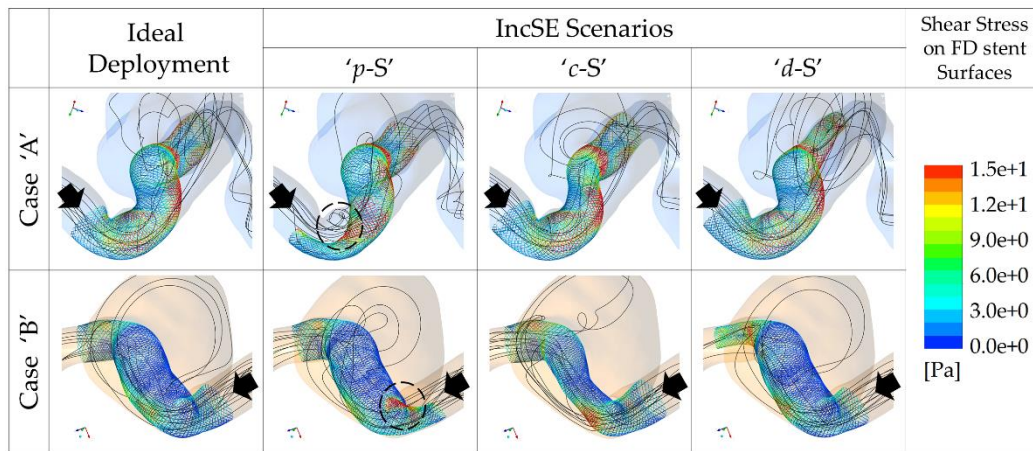


Figure 6-7: Comparisons of the parent-artery flow pattern and shear stress distribution on the stent surface between treatments in which IncSE occurs at three different stent segments. (Black arrows indicate the direction of the parent-artery flow; dashed black circles indicate the regions where collapsed stent wires persist in the centre of the parent artery that disrupt the parent-arterial flow.)

6.4.2 Counter-Intuitive Aneurysmal Flow Reduction Associated with the Proximal IncSE

The IncSE occurring at the proximal end might contribute additionally to the aneurysmal inflow reduction. The mechanism behind this may be the porous-medium effect produced by the collapsed wires that persist in the centre of the parent artery, which disrupted the 'focussed' velocity profile of the parent-arterial flow and caused the velocity to become more uniform throughout the lumen. This contrasts with the 'ideal' deployment, in which the curvature of the proximal section of the parent artery caused blood flow to be focussed in the direction of the stent's periphery, thereby resulting in aneurysmal inflow. This illustrates that the collapsed wires can change the predominant direction of the main parent-arterial stream, a parameter in close relation to the angle of the aneurysmal inflow [147], which can finally affect the aneurysm flow reduction (Figure 6-6).

However, it should be noted that this flow-reduction improvement exists only when the collapse of stent wires does not introduce any additional inflow jet to the aneurysm, and especially that no significant additional component of the parent-artery flow would enter the aneurysm via a bypass route through the uncovered space between the stent and the vascular wall. If the occurrence of IncSE caused significant additional

inflow, then the aneurysmal haemodynamics could be very different, as it has been reported that ‘communicating malapposition¹’ may cause delayed aneurysm occlusion [137].

Therefore, deliberate manipulation to provoke a proximal IncSE should never be recommended, since manipulation of IncSE may lead to a communicating malapposition whereas the additional flow reduction achieved can be very limited (*e.g.* ‘*p-I*’ of case ‘*A*’). More importantly, IncSE’s haemo-rheological and mechano-biological effects are reported to be extremely hazardous: neointimal coverage on stent struts and stent endothelialisation may be disrupted due to the poor vessel wall apposition [138,139,148]; the blood cells then tend to coagulate at those IncSE segments, causing thromboembolic or ischemic events [149,150].

6.4.3 IncSE-Induced Elevated Pressure Drop Increases the Aneurysmal

Inflow

The occurrence of central or distal IncSE can lead to a marked deterioration of the stent’s flow-diversion performance. Observation of aneurysmal haemodynamics revealed that the degraded flow diversion may be related to an elevation of pressure drop over the aneurysm segment, due to the ‘stenosed’ stent wires in the parent artery.

Fundamental theories of fluid mechanics can be used to explain the mechanism behind this phenomenon: that blood flow passing through a gradually (*e.g.* IncSE occurring in the ‘*c*’ segment) or a suddenly (*e.g.* stent malapposition observed in the ‘*d*’ segment) narrowed wire ‘tunnel’ may encounter an increased hydraulic resistance. As a consequence, this resistance may force more blood that remains within the stent lumen to leak into the aneurysm sac, causing a considerable increase of the aneurysmal inflow, as seen with MF values in Figure 6-6. The elevated pressure drop observed in the central and distal IncSE scenarios can be considered evidence of the increased hydraulic resistance.

¹ A communicating malapposition refers to the IncSE that exists proximally to the aneurysm and continues into the aneurysm neck.

Hence, IncSE occurring in the central or distal segment of a FD stent should also be strictly avoided, due to concerns of the possible deterioration of flow-diversion efficacy and post-treatment complications such as in-stent thrombotic occlusion, *etc.*

6.5 Limitations

Several limitations exist in this study. First, the investigation of IncSE did not consider its effect on treatments with FD stents of different diameters, while stent diameter was reported to be a factor that may affect the treatment outcomes [55]. Second, although IncSE was found to have occurred within only one segment of the parent artery of the two patient cases I studied, it should be noted that IncSE can occasionally occur in two sequential segments.

6.6 Conclusion

Based on two patient aneurysms in which IncSE was identified post FD treatment, fourteen treatment scenarios with different severities of IncSE occurring at different segments of the parent arteries were characterised. It has been found that the effects of IncSE on aneurysmal haemodynamics vary greatly with respect to the location where it occurs, from potentially causing a counter-intuitive improvement in aneurysmal flow diversion to causing a deterioration in performance. Morphological analysis of the parent artery, virtual FD treatment, and subsequent CFD simulations prior to the real treatment might help evaluate the risk of IncSE and thus contribute to the planning of an optimal treatment.

Chapter 7

Applying Computational Simulation to the Design of Flow-Diversion Treatment: A Showcase

7.1 Objective

As two feasible strategies for improving flow-diversion efficacy post-treatment, the stent compaction technique and multi-FD stent deployment are frequently applied in the flow-diversion interventions of IAs. Although they have been studied in detail in Chapters 4 and 5, comparisons of haemodynamic changes and flow-diversion improvements resulting from these two strategies have not yet been discussed.

In this Chapter, I seek to contrast the haemodynamic changes resulting from FD treatments with these two strategies applied, based on the simulation results obtained in Chapters 4 and 5.

7.2 Materials and Methods

7.2.1 Treatment scenarios selected for comparison

Six scenarios from virtual treatments of the unsuccessful aneurysm case were selected to contrast their haemodynamic changes caused by different treatment strategies. The unsuccessful case was chosen as the focus because it requires additional flow diversion, whereas the successful case could be treated with just one uncompacted FD.

These 6 scenarios were categorised into three groups:

- 1) conventional single FD stent implantations using stent diameters of 4 or 5 mm, without stent compaction applied (scenarios '*D4npt*' and '*D5npt*');
- 2) single FD stent implantations using stent diameters of 4 or 5 mm, with a high-level compaction (corresponding to a compaction ratio of 80%) applied (scenarios '*D4cp80*' and '*D5cp80*'); and
- 3) dual-FD stent treatments with stent diameters of 4 and 5 mm (scenarios '*D4into5*' and '*D5into4*', meaning a 4 mm stent was deployed into earlier-deployed 5 mm one, neither with compaction applied, and *vice versa*).

In this Chapter, the classification of stent compaction level, as well as the simulation of virtual stent deployment with compaction applied, was the same as that described in Chapter 4 (see Section 4-2 for a detailed description). The same protocol for simulation of multi-FD stent deployment as that reported in Section 5-2 was adopted.

7.2.2 Haemodynamic simulation

The haemodynamic simulation results under the inlet flow condition of 130 mL/min and the outlet pressure of a constant 0 Pa were selected for comparisons in this Chapter. The assumptions of incompressible Newtonian laminar flow, as well as the settings of viscosity and density of blood flow, were the same for the 6 treatment scenarios, as respectively reported in Section 4-3 and Section 5-3.

The values of intra-aneurysmal mass flowrate (MF) and energy loss (EL) were calculated after these 6 treatments. The calculation methods for MF and EL were the same as reported in Section 4-3 and Section 5-3. The MF and EL under the untreated condition are also given for comparison.

7.3 Results

7.3.1 Differences in flow-diversion efficacy

The changes of intra-aneurysmal MF and EL following the 6 treatments were presented in Table 7-1.

As can be seen, both MF and EL were drastically reduced post-treatment, compared to the untreated condition. Treatments with a single FD result in a similar level of flow diversion (for respectively '*D4ncpt*' and '*D5ncpt*', MF: 56.6 % *vs.* 58.6 % and EL: 29.0 % *vs.* 31.7 %, relative to the untreated case). A greater flow diversion was observed in treatments with stent compaction applied: herein '*D4cp80*' and '*D5cp80*' respectively decreased the MF to 17.1 and 30.8 %, and EL to 16.6 and 28.7 %, of the untreated condition. The stent wire configurations markedly differed in dual-FD treatments,

however the flow diversions achieved in ‘*D4into5*’ and ‘*D5into4*’ were similar: MF and EL of 41.5 and 7.8 % versus 42.0 and 9.6 %.

It can be found that the highest flow diversion occurred in the treatment using a FD stent of 5 mm with a compaction of 80%. Comparing treatments with different FD stent diameters, the flow diversion achieved exhibited no obvious distinctions (≤ 3 % in the reductions of intra-aneurysm MF and EL), except for those deployed with compaction technique applied, with differences of 11.7 and 9.4 % in post-treatment MF and EL (‘*D4cp80*’ and ‘*D5cp80*’).

Table 7-1: Haemodynamic parameters calculated before and after the six treatment scenarios.

Treatment scenario	Haemodynamic parameter	
	<i>Mass Flowrate</i> (10^{-3} kg/s)	<i>Energy Loss</i> (10^{-6} kg·m ² /s ³)
NT*	4.103	25.103
<i>D4ncpt</i>	2.321	7.270
<i>D5ncpt</i>	2.405	7.955
<i>D4cp80</i>	1.620	3.115
<i>D5cp80</i>	1.141	0.755
<i>D4into5</i>	1.704	1.947
<i>D5into4</i>	1.722	2.417

* NT: the untreated condition.

7.3.2 Observation of intra-aneurysmal haemodynamics

The FD stent wire structures, the streamlines traversing the aneurysmal sac, and WSS distributions were shown in Figure 7-1. The untreated condition is also shown for comparison. Figure 7-2 demonstrate the different relative MF and EL values post-treatment in the 6 scenarios.

Under the untreated condition, a strong impingement inflow can be identified entering the aneurysm sac through the proximal end. Post-treatment, the strong impingement inflow was reduced in all treatment scenarios, while the treatment using a single 5 mm stent with an 80 % compaction accrued the best inflow reduction. Although the stent structures markedly differ in the dual-FD treatments, the post-treatment aneurysmal flow patterns are very similar (Figure 7-1).

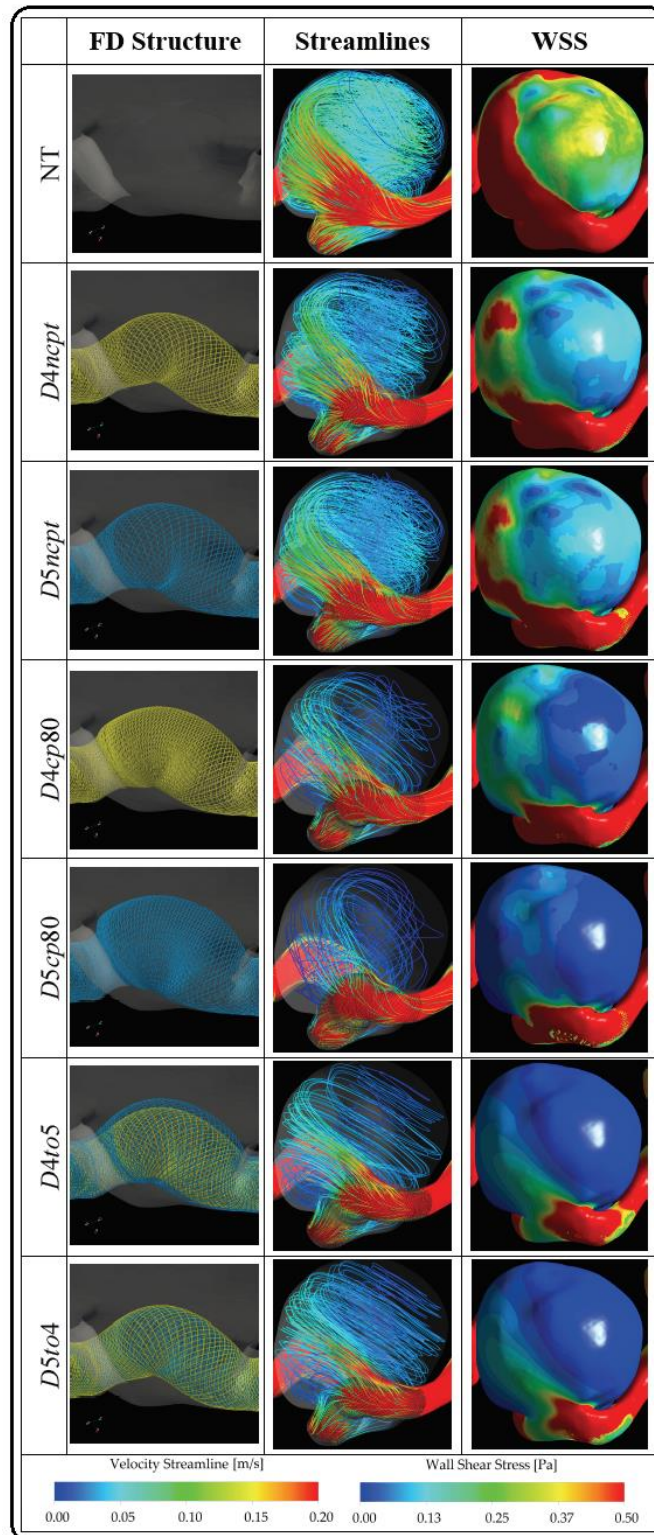


Figure 7-1: FD stent configurations and haemodynamic visualisation of the six treatment scenarios. The untreated case is also given for comparison. (Left column: FD stent configurations; yellow is 4 mm; blue is 5 mm. Middle column: flow streamlines. Right column: WSS distribution. Rows 1 to 7: treatment scenarios ‘NT’, ‘ $D4_{ncpt}$ ’, ‘ $D5_{ncpt}$ ’, ‘ $D4_{cp80}$ ’, ‘ $D5_{cp80}$ ’, ‘ $D4_{to5}$ ’, and ‘ $D5_{to4}$ ’.)

7.4 Discussion

7.4.1 Comparison of haemodynamics in different treatment scenarios

Comparing treatments with stent compaction technique applied with multiple stent implantation, the additional increases of flow diversion efficacy were both around 20 %. In addition, the highest flow diversion was achieved by using a single FD with compaction applied (*'D5cp80'*), rather than by using two FD stents (*'D4into5'* and *'D5into4'*). This suggests that the stent compaction technique might be beneficial to patients, since a decreased metal exposure rate in the parent artery plausibly avoids the risk of post-stenting in-stent stenosis, a serious complication of FD intervention [96,99,151].

Although FD stent implantation with compaction technique applied shows a greater benefit in producing higher flow diversion, it should also be noted that a strong compaction executed during deployment might push the stent wires into the aneurysm sac, causing treatment failure.

Furthermore, evaluation of treatment outcomes can vary with respect to the haemodynamic parameter (or parameters) selected: *e.g.* post-treatment intra-aneurysmal MF in *'D4cp80'* was greater than those in treatments with dual-FD stents, whereas the intra-aneurysmal EL reduction was less than those in the latter two cases. This implies that an overall evaluation of all prospective treatments, and a prioritisation of metrics, may be needed before an optimised treatment plan can be determined.

7.4.2 Effects of stent diameter vary with respect to the treatment strategy

Observing the stent structures in dual-FD stent treatment, I found a wide gap between the 4 mm (inner) and 5 mm (outer) stent layers across the aneurysm ostium. Treatments with a similar mode to this may need further considerations, as a risk of stent migration might be posed when the inner smaller-diameter stent cannot firmly attach to the outer larger-diameter stent in the remaining parent artery segment.

Haemodynamic consequences can also differ with respect to device diameters: an average difference of 10% in flow diversion was observed between treatment scenarios 'D4cp80' and 'D5cp80' (Figure 7-2). This suggests that a treatment rehearsal prior to a real *in vivo* treatment might help clinicians determine a favourable treatment plan.

7.4.3 Clinical relevance of designing a favourable treatment plan

The aneurysm model used was clinically categorised as unsuccessfully treated — a residual aneurysm lobule was identified 6 months after FD intervention. Applying computer simulation to review a set of treatment scenarios may provide some clues of treatment failure from the view point of haemodynamics: *e.g.* the discovered poor flow-diversion efficacy and complex intra-aneurysmal flow patterns in treatments with a single FD stent are in agreement with the clinical treatment outcomes.

If computer simulation can be applied to quantify the haemodynamic consequences of a variety of prospective treatments that may plausibly be used in the real treatment, neuroradiologists may have something more than experience in deciding a favourable treatment plan. For example, scenario 'D5cp80' may be a promising treatment strategy, as it can reduce the EL to just 3 % of the untreated value; as suggested by a previous study, treatments that reduce EL to below 10 % of the untreated value may favour complete aneurysm occlusion.

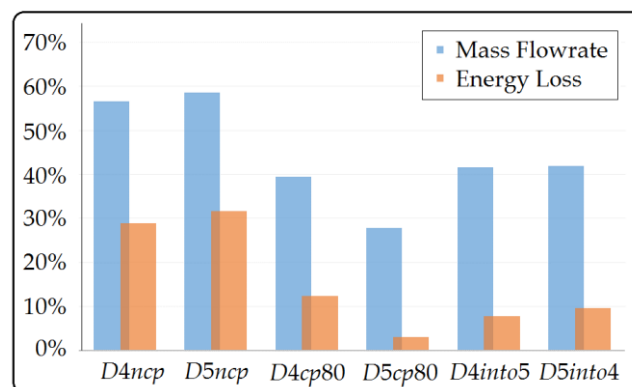


Figure 7-2: Relative mass flow rate and energy loss values for the six treatment scenarios. (The untreated condition, NT, represents the 100% level.)

7.5 Limitations

Limitations have been discussed in sections 4.6 and 5.6. In addition, herein there has been no consideration of combining a compaction technique with dual-FD stent intervention in a given patient aneurysm. It is a future direction to study the combination of stent compaction with multiple FD stent treatment in a series of aneurysm cases.

7.6 Conclusion

In this Chapter, the intra-aneurysmal haemodynamic changes after 6 virtual FD treatments were demonstrated.

Results suggest that:

- 1) both the stent compaction technique and multi-stent implantation effectively reduced the aneurysmal inflow;
- 2) the treatment strategy, as well as the FD device size, may considerably affect the treatment outcome; and
- 3) a treatment rehearsal prior to the real treatment may assist neuroradiologists in determining a favourable treatment plan.

Chapter 8

Conclusion and Outlook

8.1 Conclusion

In interventional practice, deploying a flow-diverting (FD) stent has become an important treatment mode for intracranial aneurysms (IAs). In particular, FD stent implantation is regarded as the only method for those wide-necked or fusiform IAs that previously went untreated. Nonetheless, a number of patients suffer from post-stenting complications, including notably in-stent stenosis and incomplete aneurysm occlusion, suggesting the necessity of intensive investigation of measures that would prevent those complications.

In response to this need, with an intention of individualising the FD stent design and deployment, four main investigations were set up in the present thesis:

- 1) a stent structural optimisation study, which pursues high flow diversion by accommodating FD wire configuration to a given patient aneurysm geometry;
- 2) a haemodynamic investigation of FD treatments with a stent compaction technique applied to devices of various diameters;
- 3) a haemodynamic study of dual-FD stent treatments with various combinations of device diameter under different deployment sequence; and
- 4) research into the effects of incomplete stent expansion on aneurysmal haemodynamics, with various levels of stent malapposition occurring at different segments of the parent artery.

Details of the four studies have been elaborated in Chapters 3, 4, 5, and 6, respectively. To discover the differences between the extra flow diversions generated by the “stent compaction” technique and by implantation of an “additional device”, representative results from Chapters 4 and 5 were selected and compared in Chapter 7.

Results of the present thesis indicate several new findings. Although they have been listed and discussed respectively in each Chapter, it would be remiss not to mention here the following:

- the flow-diversion efficacy of a FD device depends not only on its porosity, but also on its structural design corresponding to a patient aneurysm geometry,

suggesting the possibility of improving the treatment outcome by an individualised stent design (Chapter 3);

- the flow-diversion efficacy could be drastically improved when the “bundle of inflow” of an aneurysm was effectively blocked, or disrupted (Chapter 3);
- the increase of flow diversion with respect to stent compaction ratio follows a linear trend ($R^2 > 0.85$), suggesting that treatment with an appropriate level of stent compaction should be encouraged where applicable (Chapter 4);
- a 25% increase in compaction ratio leads to a further flow-diversion improvement of 10 % on average, whereas the same level of compaction applied to stents of different sizes yields a maximum difference of around 10 % in flow diversion (Chapter 4);
- attributable to the implantation of an additional FD stent, the porosity finally achieved could be decreased further by around 20% and pore density doubled (Chapter 5);
- the effects of the second FD stent’s diameter on haemodynamics are modest, with a standard deviation less than 5 % (Chapter 5); and
- the effects of incomplete stent expansion on aneurysmal haemodynamics are closely associated with the location where it occurs, from potentially causing a slight increase of aneurysmal flow reduction to resulting in a severe degradation of aneurysmal flow diversion (Chapter 6).

Along with these key findings, the present thesis certainly has valuable impacts on future practice of FD stent intervention, as well as on future research and development of FD stents:

Firstly, an automated design optimisation method was developed, which is the first feasible approach that can be readily applied to design optimisation of commercially available stents; this is because the optimal stent configurations obtained using the developed algorithm retain the filament braiding structure of those FD stents on the market.

Secondly, performing virtual stent deployment, I noticed a dangerous morphological characteristic that deserves special attention from the treating clinicians — a highly-curved parent artery with the aneurysm located at the curvature ‘apex’. FD stents deployed along highly-curved arteries can result in a considerable compromise of the metal coverage ratio achieved, compared to those deployed along less-curved ones.

Thirdly, based upon the haemodynamic analyses, I recommend that additional attention should be paid to those cases with ‘gaps’ existing between the parent artery wall and the FD stent wires; the main stream of blood flow in the parent artery may have a chance to enter the aneurysm sac through the ‘gap’, causing treatment failure.

Furthermore, I demonstrated a feasible approach for treatment rehearsals, and found that the flow diversion achieved in the unsuccessfully treated case may be improved to a level similar to that in the successful one, either with a Level-IV compaction applied or with an additional FD stent deployed.

If the treating clinicians could have performed such treatment rehearsals, or had had access to predictive modelling results illustrating the wire configurations of a virtually deployed FD stent and its subsequent haemodynamic outcomes, it is possible that they could have better treated the patient by a more favourable plan determined by haemodynamic simulation.

Finally, the FD stent modelling technique, the classification of stent compaction, and the in-house programs developed for virtual stent deployment *etc.* would certainly contribute to the future studies of FD stent design and treatment planning.

8.2 Outlook

Future work that is recommended to follow on from the present thesis includes mainly the following five points: 1) examining a larger cohort of aneurysms located at different segments of the brain artery, to confirm the trends identified in the thesis of flow-diversion improvement with respect to stent-compaction level and to the number of

stents implanted; 2) enhancing the current virtual stent deployment method, and enabling it to simulate the interaction between the stent and the arterial wall, as well as the interaction between the later- and the earlier-deployed stents while they are being deployed; 3) including more configurations of incomplete stent expansion scenarios with FD stents of different diameters that are malapposed at a series of consecutive parent artery segments, to integrate the investigation of all possible stent malapposition scenarios; 4) applying the current analysis strategy to a larger number of treatments clinically categorised as successful or unsuccessful, to examine the relevance of the predictive haemodynamic parameters used in the current thesis; and 5) establishing a reliable blood-clotting simulation strategy and incorporating it into the current virtual treatment simulation to more directly evaluate the possible treatment outcomes.

Bibliography

- [1] Brisman, J.L., Song, J.K., and Newell, D.W. (2006) Cerebral aneurysms. *New England Journal of Medicine*. 355 (9), 928–939.
- [2] Investigators, T.I.S. of U.I.A. (1998) Unruptured Intracranial Aneurysms — Risk of Rupture and Risks of Surgical Intervention. *New England Journal of Medicine*. 339 (24), 1725–1733.
- [3] Schievink, W.I. (1997) Intracranial Aneurysms. *New England Journal of Medicine*. 336 (1), 28–40.
- [4] Wiebers, D.O. (2003) Unruptured intracranial aneurysms: natural history, clinical outcome, and risks of surgical and endovascular treatment. *The Lancet*. 362 (9378), 103–110.
- [5] Wijdicks, E.F.M., Kallmes, D.F., Manno, E.M., Fulgham, J.R., and Piepgras, D.G. (2005) Subarachnoid Hemorrhage: Neurointensive Care and Aneurysm Repair. *Mayo Clinic Proceedings*. 80 (4), 550–559.
- [6] Anxionnat, R., Bracard, S., Ducrocq, X., Troussel, Y., Launay, L., Kerrien, E., et al. (2001) Intracranial Aneurysms: Clinical Value of 3D Digital Subtraction Angiography in the Therapeutic Decision and Endovascular Treatment. *Radiology*. 218 (3), 799–808.
- [7] King, J.T., Berlin, J.A., and Flamm, E.S. (1994) Morbidity and mortality from elective surgery for asymptomatic, unruptured, intracranial aneurysms: a meta-analysis. *Journal of Neurosurgery*. 81 (6), 837–842.
- [8] Raaymakers, T.W.M., Rinkel, G.J.E., Limburg, M., and Algra, A. (1998) Mortality and Morbidity of Surgery for Unruptured Intracranial Aneurysms. *Stroke*. 29 (8), 1531–1538.
- [9] Sugiyama, S., Endo, H., Niizuma, K., Endo, T., Funamoto, K., Ohta, M., et al. (2016) Computational Hemodynamic Analysis for the Diagnosis of Atherosclerotic Changes in Intracranial Aneurysms: A Proof-of-Concept Study Using 3 Cases Harboring Atherosclerotic and Nonatherosclerotic Aneurysms Simultaneously. *Computational and Mathematical Methods in Medicine*. 2016 1–12.
- [10] Johnston, S.C., Selvin, S., and Gress, D.R. (1998) The burden, trends, and demographics of mortality from subarachnoid hemorrhage. *Neurology*. 50 (5), 1413–1418.
- [11] Juvela, S., Porras, M., and Poussa, K. (2000) Natural history of unruptured intracranial aneurysms: probability of and risk factors for aneurysm rupture. *Journal of Neurosurgery*. 93 (3), 379–387.
- [12] Solomon, R.A., Fink, M.E., and Pile-Spellman, J. (1994) Surgical management of unruptured intracranial aneurysms. *Journal of Neurosurgery*. 80 (3), 440–446.
- [13] Friedman, J.A., Nichols, D.A., Meyer, F.B., Pichelmann, M.A., McIver, J.I., Toussaint, L.G., et al. (2003) Guglielmi detachable coil treatment of ruptured saccular cerebral

- aneurysms: retrospective review of a 10-year single-center experience. *American Journal of Neuroradiology*. 24 (3), 526–533.
- [14] Henkes, H., Fischer, S., Weber, W., Miloslavski, E., Felber, S., Brew, S., et al. (2004) Endovascular coil occlusion of 1811 intracranial aneurysms: early angiographic and clinical results. *Neurosurgery*. 54 (2), 268–285.
 - [15] Higashida, R.T., Smith, W., Gress, D., Urwin, R., Dowd, C.F., Balousek, P.A., et al. (1997) Intravascular stent and endovascular coil placement for a ruptured fusiform aneurysm of the basilar artery: case report and review of the literature. *Journal of Neurosurgery*. 87 (6), 944–949.
 - [16] Murayama, Y., Nien, Y.L., Duckwiler, G., Gobin, Y.P., Jahan, R., Frazee, J., et al. (2003) Guglielmi detachable coil embolization of cerebral aneurysms: 11 years' experience. *Journal of Neurosurgery*. 98 (5), 959–966.
 - [17] Qureshi, A.I., Janardhan, V., Hanel, R.A., and Lanzino, G. (2007) Comparison of endovascular and surgical treatments for intracranial aneurysms: an evidence-based review. *The Lancet Neurology*. 6 (9), 816–825.
 - [18] Alderazi, Y.J., Shastri, D., Kass-Hout, T., Prestigiacomo, C.J., and Gandhi, C.D. (2014) Flow Diverters for Intracranial Aneurysms. *Stroke Research and Treatment*. 2014 1–12.
 - [19] Aydin, K., Arat, A., Sencer, S., Hakyemez, B., Barburoglu, M., Sencer, A., et al. (2014) Treatment of ruptured blood blister-like aneurysms with flow diverter SILK stents. *Journal of NeuroInterventional Surgery*.
 - [20] Bhogal, P., Martinez Moreno, R., Ganslandt, O., Bätzner, H., Henkes, H., and Perez, M.A. (2017) Use of flow diverters in the treatment of unruptured saccular aneurysms of the anterior cerebral artery. *Journal of NeuroInterventional Surgery*. 9 (3), 283–289.
 - [21] Dholakia, R., Sadasivan, C., Fiorella, D., Woo, H., Lieber, B.B., and Lieber, B.B. (2016) Hemodynamics of Flow Diverters. *Journal of Biomechanical Engineering*.
 - [22] D'Urso, P.I., Lanzino, G., Cloft, H.J., and Kallmes, D.F. (2011) Flow Diversion for Intracranial Aneurysms: A Review. *Stroke*. 42 (8), 2363–2368.
 - [23] Karmonik, C., Chintalapani, G., Redel, T., Zhang, Y.J., Diaz, O., Klucznik, R., et al. (2013) Hemodynamics at the ostium of cerebral aneurysms with relation to post-treatment changes by a virtual flow diverter: a computational fluid dynamics study. in: Engineering in Medicine and Biology Society (EMBC), 2013 35th Annual International Conference of the IEEE, IEEE, pp. 1895–1898.
 - [24] Tähtinen, O.I., Manninen, H.I., Vanninen, R.L., Seppänen, J., Niskakangas, T., Rinne, J., et al. (2012) The Silk Flow-Diverting Stent in the Endovascular Treatment of Complex Intracranial Aneurysms: Technical Aspects and Midterm Results in 24 Consecutive Patients. *Neurosurgery*. 70 (3), 617–624.
 - [25] (n.d.) Pipeline Flow Diverter stent—Medtronic. [Http://www.medtronic.com/Covidien/News](http://www.medtronic.com/Covidien/News), Accessed on 2017-07-06.
 - [26] (n.d.) Intracranial Aneurysm—Mayoclinic. [Http://www.mayoclinic.org/medical-professionals/clinical-updates/general-medical/use-of-flow-diverters-to-treat-intracranial-aneurysms-yields-promising-outcomes](http://www.mayoclinic.org/medical-professionals/clinical-updates/general-medical/use-of-flow-diverters-to-treat-intracranial-aneurysms-yields-promising-outcomes), Accessed on 2017-07-06.

- [27] (n.d.) Silk Flow Diverter Stent—Balt Extrusion. <http://www.balt.fr/en>, Accessed on 2017-07-06.
- [28] (n.d.) FRED—Microvention. <http://www.culpanmed.com.au/static/pdf/microvention/fred%20brochure.pdf>, Accessed on 2017-07-06.
- [29] Castro, M.A., Putman, C.M., and Cebal, J.R. (2006) Patient-specific computational fluid dynamics modeling of anterior communicating artery aneurysms: a study of the sensitivity of intra-aneurysmal flow patterns to flow conditions in the carotid arteries. *American Journal of Neuroradiology*. 27 (10), 2061–2068.
- [30] Cebal, J.R., Mut, F., Raschi, M., Hodis, S., Ding, Y.-H., Erickson, B.J., et al. (2014) Analysis of Hemodynamics and Aneurysm Occlusion after Flow-Diverting Treatment in Rabbit Models. *American Journal of Neuroradiology*. 35 (8), 1567–1573.
- [31] Chong, W., Zhang, Y., Qian, Y., Lai, L., Parker, G., and Mitchell, K. (2014) Computational Hemodynamics Analysis of Intracranial Aneurysms Treated with Flow Diverters: Correlation with Clinical Outcomes. *American Journal of Neuroradiology*. 35 (1), 136–142.
- [32] Ku, D.N. (1997) Blood flow in arteries. *Annual Review of Fluid Mechanics*. 29 (1), 399–434.
- [33] Lieber, B.B., Stancampiano, A.P., and Wakhloo, A.K. (1997) Alteration of hemodynamics in aneurysm models by stenting: influence of stent porosity. *Annals of Biomedical Engineering*. 25 (3), 460–469.
- [34] Lieber, B.B. and Sadasivan, C. (2010) Endoluminal Scaffolds for Vascular Reconstruction and Exclusion of Aneurysms From the Cerebral Circulation. *Stroke*. 41 (10, Supplement 1), S21–S25.
- [35] Metaxa, E., Tremmel, M., Natarajan, S.K., Xiang, J., Paluch, R.A., Mandelbaum, M., et al. (2010) Characterization of Critical Hemodynamics Contributing to Aneurysmal Remodeling at the Basilar Terminus in a Rabbit Model. *Stroke*. 41 (8), 1774–1782.
- [36] Qian, Y., Takao, H., Umezu, M., and Murayama, Y. (2011) Risk Analysis of Unruptured Aneurysms Using Computational Fluid Dynamics Technology: Preliminary Results. *American Journal of Neuroradiology*. 32 (10), 1948–1955.
- [37] Sforza, D.M., Putman, C.M., and Cebal, J.R. (2009) Hemodynamics of Cerebral Aneurysms. *Annual Review of Fluid Mechanics*. 41 (1), 91–107.
- [38] Shimogonya, Y., Ishikawa, T., Imai, Y., Matsuki, N., and Yamaguchi, T. (2009) Can temporal fluctuation in spatial wall shear stress gradient initiate a cerebral aneurysm? A proposed novel hemodynamic index, the gradient oscillatory number (GON). *Journal of Biomechanics*. 42 (4), 550–554.
- [39] Steinman, D.A. (2002) Image-Based Computational Fluid Dynamics Modeling in Realistic Arterial Geometries. *Annals of Biomedical Engineering*. 30 (4), 483–497.
- [40] Steinman, D.A., Milner, J.S., Norley, C.J., Lownie, S.P., and Holdsworth, D.W. (2003) Image-based computational simulation of flow dynamics in a giant intracranial aneurysm. *American Journal of Neuroradiology*. 24 (4), 559–566.

- [41] Sugiyama, S.-I., Meng, H., Funamoto, K., Inoue, T., Fujimura, M., Nakayama, T., et al. (2012) Hemodynamic Analysis of Growing Intracranial Aneurysms Arising from a Posterior Inferior Cerebellar Artery. *World Neurosurgery*. 78 (5), 462–468.
- [42] Sforza, D.M., Kono, K., Tateshima, S., Vinuela, F., Putman, C., and Cebal, J.R. (2015) Hemodynamics in growing and stable cerebral aneurysms. *Journal of NeuroInterventional Surgery*.
- [43] Chen, S. and Doolen, G.D. (1998) Lattice Boltzmann method for fluid flows. *Annual Review of Fluid Mechanics*. 30 (1), 329–364.
- [44] Alnaes, M.S., Isaksen, J., Mardal, K.-A., Romner, B., Morgan, M.K., and Ingebrigtsen, T. (2007) Computation of hemodynamics in the circle of Willis. *Stroke*. 38 (9), 2500–2505.
- [45] Bammer, R., Hope, T.A., Aksoy, M., and Alley, M.T. (2007) Time-resolved 3D quantitative flow MRI of the major intracranial vessels: initial experience and comparative evaluation at 1.5 T and 3.0 T in combination with parallel imaging. *Magnetic Resonance in Medicine*. 57 (1), 127–140.
- [46] Wetzel, S., Meckel, S., Frydrychowicz, A., Bonati, L., Radue, E.-W., Scheffler, K., et al. (2007) In vivo assessment and visualization of intracranial arterial hemodynamics with flow-sensitized 4D MR imaging at 3T. *American Journal of Neuroradiology*. 28 (3), 433–438.
- [47] Castro, M.A., Putman, C.M., Sheridan, M.J., and Cebal, J.R. (2008) Hemodynamic Patterns of Anterior Communicating Artery Aneurysms: A Possible Association with Rupture. *American Journal of Neuroradiology*. 30 (2), 297–302.
- [48] Cebal, J.R., Duan, X., Chung, B.J., Putman, C., Aziz, K., and Robertson, A.M. (2015) Wall Mechanical Properties and Hemodynamics of Unruptured Intracranial Aneurysms. *American Journal of Neuroradiology*. 36 (9), 1695–1703.
- [49] Imai, Y., Sato, K., Ishikawa, T., and Yamaguchi, T. (2008) Inflow into Saccular Cerebral Aneurysms at Arterial Bends. *Annals of Biomedical Engineering*. 36 (9), 1489–1495.
- [50] Larrabide, I., Geers, A.J., Morales, H.G., Aguilar, M.L., and Rufenacht, D.A. (2014) Effect of aneurysm and ICA morphology on hemodynamics before and after flow diverter treatment. *Journal of NeuroInterventional Surgery*.
- [51] Rhee, K., Han, M.H., and Cha, S.H. (2002) Changes of Flow Characteristics by Stenting in Aneurysm Models: Influence of Aneurysm Geometry and Stent Porosity. *Annals of Biomedical Engineering*. 30 (7), 894–904.
- [52] Wu, Y.-F., Yang, P.-F., Shen, J., Huang, Q.-H., Zhang, X., Qian, Y., et al. (2012) A comparison of the hemodynamic effects of flow diverters on wide-necked and narrow-necked cerebral aneurysms. *Journal of Clinical Neuroscience*. 19 (11), 1520–1524.
- [53] Zeng, Z., Durka, M.J., Kallmes, D.F., Ding, Y., and Robertson, A.M. (2011) Can aspect ratio be used to categorize intra-aneurysmal hemodynamics?—A study of elastase induced aneurysms in rabbit. *Journal of Biomechanics*. 44 (16), 2809–2816.
- [54] Cebal, J.R., Mut, F., Weir, J., and Putman, C.M. (2011) Association of Hemodynamic Characteristics and Cerebral Aneurysm Rupture. *American Journal of Neuroradiology*. 32 (2), 264–270.

- [55] Hodis, S., Ding, Y.-H., Dai, D., Lingineni, R., Mut, F., Cebal, J., et al. (2014) Relationship between aneurysm occlusion and flow diverting device oversizing in a rabbit model. *Journal of NeuroInterventional Surgery*.
- [56] Chung, B. and Cebal, J.R. (2015) CFD for Evaluation and Treatment Planning of Aneurysms: Review of Proposed Clinical Uses and Their Challenges. *Annals of Biomedical Engineering*. 43 (1), 122–138.
- [57] Kulcsár, Z., Augsburger, L., Reymond, P., Pereira, V.M., Hirsch, S., Mallik, A.S., et al. (2012) Flow diversion treatment: intra-aneurysmal blood flow velocity and WSS reduction are parameters to predict aneurysm thrombosis. *Acta Neurochirurgica*. 154 (10), 1827–1834.
- [58] Moiseyev, G. and Bar-Yoseph, P.Z. (2013) Computational modeling of thrombosis as a tool in the design and optimization of vascular implants. *Journal of Biomechanics*. 46 (2), 248–252.
- [59] Radaelli, A.G., Augsburger, L., Cebal, J.R., Ohta, M., R?fenacht, D.A., Balossino, R., et al. (2008) Reproducibility of haemodynamical simulations in a subject-specific stented aneurysm model? A report on the Virtual Intracranial Stenting Challenge 2007. *Journal of Biomechanics*. 41 (10), 2069–2081.
- [60] Rayz, V.L., Boussel, L., Ge, L., Leach, J.R., Martin, A.J., Lawton, M.T., et al. (2010) Flow Residence Time and Regions of Intraluminal Thrombus Deposition in Intracranial Aneurysms. *Annals of Biomedical Engineering*. 38 (10), 3058–3069.
- [61] Rayz, V.L., Boussel, L., Lawton, M.T., Acevedo-Bolton, G., Ge, L., Young, W.L., et al. (2008) Numerical Modeling of the Flow in Intracranial Aneurysms: Prediction of Regions Prone to Thrombus Formation. *Annals of Biomedical Engineering*. 36 (11), 1793–1804.
- [62] Burns, J.D., Huston, J., Layton, K.F., Piepgras, D.G., and Brown, R.D. (2009) Intracranial Aneurysm Enlargement on Serial Magnetic Resonance Angiography: Frequency and Risk Factors. *Stroke*. 40 (2), 406–411.
- [63] Cebal, J.R., Castro, M.A., Burgess, J.E., Pergolizzi, R.S., Sheridan, M.J., and Putman, C.M. (2005) Characterization of cerebral aneurysms for assessing risk of rupture by using patient-specific computational hemodynamics models. *American Journal of Neuroradiology*. 26 (10), 2550–2559.
- [64] Farnoush, A., Avolio, A., and Qian, Y. (2013) Effect of Bifurcation Angle Configuration and Ratio of Daughter Diameters on Hemodynamics of Bifurcation Aneurysms. *American Journal of Neuroradiology*. 34 (2), 391–396.
- [65] Tremmel, M., Dhar, S., Levy, E.I., Mocco, J., and Meng, H. (2009) Influence of Intracranial Aneurysm-to-Parent Vessel Size Ratio on Hemodynamics and Implication for Rupture: Results from a Virtual Experimental Study. *Neurosurgery*. 64 (4), 622–631.
- [66] Karunanithi, K., Lee, C.-J., Zhang, Y., and Qian, Y. (2012) Risk stratification of cerebrovascular aneurysms using CFD: a review. *RISK*. 10 12.

- [67] Takao, H., Murayama, Y., Otsuka, S., Qian, Y., Mohamed, A., Masuda, S., et al. (2012) Hemodynamic Differences Between Unruptured and Ruptured Intracranial Aneurysms During Observation. *Stroke*. 43 (5), 1436–1439.
- [68] Anzai, H., Ohta, M., Falcone, J.-L., and Chopard, B. (2012) Optimization of flow diverters for cerebral aneurysms. *Journal of Computational Science*. 3 (1–2), 1–7.
- [69] Anzai, H., Chopard, B., and Ohta, M. (2014) Combinational Optimization of Strut Placement for Intracranial Stent Using a Realistic Aneurysm. *Journal of Flow Control, Measurement & Visualization*. 02 (02), 67–77.
- [70] Anzai, H., Falcone, J.-L., Chopard, B., Hayase, T., and Ohta, M. (2014) Optimization of Strut Placement in Flow Diverter Stents for Four Different Aneurysm Configurations. *Journal of Biomechanical Engineering*. 136 (6), 061006.
- [71] Chung, B., Mut, F., Kadirvel, R., Lingineni, R., Kallmes, D.F., and Cebal, J.R. (2014) Hemodynamic analysis of fast and slow aneurysm occlusions by flow diversion in rabbits. *Journal of Neurointerventional Surgery*. 1–5.
- [72] Janiga, G., Daróczy, L., Berg, P., Thévenin, D., Skalej, M., and Beuing, O. (2015) An Automatic CFD-based Flow Diverter Optimization Principle for Patient-specific Intracranial Aneurysms. *Journal of Biomechanics*.
- [73] Srinivas, K., Townsend, S., Lee, C.J., Nakayama, T., Ohta, M., Obayashi, S., et al. (2010) Two-Dimensional Optimization of a Stent for an Aneurysm. *Journal of Medical Devices*. 4 (2), 021003.
- [74] Appanaboyina, S., Mut, F., Löhner, R., Putman, C., and Cebal, J. (2009) Simulation of intracranial aneurysm stenting: Techniques and challenges. *Computer Methods in Applied Mechanics and Engineering*. 198 (45–46), 3567–3582.
- [75] Larrabide, I., Kim, M., Augsburger, L., Villa-Uriol, M.C., Rüfenacht, D., and Frangi, A.F. (2012) Fast virtual deployment of self-expandable stents: Method and in vitro evaluation for intracranial aneurysmal stenting. *Medical Image Analysis*. 16 (3), 721–730.
- [76] Bernardini, A., Larrabide, I., Morales, H.G., Pennati, G., Petrini, L., Cito, S., et al. (2011) Influence of different computational approaches for stent deployment on cerebral aneurysm haemodynamics. *Interface Focus*. 1 (3), 338–348.
- [77] Damiano, R.J., Ma, D., Xiang, J., Siddiqui, A.H., Snyder, K.V., and Meng, H. (2015) Finite element modeling of endovascular coiling and flow diversion enables hemodynamic prediction of complex treatment strategies for intracranial aneurysm. *Journal of Biomechanics*. 48 (12), 3332–3340.
- [78] Ma, D., Xiang, J., Choi, H., Dumont, T.M., Natarajan, S.K., Siddiqui, A.H., et al. (2014) Enhanced Aneurysmal Flow Diversion Using a Dynamic Push-Pull Technique: An Experimental and Modeling Study. *American Journal of Neuroradiology*.
- [79] Ma, D., Dargush, G.F., Natarajan, S.K., Levy, E.I., Siddiqui, A.H., and Meng, H. (2012) Computer modeling of deployment and mechanical expansion of neurovascular flow diverter in patient-specific intracranial aneurysms. *Journal of Biomechanics*. 45 (13), 2256–2263.

- [80] Xiang, J., Ma, D., Snyder, K.V., Levy, E.I., Siddiqui, A.H., and Meng, H. (2014) Increasing Flow Diversion for Cerebral Aneurysm Treatment Using a Single Flow Diverter: *Neurosurgery*. 75 (3), 286–294.
- [81] Janiga, G., Rössl, C., Skalej, M., and Thévenin, D. (2013) Realistic virtual intracranial stenting and computational fluid dynamics for treatment analysis. *Journal of Biomechanics*. 46 (1), 7–12.
- [82] Peach, T., Spranger, K., and Ventikos, Y. (2016) Virtual flow-diverter treatment planning: The effect of device placement on bifurcation aneurysm haemodynamics. *Proceedings of the Institution of Mechanical Engineers, Part H: Journal of Engineering in Medicine*.
- [83] Peach, T.W., Spranger, K., and Ventikos, Y. (2015) Towards Predicting Patient-Specific Flow-Diverter Treatment Outcomes for Bifurcation Aneurysms: From Implantation Rehearsal to Virtual Angiograms. *Annals of Biomedical Engineering*.
- [84] Peach, T.W., Ngoepe, M., Spranger, K., Zajarias-Fainsod, D., and Ventikos, Y. (2014) Personalizing flow-diverter intervention for cerebral aneurysms: from computational hemodynamics to biochemical modeling: Personalizing Flow-Diverter Intervention for Cerebral Aneurysms. *International Journal for Numerical Methods in Biomedical Engineering*. 30 (11), 1387–1407.
- [85] Lee, C.-J., Srinivas, K., and Qian, Y. (2014) Three-dimensional hemodynamic design optimization of stents for cerebral aneurysms. *Proceedings of the Institution of Mechanical Engineers, Part H: Journal of Engineering in Medicine*. 228 (3), 213–224.
- [86] Berg, P., Iosif, C., Ponsonnard, S., Yardin, C., Janiga, G., and Mounayer, C. (2016) Endothelialization of over- and undersized flow-diverter stents at covered vessel side branches: An in vivo and in silico study. *Journal of Biomechanics*. 49 (1), 4–12.
- [87] Mut, F. and Cebal, J.R. (2012) Effects of Flow-Diverting Device Oversizing on Hemodynamics Alteration in Cerebral Aneurysms. *American Journal of Neuroradiology*. 33 (10), 2010–2016.
- [88] Gentric, J.-C., Salazkin, I., Gevry, G., Raymond, J., and Darsaut, T. (2015) Compaction of flow diverters improves occlusion of experimental wide-necked aneurysms. *Journal of NeuroInterventional Surgery*. neurintsurg-2015-012016.
- [89] Cohen, J.E., Gomori, J.M., Moscovici, S., Leker, R.R., and Itshayek, E. (2014) Delayed complications after flow-diverter stenting: Reactive in-stent stenosis and creeping stents. *Journal of Clinical Neuroscience*. 21 (7), 1116–1122.
- [90] Fiorella, D., Albuquerque, F.C., Deshmukh, V.R., and McDougall, C.G. (2004) In-stent stenosis as a delayed complication of neuroform stent-supported coil embolization of an incidental carotid terminus aneurysm. *American Journal of Neuroradiology*. 25 (10), 1764–1767.
- [91] Kornowski, R., Hong, M.K., Tio, F.O., Bramwell, O., Wu, H., and Leon, M.B. (1998) In-stent restenosis: contributions of inflammatory responses and arterial injury to neointimal hyperplasia. *Journal of the American College of Cardiology*. 31 (1), 224–230.

- [92] Mehran, R., Dangas, G., Abizaid, A.S., Mintz, G.S., Lansky, A.J., Satler, L.F., et al. (1999) Angiographic patterns of in-stent restenosis classification and implications for long-term outcome. *Circulation*. 100 (18), 1872–1878.
- [93] Tominaga, R., Harasaki, H., Sutton, C., Emoto, H., Kambic, H., and Hollman, J. (1993) Effects of stent design and serum cholesterol level on the restenosis rate in atherosclerotic rabbits. *American Heart Journal*. 126 (5), 1049–1058.
- [94] Darsaut, T.E., Bing, F., Salazkin, I., Gevry, G., and Raymond, J. (2011) Testing Flow Diverters in Giant Fusiform Aneurysms: A New Experimental Model Can Show Leaks Responsible for Failures. *American Journal of Neuroradiology*. 32 (11), 2175–2179.
- [95] Makoyeva, A., Bing, F., Darsaut, T.E., Salazkin, I., and Raymond, J. (2013) The Varying Porosity of Braided Self-Expanding Stents and Flow Diverters: An Experimental Study. *American Journal of Neuroradiology*. 34 (3), 596–602.
- [96] Puffer, R.C., Kallmes, D.F., Cloft, H.J., and Lanzino, G. (2012) Patency of the ophthalmic artery after flow diversion treatment of paraclinoid aneurysms: clinical article. *Journal of Neurosurgery*. 116 (4), 892–896.
- [97] Sorensen, E.N., Burgreen, G.W., Wagner, W.R., and Antaki, J.F. (1999) Computational simulation of platelet deposition and activation: I. Model development and properties. *Annals of Biomedical Engineering*. 27 (4), 436–448.
- [98] Wanke, I. and Forsting, M. (2008) Stents for intracranial wide-necked aneurysms: more than mechanical protection. *Neuroradiology*. 50 (12), 991–998.
- [99] Kulcsar, Z., Ernemann, U., Wetzel, S.G., Bock, A., Goericke, S., Panagiotopoulos, V., et al. (2010) High-Profile Flow Diverter (Silk) Implantation in the Basilar Artery: Efficacy in the Treatment of Aneurysms and the Role of the Perforators. *Stroke*. 41 (8), 1690–1696.
- [100] Lubicz, B., Van der Elst, O., Collignon, L., Mine, B., and Alghamdi, F. (2015) Silk flow-diverter stent for the treatment of intracranial aneurysms: a series of 58 patients with emphasis on long-term results. *American Journal of Neuroradiology*. 36 (3), 542–546.
- [101] Lubicz, B., Collignon, L., Raphaeli, G., and De Witte, O. (2011) Pipeline Flow-Diverter Stent for Endovascular Treatment of Intracranial Aneurysms: Preliminary Experience in 20 Patients with 27 Aneurysms. *World Neurosurgery*. 76 (1–2), 114–119.
- [102] Lubicz, B., Collignon, L., Raphaeli, G., Pruvo, J.-P., Bruneau, M., De Witte, O., et al. (2010) Flow-Diverter Stent for the Endovascular Treatment of Intracranial Aneurysms: A Prospective Study in 29 Patients With 34 Aneurysms. *Stroke*. 41 (10), 2247–2253.
- [103] Antiga, L. and Steinman, D.A. (2012) VMTK: vascular modeling toolkit. .
- [104] Zhang, Y., Chong, W., and Qian, Y. (2013) Investigation of intracranial aneurysm hemodynamics following flow diverter stent treatment. *Medical Engineering & Physics*. 35 (5), 608–615.
- [105] Nelson, P.K., Lylyk, P., Szikora, I., Wetzel, S.G., Wanke, I., and Fiorella, D. (2010) The Pipeline Embolization Device for the Intracranial Treatment of Aneurysms Trial. *American Journal of Neuroradiology*.

- [106] Spranger, K. and Ventikos, Y. (2014) Which Spring is the Best? Comparison of Methods for Virtual Stenting. *IEEE Transactions on Biomedical Engineering*. 61 (7), 1998–2010.
- [107] Spranger, K., Capelli, C., Bosi, G.M., Schievano, S., and Ventikos, Y. (2015) Comparison and calibration of a real-time virtual stenting algorithm using Finite Element Analysis and Genetic Algorithms. *Computer Methods in Applied Mechanics and Engineering*. 293 462–480.
- [108] Meier, U., López, O., Monserrat, C., Juan, M.C., and Alcañiz, M. (2005) Real-time deformable models for surgery simulation: a survey. *Computer Methods and Programs in Biomedicine*. 77 (3), 183–197.
- [109] Henderson, A., Ahrens, J., and Law, C. (2004) The ParaView Guide. Kitware Clifton Park, NY, .
- [110] Chopard, B., Ouared, R., and Rüfenacht, D.A. (2006) A lattice Boltzmann simulation of clotting in stented aneurysms and comparison with velocity or shear rate reductions. *Mathematics and Computers in Simulation*. 72 (2–6), 108–112.
- [111] Chopard, B., Dupuis, A., Masselot, A., and Luthi, P. (2002) Cellular automata and lattice boltzmann techniques: an approach to model and simulate complex systems. *Advances in Complex Systems*. 05 (02n03), 103–246.
- [112] Chopard, B., Lagrava, D., Malaspinas, O., Ouared, R., Latt, J., Lovblad, K.-O., et al. (2010) A lattice Boltzmann modeling of bloodflow in cerebral aneurysms. in: V: European Conference on Computational Fluid Dynamics, ECCOMAS CFD, p. 12.
- [113] Hirabayashi, M., Ohta, M., Rüfenacht, D., and Chopard, B. (2003) Characterization of flow reduction properties in an aneurysm due to a stent. *Physical Review E*. 68 (2),.
- [114] Lagrava, D., Malaspinas, O., Latt, J., and Chopard, B. (2012) Advances in multi-domain lattice Boltzmann grid refinement. *Journal of Computational Physics*. 231 (14), 4808–4822.
- [115] Ouared, R. and Chopard, B. (2005) Lattice Boltzmann Simulations of Blood Flow: Non-Newtonian Rheology and Clotting Processes. *Journal of Statistical Physics*. 121 (1–2), 209–221.
- [116] Tamagawa, M. and Matsuo, S. (2004) Predictions of Thrombus Formation Using Lattice Boltzmann Method. *JSME International Journal Series C Mechanical Systems, Machine Elements and Manufacturing*. 47 (4), 1027–1034.
- [117] Wang, D. and Bernsdorf, J. (2009) Lattice Boltzmann simulation of steady non-Newtonian blood flow in a 3D generic stenosis case. *Computers & Mathematics with Applications*. 58 (5), 1030–1034.
- [118] Závodszy, G. and Paál, G. (2013) Validation of a lattice Boltzmann method implementation for a 3D transient fluid flow in an intracranial aneurysm geometry. *International Journal of Heat and Fluid Flow*. 44 276–283.
- [119] LeVeque, R.J. (1992) Numerical methods for conservation laws. Springer Science & Business Media, .

- [120] Pletcher, R.H., Tannehill, J.C., and Anderson, D. (2012) Computational fluid mechanics and heat transfer. CRC Press, .
- [121] (n.d.) Palabos—Flowkit. [Http://Www.Palabos.Org/](http://www.Palabos.Org/), Accessed on 2017-07-06.
- [122] Corbett, S.C., Ajdari, A., Coskun, A.U., and N-Hashemi, H. (2010) In Vitro and Computational Thrombosis on Artificial Surfaces With Shear Stress. *Artificial Organs*. 34 (7), 561–569.
- [123] Jou, L.-D., Chintalapani, G., and Mawad, M.E. (2016) Metal coverage ratio of pipeline embolization device for treatment of unruptured aneurysms: Reality check. *Interventional Neuroradiology*. 22 (1), 42–48.
- [124] Ma, D., Dumont, T.M., Kosukegawa, H., Ohta, M., Yang, X., Siddiqui, A.H., et al. (2013) High Fidelity Virtual Stenting (HiFIVS) for Intracranial Aneurysm Flow Diversion: In Vitro and In Silico. *Annals of Biomedical Engineering*. 41 (10), 2143–2156.
- [125] Xiang, J., Damiano, R.J., Lin, N., Snyder, K.V., Siddiqui, A.H., Levy, E.I., et al. (2015) High-fidelity virtual stenting: modeling of flow diverter deployment for hemodynamic characterization of complex intracranial aneurysms. *Journal of Neurosurgery*. 123 (4), 832–840.
- [126] Kojima, M., Irie, K., Fukuda, T., Arai, F., Hirose, Y., and Negoro, M. (2012) The study of flow diversion effects on aneurysm using multiple enterprise stents and two flow diverters. *Asian Journal of Neurosurgery*. 7 (4), 159.
- [127] Meng, H., Wang, Z., Kim, M., Ecker, R.D., and Hopkins, L.N. (2006) Saccular aneurysms on straight and curved vessels are subject to different hemodynamics: implications of intravascular stenting. *American Journal of Neuroradiology*. 27 (9), 1861–1865.
- [128] Zanaty, M., Chalouhi, N., Tjoumakaris, S.I., Rosenwasser, R.H., Gonzalez, L.F., and Jabbour, P. (2014) Flow-Diversion Panacea or Poison? *Frontiers in Neurology*. 5.
- [129] Shapiro, M., Raz, E., Becske, T., and Nelson, P.K. (2014) Variable Porosity of the Pipeline Embolization Device in Straight and Curved Vessels: A Guide for Optimal Deployment Strategy. *American Journal of Neuroradiology*. 35 (4), 727–733.
- [130] Bouillot, P., Brina, O., Ouared, R., Lovblad, K.-O., Farhat, M., and Mendes Pereira, V. (2015) Hemodynamic transition driven by stent porosity in sidewall aneurysms. *Journal of Biomechanics*. 48 (7), 1300–1309.
- [131] Damiano, R.J., Tutino, V.M., Paliwal, N., Ma, D., Davies, J.M., Siddiqui, A.H., et al. (2017) Compacting a Single Flow Diverter versus Overlapping Flow Diverters for Intracranial Aneurysms: A Computational Study. *American Journal of Neuroradiology*.
- [132] Pereira, V.M., Brina, O., Delattre, B.M.A., Ouared, R., Bouillot, P., Erceg, G., et al. (2014) Assessment of intra-aneurysmal flow modification after flow diverter stent placement with four-dimensional flow MRI: a feasibility study. *Journal of NeuroInterventional Surgery*.
- [133] Bear, J. (1988) Dynamics of Fluids in Porous Media. Revised edition Dover Publications, New York.

- [134] Fischer, S., Vajda, Z., Aguilar Perez, M., Schmid, E., Hopf, N., Bätzner, H., et al. (2012) Pipeline embolization device (PED) for neurovascular reconstruction: initial experience in the treatment of 101 intracranial aneurysms and dissections. *Neuroradiology*. 54 (4), 369–382.
- [135] Ou, C., Huang, W., Yuen, M.M.-F., and Qian, Y. (2016) Hemodynamic modeling of leukocyte and erythrocyte transport and interactions in intracranial aneurysms by a multiphase approach. *Journal of Biomechanics*. 49 (14), 3476–3484.
- [136] Ou, C., Huang, W., and Yuen, M.M.-F. (2017) A computational model based on fibrin accumulation for the prediction of stasis thrombosis following flow-diverting treatment in cerebral aneurysms. *Medical & Biological Engineering & Computing*. 55 (1), 89–99.
- [137] King, R.M., Brooks, O.W., Langan, E.T., Caroff, J., Clarençon, F., Tamura, T., et al. (2017) Communicating malapposition of flow diverters assessed with optical coherence tomography correlates with delayed aneurysm occlusion. *Journal of Neurointerventional Surgery*. neurintsurg–2017.
- [138] Rouchaud, A., Ramana, C., Brinjikji, W., Ding, Y.-H., Dai, D., Gunderson, T., et al. (2016) Wall Apposition Is a Key Factor for Aneurysm Occlusion after Flow Diversion: A Histologic Evaluation in 41 Rabbits. *American Journal of Neuroradiology*. 37 (11), 2087–2091.
- [139] Foin, N., Gutierrez-Chico, J.L., Nakatani, S., Torii, R., Bourantas, C.V., Sen, S., et al. (2014) Incomplete Stent Apposition Causes High Shear Flow Disturbances and Delay in Neointimal Coverage as a Function of Strut to Wall Detachment Distance: Implications for the Management of Incomplete Stent Apposition. *Circulation: Cardiovascular Interventions*. 7 (2), 180–189.
- [140] van der Marel, K., Gounis, M.J., Weaver, J.P., de Korte, A.M., King, R.M., Arends, J.M., et al. (2016) Grading of Regional Apposition after Flow-Diverter Treatment (GRAFT): a comparative evaluation of VasoCT and intravascular OCT. *Journal of NeuroInterventional Surgery*. 8 (8), 847–852.
- [141] Chintalapani, G., Chinnadurai, P., Maier, A., Xia, Y., Bauer, S., Shaltoni, H., et al. (2016) The Added Value of Volume-of-Interest C-Arm CT Imaging during Endovascular Treatment of Intracranial Aneurysms. *American Journal of Neuroradiology*. 37 (4), 660–666.
- [142] Guo, N., Maehara, A., Mintz, G.S., He, Y., Xu, K., Wu, X., et al. (2010) Incidence, Mechanisms, Predictors, and Clinical Impact of Acute and Late Stent Malapposition After Primary Intervention in Patients With Acute Myocardial Infarction: An Intravascular Ultrasound Substudy of the Harmonizing Outcomes With Revascularization and Stents in Acute Myocardial Infarction (HORIZONS-AMI) Trial. *Circulation*. 122 (11), 1077–1084.
- [143] Szikora, I., Berentei, Z., Kulcsar, Z., Marosfoi, M., Vajda, Z.S., Lee, W., et al. (2010) Treatment of Intracranial Aneurysms by Functional Reconstruction of the Parent Artery: The Budapest Experience with the Pipeline Embolization Device. *American Journal of Neuroradiology*. 31 (6), 1139–1147.

- [144] Zhang, M., Li, Y., Zhao, X., Verrelli, D.I., Chong, W., Ohta, M., et al. (2017) Haemodynamic effects of stent diameter and compaction ratio on flow-diversion treatment of intracranial aneurysms: A numerical study of a successful and an unsuccessful case. *Journal of Biomechanics*. 58 179–186.
- [145] Zhang, M., Li, Y., Verrelli, D.I., Chong, W., Ohta, M., and Qian, Y. (2017) Applying computer simulation to the design of flow-diversion treatment for intracranial aneurysms. in: 2017 39th Annual International Conference of the IEEE Engineering in Medicine and Biology Society (EMBC), pp. 3385–3388.
- [146] Wu, W., Qi, M., Liu, X.-P., Yang, D.-Z., and Wang, W.-Q. (2007) Delivery and release of nitinol stent in carotid artery and their interactions: A finite element analysis. *Journal of Biomechanics*. 40 (13), 3034–3040.
- [147] Castro, M.A., Putman, C.M., and Cebal, J.R. (2006) Computational fluid dynamics modeling of intracranial aneurysms: effects of parent artery segmentation on intra-aneurysmal hemodynamics. *American Journal of Neuroradiology*. 27 (8), 1703–1709.
- [148] Kadirvel, R., Ding, Y.-H., Dai, D., Rezek, I., Lewis, D.A., and Kallmes, D.F. (2013) Cellular Mechanisms of Aneurysm Occlusion after Treatment with a Flow Diverter. *Radiology*. 130796.
- [149] Klisch, J., Turk, A., Turner, R., Woo, H.H., and Fiorella, D. (2011) Very Late Thrombosis of Flow-Diverting Constructs after the Treatment of Large Fusiform Posterior Circulation Aneurysms. *American Journal of Neuroradiology*. 32 (4), 627–632.
- [150] Saatci, I., Yavuz, K., Ozer, C., Geyik, S., and Cekirge, H.S. (2012) Treatment of Intracranial Aneurysms Using the Pipeline Flow-Diverter Embolization Device: A Single-Center Experience with Long-Term Follow-Up Results. *American Journal of Neuroradiology*. 33 (8), 1436–1446.
- [151] Kulcsar, Z., Houdart, E., Bonafe, A., Parker, G., Millar, J., Goddard, A.J.P., et al. (2010) Intra-Aneurysmal Thrombosis as a Possible Cause of Delayed Aneurysm Rupture after Flow-Diversion Treatment. *American Journal of Neuroradiology*.